Graphene Optoelectronics and Metamaterials

by

You-Chia Chang

A dissertation submitted in partial fulfillment
of the requirements for the degree of
Doctor of Philosophy
(Applied Physics)
in the University of Michigan
2016

Doctoral Committee:

Professor Theodore B. Norris, Chair
Associate Professor Anthony Grbic
Professor Cagliyan Kurdak
Professor Roberto D. Merlin
Associate Professor Zhaohui Zhong

DEDICATION

To my dearest family

ACKNOWLEDGEMENTS

It has been a long journey in several different senses. As a graduate student, it has been a journey of learning about research. As an international student, it has been a journey of living in a different country. As a now-35-year-old adult, it has been a journey about asking how to live life.

In this seven-year-long journey, I have been lucky to be supported by many people. My family is always my strongest and warmest support, even though we are separated by the Pacific Ocean. I truly thank my parents for always supporting my decisions, and want to apologize to them for not being around. My dearest mother and sister are the two in the world who understand me best, and always help me through my ups and downs. My respectful father is always there holding the family together for us. And I miss my grandmother, who passed away early this year, so much that I wish I had spent more time with her. I also want to thank my cousin Eric for editing the language of the dissertation.

Research is never done alone, especially in an experimental group. I would like to thank all the lab members I have worked with in the Norris group: Dong, Chuck, Malakeh, Yunbo, Jessica, Momchil, Pacha, Miao-Bin, Heather, Xiuli, Yang, Qinsheng, Gong, Nooshin, Laura, Zhen, and Moussa. Special thanks go to Dong, who taught me a lot when I first joined the group. I also want to thank Steve for helping with the laser in lab. Since I worked in the Lambda Cubed lab for one of my projects, I want to give my special thanks to Bixue and John, who never hesitate to help with my experiments and share their experience. I also want to thank my collaborators in the Zhong group, Chang-Hua and Che-Hung, for everything we have done together.

One cannot go on a journey without friends. I want to thank my Taiwanese friends in Ann Arbor, roommates, Applied Physics family (especially Cyndi and Chuck), tennis

partners, and judo partners at the Japanese Martial Arts Center. You have all been very important to my journey here.

Last but not least, I would like to give special thanks to my advisor, Prof. Ted Norris, for providing the research opportunities, advice and support during all these years. I want to thank Prof. Zhaohui Zhong for the collaboration on the projects of graphene photodetectors and graphene hyperbolic metamaterials. I would also like to acknowledge Prof. Alex Kildishev and Prof. Evgenii Narimanov at Purdue for the collaboration on hyperbolic metamaterials. I would like to thank Dr. Joshua Caldwell at the Naval Research Laboratory for sharing the measured optical constants of hexagonal boron nitride. I would like to thank my master advisor Prof. Chih-Kung Lee at National Taiwan University, who inspired me to pursue a research career. Finally, I want to thank my committee— Prof. Roberto Merlin, Prof. Cagliyan Kurdak, Prof. Zhaohui Zhong, and Prof. Anthony Grbic — for the comments and supports of my research.

TABLE OF CONTENTS

LIST OF FIGURES

LIST OF APPENDICES

ABSTRACT

Graphene, the one-atom-thick carbon crystal, represents the first of an entire class of two-dimensional materials. Many interesting optical properties arise from the atomic thickness and the electronic band structure with Dirac cones. In this thesis, the opportunities of graphene as a building block for optoelectronics and metamaterials are explored.

Several key frontiers of graphene research specifically for the applications in optoelectronics and metamaterials are addressed. The first frontier, which concerns the understanding of the fundamental optical properties of graphene, is investigated using experimental methods. In one of the projects, experiments are conducted to study the nonlinear harmonic generation of graphene at terahertz frequencies. 10-layer epitaxial graphene is excited with 40 kV/cm terahertz fields but no harmonic generation with an efficiency greater than 2% is observed. This result reveals the fundamental role played by the strong carrier-carrier scattering, which had been neglected by previously published theories of nonlinearity. Another project develops an ellipsometry-based technique that allows for accurate and robust measurement of the optical conductivities of two-dimensional materials. Measurements of the optical conductivities of mono- and bilayer graphene from the ultraviolet to mid-infrared range are demonstrated. This technique is also applied to study the effect of chemical doping on the optical conductivity of graphene.

Another class of projects aims to push the second frontier of graphene research — the new opportunities in physics and applications enabled by the fabrication of complex graphene layered structures. These include the development of a double-layer graphene photodetector, which achieves broadband infrared operation and high responsivity on the order of A/W utilizing the phototransistor gain, and the realization of vertically-stacked

graphene-dielectric multilayers, which turns into a hyperbolic metamaterial for wavelengths longer than 4.5 μm.

The third frontier of graphene research addressed in this thesis investigates the combination of graphene with metasurfaces, as graphene and metasurfaces share the same reduced dimensionality compared to their bulk counterparts. A new type of metasurface based on the guided resonance of a photonic hypercrystal is proposed, which can serve as a two-dimensional resonator for enhancing the light-graphene interaction. Using full-wave electromagnetic simulation, it is demonstrated that the combined system can create optical modulators with high modulation depth and photodetectors with enhanced absorption.

CHAPTER 1

Introduction

Section 1.1 Motivation and thesis organization

Since the first isolation of single-layer graphene in 2004 [1,2], many other crystalline materials, such as transition metal dichalcogenides (TMDs), hexagonal boron nitride (h-BN), and black phosphor, have also been exfoliated or grown into atomically thin layers [3-6]. They are now classified as two-dimensional (2D) materials, which have very distinct properties from their bulk counterparts. The discovery of graphene and other 2D materials led to the Nobel Prize in 2010. Different 2D materials can be combined into the so-called van der Waals crystals, thanks to the strong in-plane covalent bonds and weak interlayer van der Waals force [5]. This opens unprecedented freedom of creating artificial crystals because there is no need for lattice match between layers. Each layer of the 2D material can be considered an atomic Lego brick that we can play arbitrarily. Moreover, we have all kinds of Lego bricks in our toolbox, including semimetals, insulators, semiconductors and superconductors.

Recently, the advance in growing and transferring high-quality graphene and other 2D materials has enabled reliable fabrication of more complicated structures [5-10]. We are now at a stage to explore new device concepts by building complicated structures with various atomic Lego bricks. In this thesis, I am particularly interested in the opportunities of graphene in the fields of optoelectronics and metamaterials. As will be discussed in Section 1.4, graphene has many unique optical properties that make it a promising photonic

building block — it is electrically tunable, it allows photodetection, it has interesting optical nonlinearity, and it is a good plasmonic material.

My thesis covers several different interrelated frontiers in graphene-based optoelectronics and metamaterials. In Chapter 2, I conduct an experimental study of the nonlinear response of graphene at terahertz (THz) frequencies. In Chapter 3, a double-layer graphene photodetector with broad band and high responsivity is developed. In Chapter 4, I develop an ellipsometry-based technique that allows for accurate and robust measurement of the optical properties of graphene. In Chapter 5, I realize experimentally a hyperbolic metamaterial (HMM) with graphene-dielectric multilayers.

Metasurfaces are analogous to 2D materials [11,12]. By designing constituent subwavelength structures, metasurfaces can be homogenized into 2D layers with optical functionalities. In Chapter 6, a metasurface made of an ultra-thin photonic hypercrystal slab is investigated with numerical simulation. I also demonstrate a combination of metasurface and graphene for creating optical modulators and better photodetectors.

Section 1.2 Electronic properties of graphene

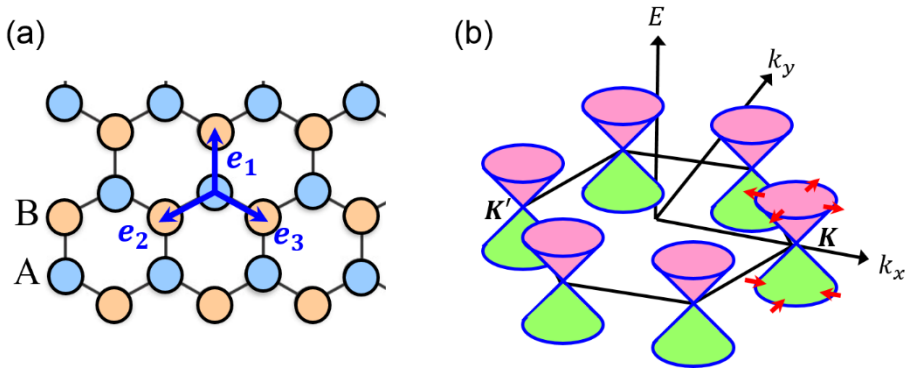

Figure 1.1 **The lattice and the band structure of graphene.** (a) The hexagonal honeycomb lattice of graphene. (b) The Brillouin zone and band structure of graphene. The conduction band and the valence band are represented with pink and green color, respectively. The red arrows represent the direction of pseudospin.

Graphene is an amazing material in many different aspects. It is the thinnest material imaginable and mechanically the strongest material ever measured. It has extremely high intrinsic carrier mobility and thermal conductivity [13]. Among many interesting properties of graphene, optical properties are the main interest of this thesis.

Since the optical response of graphene originates from electronic transitions, I begin this chapter with an introduction to the electronic properties of graphene [14].

Graphene has a hexagonal honeycomb lattice, which can be viewed as two triangular sublattices (labeled by A and B), as plotted in Figure 1.1(a). Strong sp^2 bonds are formed between the nearest carbon atoms, while the fourth valence electron of each carbon atom is in the p_z orbital. It is the p_z electrons that form the interesting band structure of graphene. The band theory of graphene has been known for more than half a century [15,16], which can be derived from the tight-binding model. The tight-binding Hamiltonian of graphene in position representation can be expressed by [14,17-19]

$$\mathrm{H} = -\mathrm{t}\sum_{<i,j>} a_i^+ b_j - \mathrm{t}\sum_{<i,j>} b_i^+ a_j \ , \tag{1}$$

where a_i^+ and b_i^+ are creation operators at position i for A and B sublattices, respectively. $< i,j >$ represents the nearest neighbors. t is the nearest-neighbor hopping energy. We can rewrite Eq. (1) in the momentum representation as

$$\mathrm{H} = \int \frac{d^2\mathbf{k}}{(2\pi)^2} \ (a_{\mathbf{k}}^+ \quad b_{\mathbf{k}}^+)\mathcal{H}(\mathbf{k}) \begin{pmatrix} a_{\mathbf{k}} \\ b_{\mathbf{k}} \end{pmatrix}, \tag{2}$$

where $a_{\mathbf{k}}^+$ and $b_{\mathbf{k}}^+$ are the creation operators for the A and B sublattices in the momentum representation. $\mathcal{H}(\mathbf{k})$ is given by

$$\mathcal{H}(\mathbf{k}) = -t \begin{pmatrix} 0 & e^{-i\mathbf{k}\cdot\boldsymbol{e}_1} + e^{-i\mathbf{k}\cdot\boldsymbol{e}_2} + e^{-i\mathbf{k}\cdot\boldsymbol{e}_3} \\ e^{i\mathbf{k}\cdot\boldsymbol{e}_1} + e^{i\mathbf{k}\cdot\boldsymbol{e}_2} + e^{i\mathbf{k}\cdot\boldsymbol{e}_3} & 0 \end{pmatrix}, \tag{3}$$

where $\boldsymbol{e}_1 = (0, a)$, $\boldsymbol{e}_2 = (-\frac{\sqrt{3}}{2}a, -\frac{a}{2})$ and $\boldsymbol{e}_3 = (\frac{\sqrt{3}}{2}a, -\frac{a}{2})$ are the nearest-neighbor vectors, and a is the lattice constant. We can further expand $\mathcal{H}(\mathbf{k})$ near $\boldsymbol{K}$ and $\boldsymbol{K}'$ points of the Brillouin zone (see Figure 1.1). The low-energy effective Hamiltonian in the vicinity of the $\boldsymbol{K}$ point is given by

$$\mathcal{H}(\mathbf{k}) = \mathcal{H}(\boldsymbol{K} + \mathbf{q}) = \hbar v_{\mathrm{F}} \begin{pmatrix} 0 & \mathrm{q}_x - i\mathrm{q}_y \\ \mathrm{q}_x + i\mathrm{q}_y & 0 \end{pmatrix} = \hbar v_{\mathrm{F}} \boldsymbol{\sigma} \cdot \mathbf{q} \ , \tag{4}$$

where $\boldsymbol{\sigma} = \sigma_x \hat{\boldsymbol{x}} + \sigma_y \hat{\boldsymbol{y}}$ are the Pauli matrices, and $v_{\mathrm{F}} = \frac{3}{2}ta/\hbar$ is the Fermi velocity. In the first quantization language, this Hamiltonian gives the Dirac equation in the momentum representation,

$$\hbar v_{\mathrm{F}} \boldsymbol{\sigma} \cdot \mathbf{q} \, |\psi_{\mathbf{q}}\rangle = E|\psi_{\mathbf{q}}\rangle, \tag{5}$$

from which we can obtain the energy dispersion and the two-component wavefunction:

$$E = \pm \hbar v_{\mathrm{F}} |\mathrm{q}| \, , \tag{6}$$

$$|\psi_{\mathbf{q}}\rangle = \frac{1}{\sqrt{2}} \begin{pmatrix} e^{-i\theta_{\mathbf{q}}/2} \\ \pm e^{i\theta_{\mathbf{q}}/2} \end{pmatrix} |\mathbf{q}\rangle \, . \tag{7}$$

Eq. (6) represents the famous linear energy dispersion of graphene, as plotted in Figure 1.1(b). The + and – signs correspond to the conduction band (electron) and valence band (hole), respectively. $\theta_{\mathbf{q}} = \arctan(\mathrm{q}_y/\mathrm{q}_x)$ is the angle between $\mathbf{q}$ and the x-axis, and the two-component column vector in Eq. (7) is the pseudospinor. We can see from Eq. (7) that the pseudospinor is tied to $\mathbf{q}$. The relation between pseudospinor and $\mathbf{q}$ defines the chirality of the particle, which has important consequences in suppressing the backscattering and contributing to the high mobility of graphene [17,20]. The electron and the hole near the $\boldsymbol{K}$ point are the antiparticles of each other, and have the opposite chiralities [17]. Similarly, the low-energy effective Hamiltonian near $\boldsymbol{K'}$ point is given by

$$\mathcal{H}(\mathbf{k}) = \mathcal{H}(\boldsymbol{K'} - \mathbf{q}) = \hbar v_{\mathrm{F}} \begin{pmatrix} 0 & \mathrm{q}_x + i\mathrm{q}_y \\ \mathrm{q}_x - i\mathrm{q}_y & 0 \end{pmatrix} = \hbar v_{\mathrm{F}} \boldsymbol{\sigma}^* \cdot \mathbf{q} \, . \tag{8}$$

The corresponding Dirac equation in the first quantization language is given by

$$\hbar v_{\mathrm{F}} \boldsymbol{\sigma}^* \cdot \mathbf{q} |\psi'_{\mathbf{q}}\rangle = E|\psi'_{\mathbf{q}}\rangle. \tag{9}$$

The energy dispersion and the two-component wavefunction are given by

$$E = \pm \hbar v_{\mathrm{F}} |\mathrm{q}| \, , \tag{10}$$

$$|\psi'_{\mathbf{q}}\rangle = \frac{1}{\sqrt{2}} \begin{pmatrix} e^{i\theta_{\mathbf{q}}/2} \\ \pm e^{-i\theta_{\mathbf{q}}/2} \end{pmatrix} |\mathbf{q}\rangle. \tag{11}$$

Notice that the particle in each of the two valleys (i.e. near $\boldsymbol{K}$ or $\boldsymbol{K'}$ point) forms a Weyl fermion, and together, they form a Dirac fermion.

Section 1.3 Basic optical properties of graphene

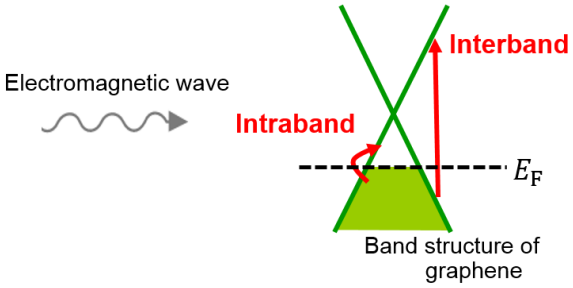

Figure 1.2 **Light-induced interband and intraband transition in doped graphene.**

The optical properties of a truly 2D material are fully described by the optical conductivity $\sigma(\omega)$, which is defined by

$$J = \sigma(\omega)E_{\parallel}, \tag{12}$$

where J is the surface current in graphene and $E_{\parallel}$ is the in-plane component of the electric field. As plotted in Figure 1.2, when electromagnetic fields interact with graphene, they can induce interband and intraband transitions, which are the origin of optical conductivity. Considering the Dirac band structure of graphene, an analytical expression for the optical conductivity can be derived perturbatively from the linear response theory [21-23]:

$$\sigma_{\text{inter}}(\omega) = \frac{\sigma_0}{2}\left(\tanh\frac{\hbar\omega+2E_F}{4k_BT} + \tanh\frac{\hbar\omega-2E_F}{4k_BT}\right) - i\frac{\sigma_0}{2\pi}\log\left[\frac{(\hbar\omega+2E_F)^2}{(\hbar\omega-2E_F)^2+(2k_BT)^2}\right], \tag{13}$$

$$\sigma_{\text{intra}}(\omega) = i\frac{4\sigma_0}{\pi}\frac{E_F}{\hbar\omega+i\hbar\gamma}\ . \tag{14}$$

$\sigma_{\text{inter}}(\omega)$ and $\sigma_{\text{intra}}(\omega)$ represent the conductivity contributed by the interband and intraband transition, respectively. The conductivity $\sigma(\omega)$ equals $\sigma_{\text{inter}} + \sigma_{\text{intra}}$, the sum of the two contributions. σ_0 equals $e^2/(4\hbar)$, a constant often called the universal conductivity of graphene. E_F is the Fermi energy relative to the Dirac point (positive regardless of whether the graphene is p-doped or n-doped), and γ is the intraband scattering rate.

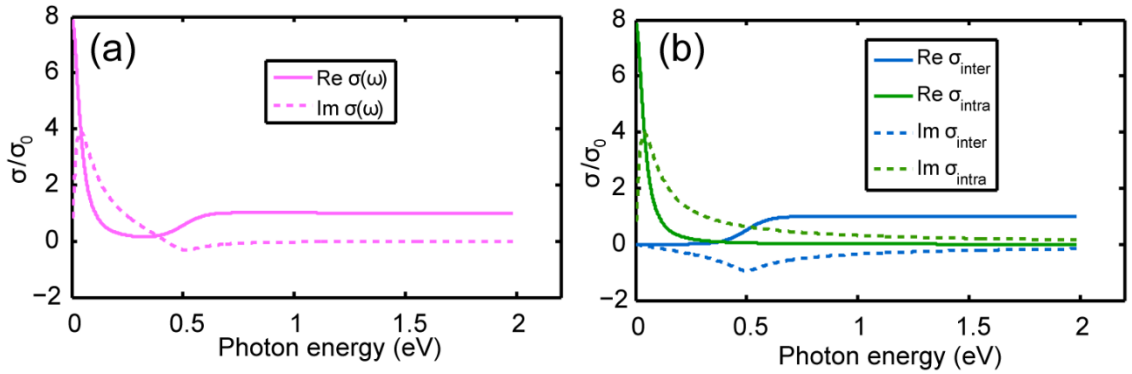

Figure 1.3 **The theoretical optical conductivity of graphene.** (a) The conductivity $\sigma(\omega) = \sigma_{\text{inter}}(\omega) + \sigma_{\text{intra}}(\omega)$ is plotted. (b) The interband and intraband conductivity, $\sigma_{\text{inter}}(\omega)$ and $\sigma_{\text{intra}}(\omega)$, are plotted separately. This figure is plotted with E_{F}=250 meV and $\hbar\gamma$=40 meV.

Many important optical properties of graphene can be understood from Eq. (13-14), which are plotted in Figure 1.3. First, notice that the low-frequency response is dominated by the intraband conductivity $\sigma_{\text{intra}}(\omega)$, while the high-frequency response comes mainly from the interband conductivity $\sigma_{\text{inter}}(\omega)$. $\sigma_{\text{inter}}(\omega)$ exhibits Pauli blocking when $\hbar\omega \lesssim 2E_{\text{F}}$ and approaches the universal conductivity σ_0 at high frequencies. It is this universal conductivity σ_0 that gives the famous 2.3% absorption of suspended graphene in the visible spectral range [24]. The form of Eq. (14) indicates that $\sigma_{\text{intra}}(\omega)$ is described by the Drude model. However, the Drude weight for graphene is proportional to $\sqrt{n}$, the square root of the carrier density, since $\sigma_{\text{intra}}(\omega) \propto E_{\text{F}} \propto \sqrt{n}$. This is different from the Drude model of a bulk metal, in which the Drude weight is proportional to n.

The detailed derivation of Eq. (13-14) can be found in Ref. [21-23]. In Appendix A, I provide the derivation of two special cases that can be derived rather straightforwardly. In the first case, it can be derived from the Fermi's golden rule that $\sigma_{\text{inter}}(\omega)$ equals σ_0 when there is no Pauli blocking [24]. In the second case, the Drudic form of $\sigma_{\text{intra}}(\omega)$ in Eq. (14) is derived semi-classically using the Boltzmann equation [25].

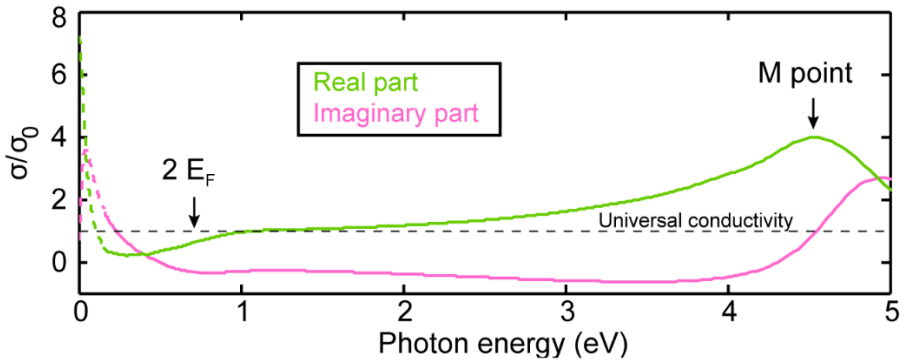

Figure 1.4 **The optical conductivity of graphene measured experimentally with our technique described in Chapter 4.** The solid lines are measured directly, while dash lines are extrapolated from the experimental data using Eq. (14), as they are beyond our detection range.

In fact, the theoretical analytical expression of Eq. (13-14) has limitations, and there are optical properties of graphene that cannot be captured by this theory. Figure 1.4 shows the optical conductivity of graphene measured experimentally with a technique developed by us. This ellipsometry-based technique will be reported in Chapter 4. From the experimental conductivity shown in Figure 1.4, we can see the limitations of the theoretical expressions Eq. (13-14), and obtain a better understanding of some optical properties beyond this theory. First, the theory is developed with the assumption of the Dirac Hamiltonian. Recall that the Dirac Hamiltonian (see Section 1.2.) is the low-energy effective Hamiltonian, which is not accurate for high photon energies. This can be seen from Figure 1.4; the conductivity deviates from σ_0 when the photon energy is larger than ~ 2 eV. In particular, there is a peak at 4.6 eV in the real part of the conductivity. This peak is due to the van Hove singularity at the M point of the Brillouin zone, which is beyond the low-energy linear band structure. Second, Eq. (13-14) are obtained with a non-interacting theory, where electron-hole interaction is absent. However, it has been shown both in experiments and in first-principle calculation that excitonic effects play an important role at high photon energies [26,27]. In fact, the peak associated with the M point is at 5.1 eV according to the non-interacting theory, and it is shifted to 4.6 eV due to the formation of excitons. The excitonic effects alter $\sigma(\omega)$ significantly at high photon energies, and therefore Eq. (13-14) are not capable of describing the optical conductivity of graphene for $\hbar\omega \gtrsim 2$eV. On the other hand, the Drudic intraband conductivity Eq. (14) has been proved

experimentally to be an accurate description for graphene from the mid-infrared to far-infrared ranges [28,29].

Section 1.4 Graphene as a unique photonic building block

Section 1.4.1 Electrically tunable optical conductivity

One of the most unique properties of graphene is its electrically tunable optical conductivity, which has been exploited to realize active photonic devices such as optical modulators and tunable filters [30-32]. The tuning can be performed with a speed as high as tens of GHz, thanks to the high mobility of graphene [30,32]. Such a graphene-based tunable device often incorporates a resonant structure, such as a metallic metasurface [30] or graphene plasmonic structure [33], to further enhance the tunability. In particular, I will report in Chapter 6 a graphene-based optical modulator proposed by us, which incorporates graphene with an ultra-thin resonant photonic hypercrystal.

The tuning is often realized with a gate structure shown in Figure 1.5. The carrier concentration in graphene or other 2D materials can be effectively tuned by electrical gating. As a consequence of the change in carrier concentration, the optical conductivity is also changed. The carrier concentration n is simply given by the formula of a parallel-plate capacitor: $n = (\frac{\varepsilon}{ed})\, V_{\mathrm{g}}$, where ε and d are the DC permittivity and thickness of the gate dielectric, respectively, and V_{g} is the gate voltage. According to this relation, in order to obtain good tunability, it is preferable to use a high ε material as the gate dielectric, or to reduce the thickness d. The latter can be achieved particularly with an ion gel gate dielectric [34].

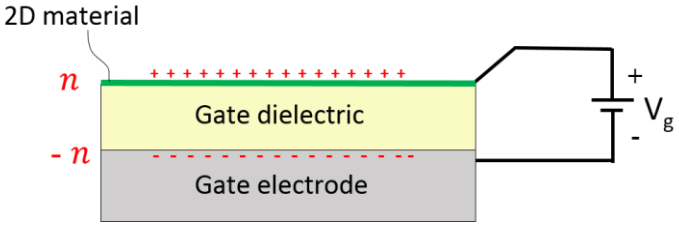

Figure 1.5 **A gate structure to electrically tune the carrier concentration and the optical conductivity of a 2D material.**

An important reason that enables the electrical tunability of the optical properties of graphene is the low density of states. Because of the Dirac band structure, graphene has a very low density of states near the Dirac point. As a result, the change of carrier concentration can shift the Fermi level very effectively [35], and therefore changes the optical conductivity significantly. In Figure 1.6, we plot the optical conductivity of graphene at different Fermi energies using Eq. (13-14). It can be seen that, by varying the Fermi energy, we can shift the wavelength at which the Pauli blocking of the interband transition begins. The Drude weight of the intraband conductivity is also controlled directly by the Fermi energy.

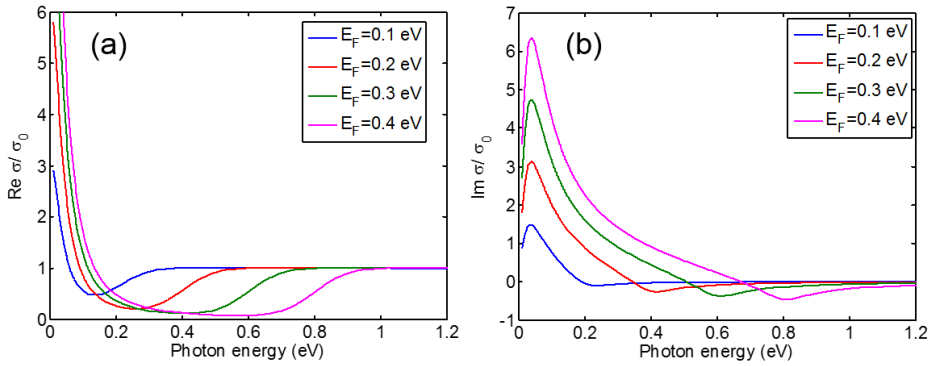

Figure 1.6 **The electrically tunable optical conductivity of graphene.** Real (a) and imaginary (b) part of the optical conductivity of graphene at different Fermi energies, plotted by using the theoretical expression Eq. (13-14). $\hbar\gamma = 40\ meV$ in this plot.

Section 1.4.2 Photodetection

Light absorption in graphene creates photo-excited carriers, which can be detected electrically. Therefore, graphene can be used as a building block for photodetection. The photo-excited carriers in graphene exhibit interesting dynamics: When light is absorbed via interband transition, it creates electrons and holes, and establishes two quasi-Fermi levels in the conduction band and valence band. The two quasi-Fermi levels merge within the first ~ 130 fs [36] due to very fast carrier-carrier scattering. Therefore all the electrons thermalize into a hot electron gas. The hot electrons eventually cool down by the heat transfer to phonons on a time scale of picoseconds, depending on the doping of graphene and the substrate temperature [37,38].

Photodetection with graphene has unique advantages [39,40]. Because graphene has no bandgap, it absorbs light over a very broad spectrum, covering the entire range from ultraviolet to THz [28,41,42], which enables ultra-broadband photodetection. Furthermore, graphene-based detectors can operate with an ultrafast speed (speeds up to 40 GHz have been reported in Ref. 43), thanks to the high mobility and ultrafast carrier dynamics [39,40].

Various mechanisms have been exploited for graphene-based photodetection [39]. First, the photodetection can be accomplished with the photovoltaic effect. The electrons and holes are separated by the built-in electric fields at junctions [43]. Because the photo-excited carriers in graphene have very short life time, the photovoltaic effect happens only near the junction. Second, photodetection can be accomplished with the photo-thermoelectric effect, in which a voltage is created because of the difference in Seebeck coefficients or temperature [44]. This is an important mechanism in graphene particularly because the photo-excited carriers remain a hot electron gas for picoseconds. Third, the bolometric effect can also utilized for photodetection, which relies on the change of electrical conductivity when the carriers in graphene are heated by the incident light [45]. Fourth, the photodetection can be accomplished with the photogating effect [46-48]. This effect is realized with another material (or another graphene layer) that transfers carriers to the graphene channel under light illumination. Therefore, the graphene channel is gated in the presence of light illumination, resulting in a change of carrier concentration in the graphene channel. In Chapter 3, I will report our work on an ultra-broadband and high responsivity graphene photodetector, which is based on this mechanism [48]. Fifth, recently it was found that the lateral photo-Dember effect can take place at the graphene boundaries, which give rise to photocurrents [49].

Section 1.4.3 Nonlinear optics

The optical conductivity discussed in Section 1.3 is appropriate for describing the linear response of graphene. However, when excited by intense light, graphene exhibits nonlinear behaviors, and can be used as a building block for applications in nonlinear optics. For example, graphene has been used as the saturable absorber for mode-locked lasers [50]. A saturable absorber is an optical component that shows higher transmission

(smaller absorption) under stronger optical intensity, which is a key component in passive mode-locking. Under intense illumination, a significant amount of electrons and holes are created in the conduction and valence bands, respectively, resulting in Pauli blocking of further interband transitions, consequently decreasing the absorption. Because the linear energy dispersion, saturable absorption in graphene is broadband, allowing for applications in wide spectral ranges. Another important figure of merit for a saturable absorber is the recovery time. Because of the ultrafast carrier relaxation in graphene, a graphene-based saturable absorber has a short recovery time that is useful for producing ultrafast laser pulses. A mode-locked fiber laser using graphene flakes as the saturable absorber has been demonstrated to produce pulses with a duration of 460 fs [50].

While the second-order nonlinear susceptibility is absent because of symmetry, graphene has a large third-order nonlinear susceptibility $\chi^{(3)}(-\omega; \omega_1, \omega_2, \omega_3)$. This can be attributed to the linear energy dispersion of the band structure, which allows resonance for all the frequencies that participate in the nonlinear parametric process (i.e. $\omega, \omega_1, \omega_2, \omega_3$ are all on resonance) [51,52]. Examples such as four-wave mixing and third harmonic generation have been demonstrated experimentally in graphene [51,53].

In Chapter 2, I will report on our study of the nonlinearity of graphene in the THz spectral range. We have found that the graphene nonlinearity in the THz range can be suppressed by the carrier scattering.

Section 1.4.4 Plasmonic material

Graphene is a semi-metal that supports plasmons. Therefore, graphene can be used as a building block to provide field confinement or enhancement by exploiting its plasmonic behaviours [54, 55]. The relevant spectral range of graphene plasmonics lies in the mid-infrared to THz frequencies. Resonances due to localized plasmons in graphene have been demonstrated in various structures, such as graphene ribbons and discs [34,56,57]. One important feature of the graphene plasmons is the tunability. Because the plasmons depend on the carrier concentration, graphene plasmonics is highly tunable, since the carrier concentration can be controlled by electrical gating or chemical doping (see Section 1.4.1) [34,56]. This is not attainable in metal plasmonics.

The basic plasmonic behaviors of graphene can be described with a semi-classical model [58, 59]. Interestingly, unlike metals that only support TM plasmons, both TM and TE plasmon modes are allowed in graphene. The dispersion relations of TM and TE plasmon modes for suspended graphene are given by [58]

$$1 + i\frac{\sigma(\omega)\sqrt{q^2-(\omega/c)^2}}{2\epsilon_0\omega} = 0, \tag{15}$$

$$1 - i\frac{\omega\mu_0\sigma(\omega)}{2\sqrt{q^2-(\omega/c)^2}} = 0, \tag{16}$$

respectively. Here q is the wave number of the plasmonic mode. It can be seen from Eq. (15) and (16) that the sign of Im σ determines which mode can be supported. TM plasmon mode exists when Im $\sigma > 0$, which is satisfied in most mid-infrared to THz range. On the other hand, TE plasmon mode exists when Im $\sigma < 0$. TE plasmon mode has less practical applications because of the weak confinement; therefore, I will focus on TM plasmon mode in the following discussion.

We can look closer at the dispersion relation of the TM plasmons by inserting the expression of $\sigma(\omega)$ in Eq. (14) into Eq. (15). Consider only the intraband conductivity and neglect the loss, we obtain [55,59]

$$\omega = \sqrt{\left(\frac{2\sigma_0}{\pi\epsilon_0\hbar}\right)E_{\mathrm{F}}q}\ . \tag{17}$$

This expression demonstrates the important signatures of 2D Dirac plasmons: $\omega \propto n^{1/4}$ and $\omega \propto q^{1/2}$ (recall that $E_{\mathrm{F}} = V_{\mathrm{F}}\hbar\sqrt{\pi n} \propto n^{1/2}$ in graphene, where V_{F} is the Fermi velocity) [34,56].

As a closing remark, the results of Eq. (15-17) are based on a semi-classical model, and they only works well when $q \ll k_{\mathrm{F}}$ [59]. A more general dispersion relation of graphene plasmons can be derived from the random phase approximation (RPA) [59,60].

CHAPTER 2

High-field THz response of graphene

Section 2.1 Chapter introduction

Among various applications, graphene is considered a promising electronic material for high speed electronic devices because of the high room-temperature carrier mobility and Fermi velocity (~1/300 of the speed of light). Experimentally, high speed graphene devices such as 100-GHz transistors, 30-GHz modulators and 40-GHz photodetectors have been demonstrated [32,43,61,63,64]. As the operating frequency of graphene devices improves, it becomes crucial to understand how it behaves in the terahertz (THz) regime. In addition, due to many unique THz properties of graphene, such as strong THz absorption of one atomic layer [65] and plasmon resonances of patterned structures [34], graphene can play an important role in the so-called THz gap (0.1 to 10 THz), where there is a need for improved sources, components and detectors.

In a weak field where graphene behaves linearly, the optical properties have been studied extensively over a broad spectral range from visible to THz [24,66-67]. Basic linear optical properties of graphene have been discussed in Section 1.3. In addition, I will report in Chapter 4 an ellipsometry-based technique we develop to measure the linear optical property precisely.

Previous theoretical works on the THz high-field response of graphene have predicted that the Dirac band structure can lead to strong optical nonlinearities [25,68-77]. In particular, efficient harmonic generation at THz frequencies is predicted [25,73-77],

which makes graphene an attractive material for THz frequency multipliers. In addition, since the internal electric field in many graphene devices could reach 100 kV/cm, it is important to determine whether the transport is still linear under such a strong field. We are therefore motivated to conduct an experimental study of the THz nonlinearity of graphene and, in particular, the harmonic generation.

Contrary to these early theoretical predictions, our experiment shows no detectable harmonic generation in the transmitted field, indicating that the early theories have missed some important physics of graphene and have overestimated the nonlinearity. It is noted that the early theoretical works neglect all scattering mechanisms in developing their theories. Our experimental results, which is published in *New Journal of Physics* in 2013 along with another experiment performed by our collaborator at Oregon State University [78], suggest that the nonlinear effects can be suppressed by carrier scattering. Our observation is later supported by more recent theories [76,77].

Section 2.2 Theories of THz harmonic generation in graphene

Theories of THz harmonic generation in graphene have been developed by several different groups before our experimental study [25,74-75]. The earliest work was done by Mikhailov *et al.* in 2007, who analyze the intraband contribution using the semi-classical kinetic theory [25,73]. The basic idea of this theory can be described as follows. The group velocity of electrons can be obtained from the band structure by $v_{\mathrm{gx}} = \partial E/\partial p_{\mathrm{x}}$, where v_{gx} is the group velocity in x direction, E is the energy, and p_{x} is the crystal momentum in x-direction. For parabolic-band materials, as shown by Figure 2.1(a), v_{gx} is linearly proportional to p_{x}. However, this is not the case for graphene due to its Dirac-cone band structure. Considering the conduction-band electrons in graphene, there is a step-function relation between v_{gx} and p_{x}, as indicated by Figure 2.1(b). This step-function relation can gives rise to efficient harmonic generation.

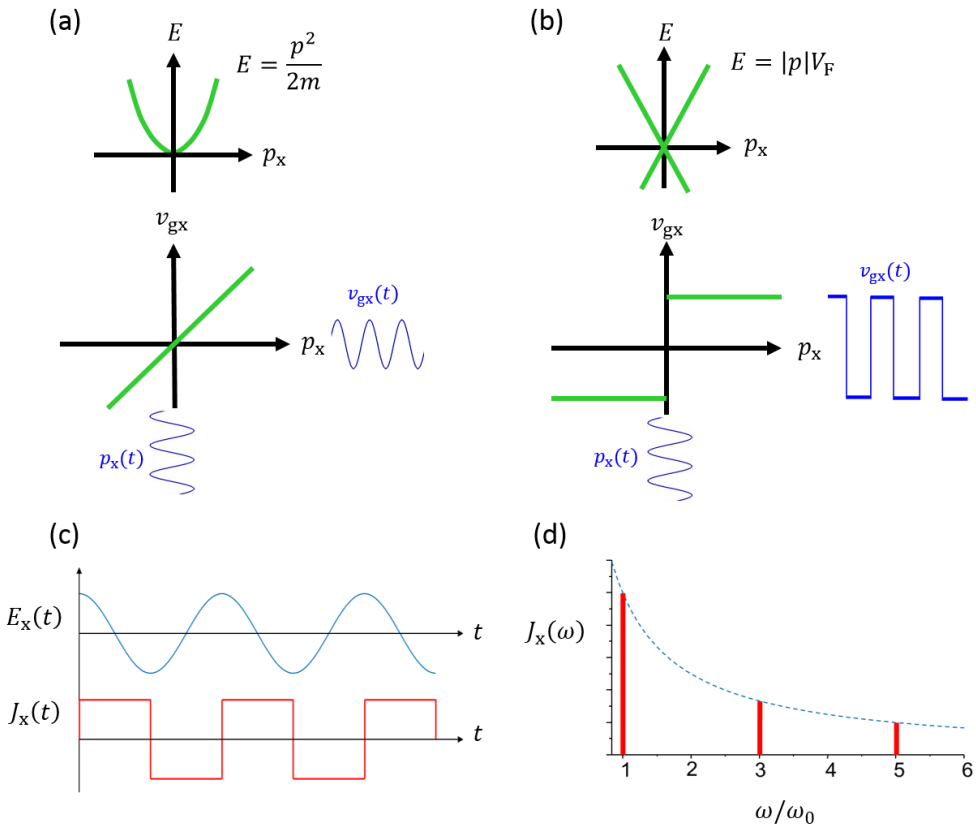

Figure 2.1. **The mechanism for the THz harmonic generation in graphene.** (a) and (b) The band structure and group velocity of a parabolic-band material and graphene. (c) An oscillating electric field and the induced sheet current density in graphene. (d) Fourier spectrum of the sheet current density.

According to the semi-classical equation of motion $dp_x/dt = -eE_x(t)$, an electron gains a momentum $p_x(t) = -(eE_0/\omega_0)\sin(\omega_0 t)$ in an oscillating electric field of $E_x(t) = E_0 \cos(\omega_0 t)$. Because of the step-function relation between v_{gx} and p_x in graphene, the electron moves in the same direction with $p_x(t)$ with a constant speed, i.e., $v_{gx}(t) = -v_F \,\mathrm{sgn}[\sin(\omega_0 t)]$, where v_F is the Fermi velocity of graphene. Accordingly, the sheet current density in graphene is expressed by

$$J_x(t) = env_F \,\mathrm{sgn}[\sin(\omega_0 t)], \tag{1}$$

where n is the carrier density. This means that a sinusoidal excitation can produce a square wave-like sheet current in graphene, and therefore odd harmonics are generated efficiently [25], as shown by Figure 2.1(c-d). Notice that here we consider only the simplest case where p_y of the electron equals 0, which can easily be generalized to cases of $p_y \neq 0$ [25].

The simple calculation described above is extended to an ensemble of electrons using Boltzmann equation in Mikhailov's work [25]. Notice that in their theory only intraband contribution is taken into account. Also, in order for the semi-classical equation of motion to work, the frequency ω needs to satisfy $\hbar\omega \ll max\{E_F, k_B T\}$, where E_F and $k_B T$ are the Fermi energy and thermal energy. Using their theory, Mikhailov *et al.* obtain the critical electric field strength to observe efficient harmonic generation, which is given by 0.3 kV/cm$\times$ $n(10^{11}\text{cm}^{-2})$. For a graphene sample of Fermi energy of 200 meV, the critical field strength is ~ 9 kV/cm.

Since the semi-classical theory developed by Mikhailov *et al.*, there have been other theoretical works that treat this problem quantum-mechanically. In 2009, Wright *et al.* calculate the harmonic generation in undoped graphene by solving the Dirac equation in frequency domain, and predict a strong frequency-tripled current [74]. The critical field strength to observe the harmonic generation in their theory is ~ 2 kV/cm. In 2010, Ishikawa takes a time-domain approach by casting the time-dependent Dirac equation into extended optical Bloch equations, which reveals the importance of the interplay between interband and intraband dynamics [75]. Finite doping is considered in Ishikawa's theory.

It is important to note that, in the theoretical works described above [25,74-75], all scattering mechanisms in graphene are neglected. However, this is not well-justified. In fact, it has been shown that in graphene carrier-carrier scattering is strong and can damp the current [79-82]. Carrier dynamics in graphene is also susceptible to defect scattering and electron-photon scattering [14]. Therefore, in realistic graphene systems, the predicted nonlinear harmonic generation may be obscured by various intrinsic and extrinsic scattering mechanisms, which will be discussed in more detail the Section 2.5.

Section 2.3 Strong THz source based on two-color air ionization

In order to conduct experiments to look for the nonlinear harmonic generation in graphene, a strong ultrafast THz source that produces an electric field of at least 2 kV/cm [25,74-75] is required. However, such a strong field is not achievable with commonly available ultrafast THz sources such as photoconductive emitters and optical rectification

[83]. Therefore, I have built a THz source based on two-color air ionization [84-87], which is able to produce strong single-cycle pulses with a spectrum extending from mid-infrared (MIR) to THz.

Figure 2.2 shows a schematic of the two-color air ionization. A 500 Hz regeneratively amplified Ti-sapphire laser system (Lambda Cubed laser system at University of Michigan) produces 30-fs, 3-mJ pulses [88]. The beam is focused by a lens, and a β-Barium borate (BBO) crystal is placed between the lens and the focal point to generate second harmonics at 400 nm wavelength. The fundamental and second-harmonic pulses add coherently to produce a symmetry-broken field at the focus [84-87], which ionizes the air at the focal point via tunneling ionization process. Because of the broken symmetry, the air plasma at the focal point contains a directional transient current [86,87], which give rise to the broadband MIR and THz radiation.

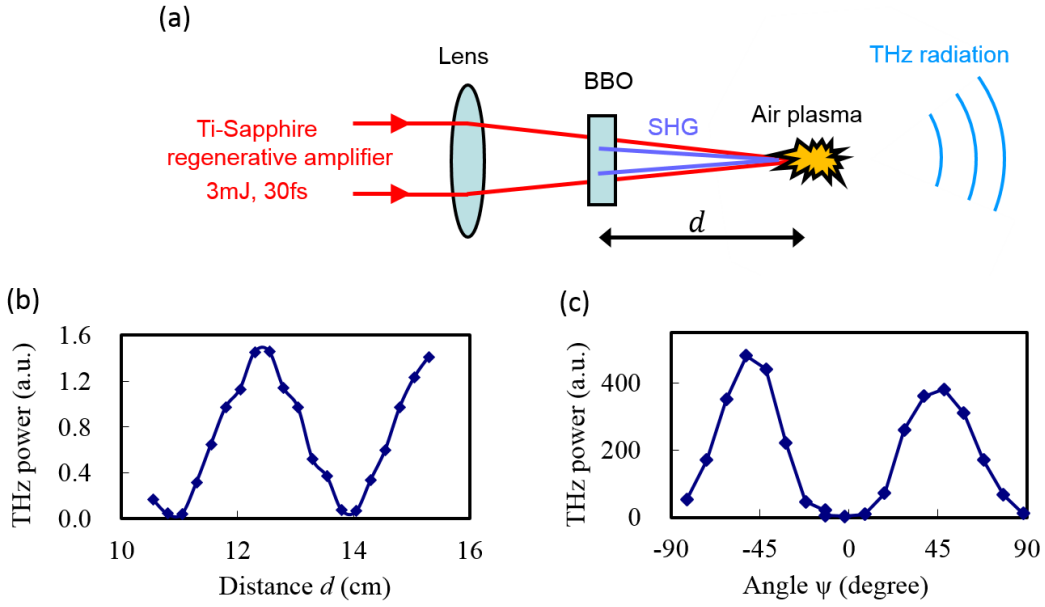

Figure 2.2. **THz source based on two-color air ionization.** (a) The schematic of the optical setup. (b) The phase modulation of the THz generation obtained by changing the distance d. (c) The polarization dependence of the THz generation obtained by rotating the BBO crystal. The THz power is measured with a bolometer.

Since the radiation is created by a coherent process, the phase difference between the fundamental and second-harmonic pulses $\Delta\Phi$ needs optimization, which can be done by adjusting by the distance between the BBO and the focal point [84]. This simple phase

adjustment is possible because the refractive index of air is different for fundamental and second-harmonic pulses. The phase difference is given by

$$\Delta\Phi = k_0(n_\omega - n_{2\omega})d + \Delta\Phi_0, \tag{2}$$

where k_0 is the wave number in vacuum, d is the distance between the BBO crystal and the focal point. n_ω and $n_{2\omega}$ are the refractive index of air for fundamental and harmonic pulses, respectively. $\Delta\Phi_0$ is a constant phase difference that is independent of d. Figure 2.2(b) shows our experimental optimization of $\Delta\Phi$. The THz generation depends critically on $\Delta\Phi$, which is consistent with Ref. 84. The orientation of the BBO crystal also needs optimization. Here we use a type-I BBO crystal, which gives best phase matching for second harmonic generation (SHG) when the angle ψ, defined as the angle between extraordinary axis and the fundamental electric field, equals 90°. However, in this case the electric fields of the fundamental and SHG pulses are perpendicular to each other, and the THz generation becomes inefficient. On the other hand, when ψ equals 0, there is no THz generation because of the lack of SHG. As a result, the optimal angle for ψ we observe is about 45°, which is also consistent with Ref. 84.

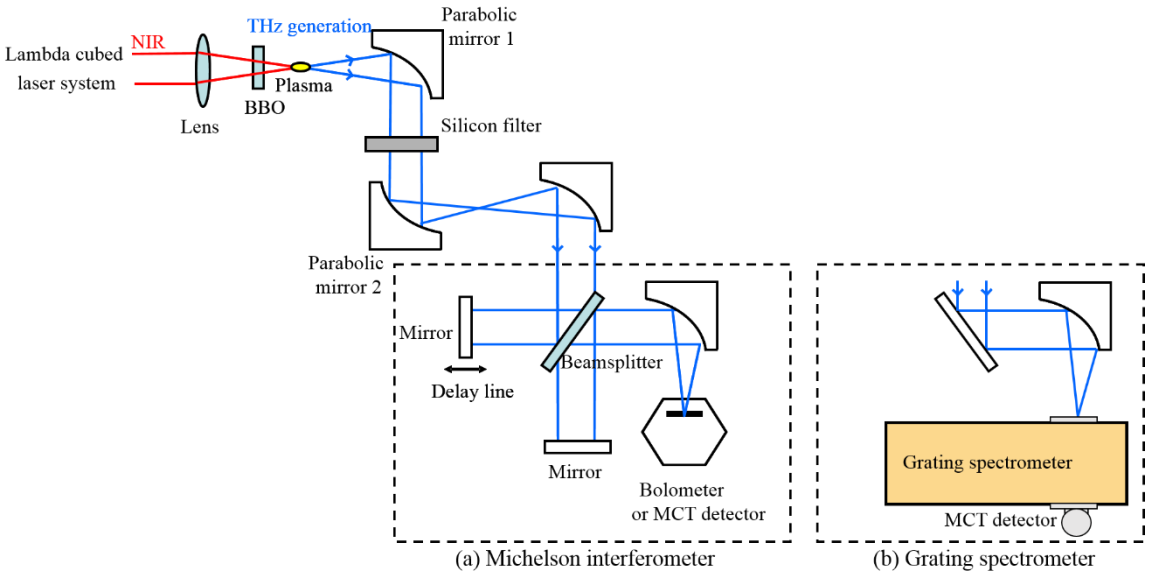

Figure 2.3. **The optical setup of the THz source based on two-color air ionization and the detection system.** (a) The radiation is detected by a Michelson interferometer. (b) The radiation is detected by a grating spectrometer.

The optical setup of the THz source and the detection system are shown in Figure 2.3. The generated THz and MIR radiation from the plasma is collected and re-focused by parabolic mirrors. The unwanted light at near-infrared (NIR) and visible frequencies is blocked by a silicon long-pass filter. To analyze the spectrum of the generated radiation, we use two detection systems, a Michelson interferometer and a grating spectrometer, for different spectral ranges. As shown by Figure 2.3(a), the Michelson interferometer consists of a pellicle beamsplitter and two arms, where one arm is equipped with a delay translation stage. Interferograms are acquired by moving the delay translation stage, and their Fourier transform gives the power spectra. A bolometer (HD-3, IRLabs) and an HgCdTe (MCT) photoconductive detector (MCT-13-1.0, Infrarred Associates) are used for detecting in the THz and MIR ranges, respectively. Figure 2.4(a) shows the interferograms acquired with both detectors, and Figure 2.4(b) shows the corresponding power spectra. However, the Michelson interferometer is not suitable for MIR range because the vibration of the pellicle beamsplitter kills the interference. Instead of the Michelson interferometer, we use a grating spectrometer (Spectra-Pro-500i, Acton) to obtain better MIR spectra, which are shown in Figure 2.3(b) and Figure 2.4(b). These results demonstrate that the two-color air-ionization source creates extremely broadband radiation, ranging from at least 0.15 THz to 80 THz (or equivalently, from wavelengths of 3.75 μm to 2000 μm.)

According to the previous theoretical works of THz harmonic generation in graphene, we need THz electric field of least 2 kV/cm to examine their theoretical predictions [25,74-75]. We can calculate the electric field strength at the focal point of the parabolic mirror 2 in Figure 2.3. The bolometer detects radiations from 0.15 THz to 15 THz. Within this spectral range, we obtained a pulse energy of 6 nJ. The pulse duration is ~0.1 ps, estimated from the interferograms. The spot size at focus is ~300 μm, obtained from a knife-edge measurement. Given these numbers, the calculated electric field strength is 350 kV/cm, which is more than enough to examine the theoretical prediction of the harmonic generation in graphene.

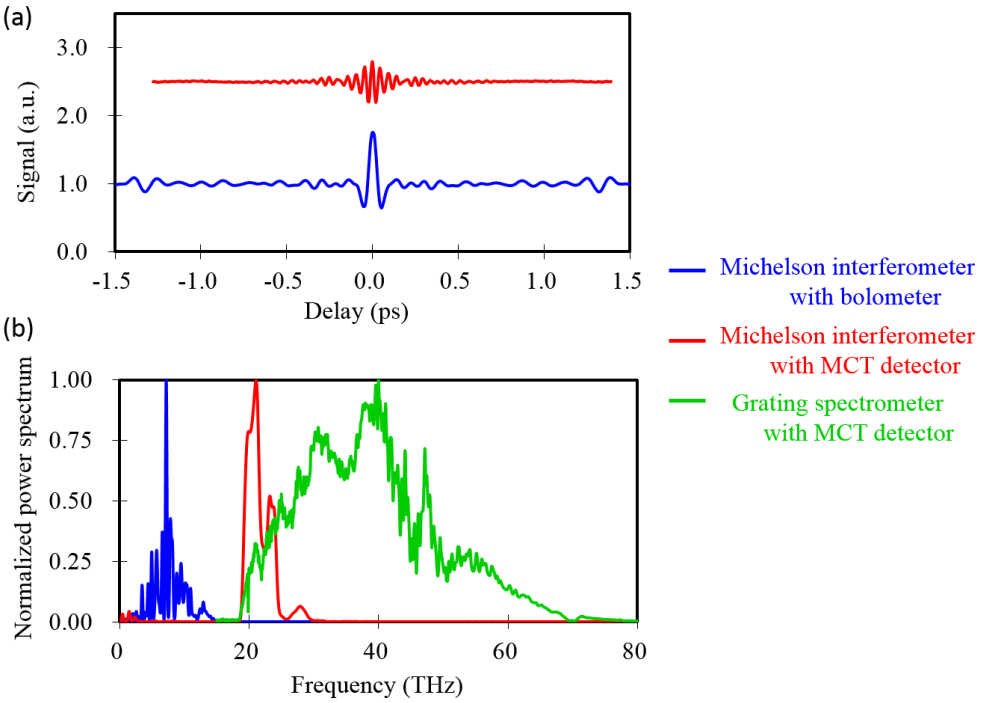

Figure 2.4. **THz radiation from the two-color air ionization source.** (a) Interferomgrams acquired by the Michelson interferometer with a bolometer (blue curve) and a MCT detector (red curve). (b) Power spectra acquired by the Michelson interferometer with a bolometer (blue curve) and a MCT detector (red curve). The green curve is obtained by using a grating spectrometer with a MCT detector. Note that the relative sensitivities between different measurement methods are not calibrated.

The next section will discuss the experiment that searches for the THz harmonic generation in graphene using this optical setup. The strong THz source I built is also used in another work collaborating with Prof. L. Jay Guo group. In that work, we demonstrate experimentally a THz detector based on photoacoustic effect in carbon nanotube nanocomposite. However, that work, published in *Nature Photonics* in 2014 [89], is beyond the scope of this dissertation.

Section 2.4 Experiment of THz harmonic generation in graphene

The goal of this work is to excite graphene with strong THz pules and search for the harmonic generation. Only few experimental works on the strong THz-field response of graphene were reported before our work [65,79], and none of them looked for the THz harmonic generation. On the other hand, Dragoman *et al*. have observed harmonic

generation from graphene in the millimeter wave range, with extremely low generation efficiency [90].

We use an epitaxial graphene sample, which is ideal for this measurement because it has a large area and consists of both highly-doped and nearly-intrinsic layers. Such a wide doping distribution allows us to search for the harmonic generation from both interband and intraband contributions. The sample has approximately 10 graphene layers grown on C-face 4H-SiC substrate. The first few layers close to the SiC substrate are highly n-doped (up to a Fermi level of 360 meV), while other layers are nearly intrinsic [91,92].

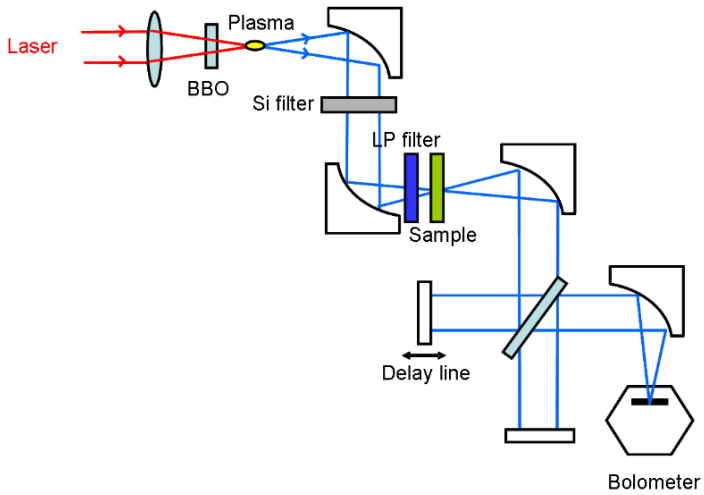

Figure 2.5. **The experimental setup designed to search for the THz nonlinear harmonic generation in graphene.** Strong single-cycle THz pulses, produced by two-color air ionization, are focused to a multilayer epitaxial graphene sample. The spectrum is obtained by a Michelson interferometer and a bolometer.

The optical setup, as shown in Figure 2.5, is similar to Figure 2.3 of Section 2.4, where the details of the optical setup have been described. An epitaxial graphene sample is placed at the focal point of the second parabolic mirror, and a 3-THz low-pass filter (C103, IRLabs) is inserted right before the epitaxial graphene sample to restrict the excitation spectral range to below 3 THz. The electric field strength at the focal point is 40 kV/cm, calculated from the measured pulse energy, duration and spot size. This electric field strength is weaker than the value reported in last section due to the presence of the 3-THz low-lass filter, but still much stronger than the critical field strength (~ 2 kV/cm) predicted by early theoretical works. The interferograms and spectra of the transmitted THz radiation is obtained by using the Michelson interferometer. The THz energy is detected by the bolometer. The experiment is done at the room temperature.

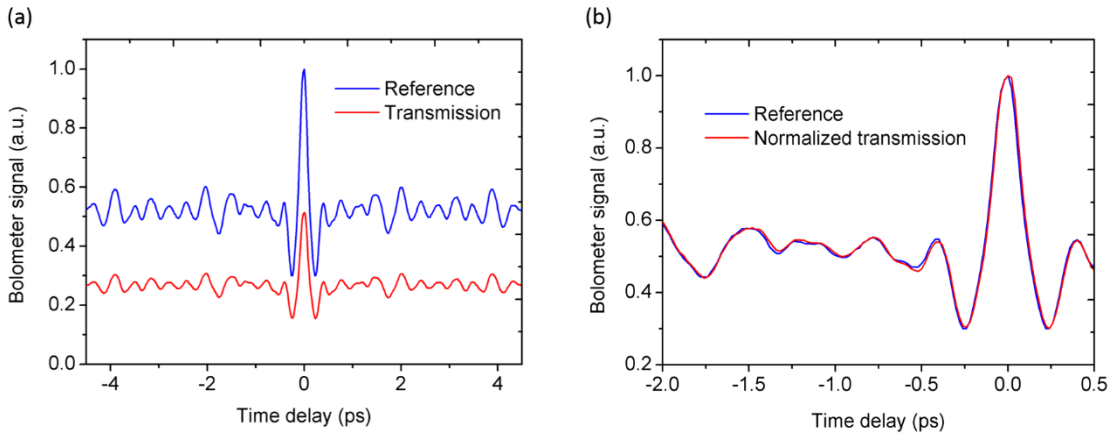

Figure 2.6. **The interferogram of the THz radiation that transmits through multilayer epitaxial graphene.** (a) The interferogram of the THz radiation that transmits through the graphene sample and the reference interferogram acquired with the graphene sample removed. (b) The same interferograms as (a) but with their peaks normalized to the same value.

Figure 2.6(a) shows the interferogram of the transmitted THz radiation, along with the reference interferogram acquired when the epitaxial graphene sample is not present. The transmission through this 10-layer epitaxial graphene sample is ~50%, and the two interferograms are identical within the noise level when they are normalized, as shown in Figure 2.6**(**b), indicating that the graphene sample responds linearly to the incident THz field with a nearly flat spectral response. Figure 2.7(a) shows the transmission and reference spectra, calculated from the Fourier transform of the interferograms in Figure 2.6(a). Most of the power of the incident THz radiation is below 3 THz because of the presence of the 3-THz low-pass filter. However, the transmission spectrum shows no increase of power above 3 THz. In the presence of noise and nonzero transmission through the low-pass filter above 3 THz, the minimal detectable harmonic generation efficiency is ~ 2%. The fact that the transmitted power is smaller than excitation power at all frequencies indicates that no nonlinear harmonic generation larger than ~2% is observed. We also vary the field strength by moving the graphene sample away from the focal point. Figure 2.7(b) shows that the normalized interferograms acquired from different field strengths are nearly identical, indicating again the lack of nonlinear harmonic generation.

As a summary, our experiment observe no detectable (less than 2%) THz nonlinear harmonic generation under strong THz excitation, which contradicts the early theoretical

predictions. This is an indication that the early theories overestimate the nonlinearity and miss some important physics of graphene, which will be discussed in the next section.

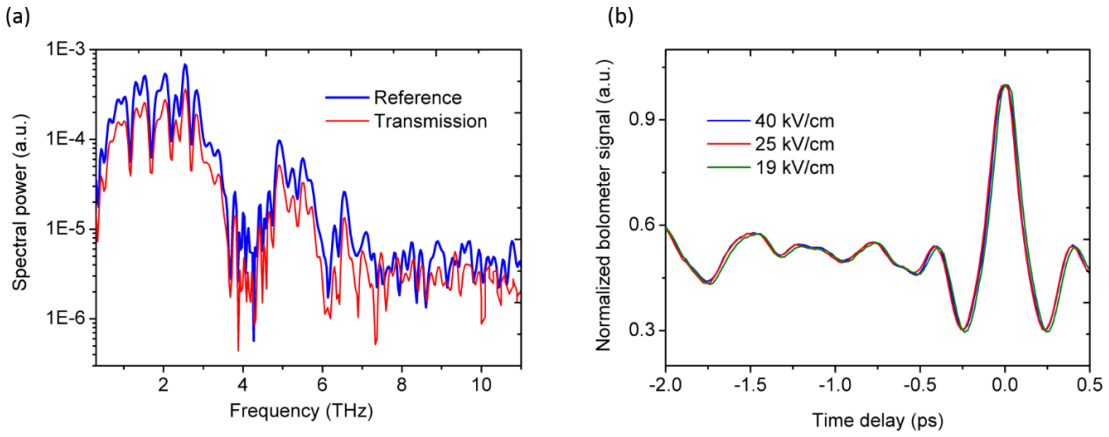

Figure 2.7. **The spectra and interferogram of the THz radiation that transmits through multilayer epitaxial graphene.** (a) Reference and transmission power spectra obtained by the Fourier transform of the interferograms shown in Figure 2.6(a). (b) Normalized interferograms of the THz radiation transmitted through the graphene sample under different incident field strengths.

Section 2.5 Discussions

Our measurements show no observable (< 2 %) THz harmonic generation from 10-layer epitaxial graphene, even though the incident field exceeds significantly the critical field strength predicted by early theories. When we published this experimental result in *New Journal of Physics* in 2013, we proposed that the most likely explanation is the presence of fast carrier-carrier scattering when the electrons of graphene are excited by a strong field [78]. Scattering mechanisms are neglected in the early theoretical studies [25,74-75], where this neglect is only justified by the high mobility of graphene in a low field [25]. However, in a strong field, electrons gain great amount of energy from the field and become hot electrons. Various experiments and calculations have shown that hot electrons in graphene undergo extremely fast carrier-carrier scattering [79-81], which becomes the dominant thermalization mechanism that brings the electrons to equilibrium. Furthermore, unlike in materials with parabolic bands, carrier-carrier scattering in graphene does not conserve current [80,82] and directly leads to damping of current. As the fast thermalization can lead to suppression of nonlinear harmonic current, a theory of nonlinear harmonic generation would have to include the scattering mechanisms.

Our explanation is supported by the following theoretical works after the publication of our experiment in 2013. In 2014, Al-Naib *et al.* published a more sophisticated theory based the density-matrix formalism, which is capable to take scattering into account by introducing a phenomenological scattering time [76,77]. Their calculation shows that carrier scattering can diminish the harmonic generation by destroying the coherence, which agrees with our explanation of the experiment [78]. Another reason for not observing the harmonic generation in our experiment, inferred from their theoretical calculation, is that the surface current created in graphene actually produce very weak radiation. In their theory, the THz transmitted and reflected fields are calculated self-consistently. According to their calculation, the harmonic radiation fields are very small compared to the incident field, even though the harmonic surface current in some case can be comparable to the fundamental surface current in graphene. This means that a monolayer of graphene does not have enough interaction with light to produce strong harmonic radiation.

Al-Naib *et al.* also show in their theoretical work that low cryogenic temperature and low doping are critical for obtaining harmonic generation. They show that strong harmonic current can be generated in undoped graphene under a temperature of 10 K, a scattering time of 50 fs, and a field strength of 0.2 kV/cm. However, even in this case where the surface current induced in graphene is highly nonlinear, the radiation generated by the nonlinear current is still extremely weak. In the transmission direction, the power of the third harmonic radiation is only ~ 3×10^{-7} of the incident power.

There is a more recent experimental work on this topic reported by another group after the publication of our experiment results. Bowlan *et al.* report in *Physical Review B* in 2014 of observing the THz harmonic generation in graphene [93]. They use 45-layer epitaxial graphene and cool the sample to 50 K. Under a field of ~ 40 kV/cm, they observe third harmonic generation with power ~ 3×10^{-3} of the fundamental transmitted power. The significantly higher efficiency than Al-Naib's theoretical prediction may due to the use of multilayer sample and much stronger field.

CHAPTER 3

Ultra-broadband and high responsivity graphene photodetector

Section 3.1 Chapter introduction

Graphene is a promising building block for optoelectronics especially because of the Dirac band structure and high mobility. Because of the lack of bandgap, graphene absorbs light over a very broad spectrum, covering entire range from ultraviolet to THz [41,42,56,66]. This unique property of graphene enables ultra-broadband photodetectors. Graphene photodetectors based on different detection mechanisms (e.g., photovoltaic, photo-thermoelectric, and bolometric effects. See Section 1.4.2) and different operating spectral ranges have been reported by many research groups [39]. However, there are two challenges in graphene-based photodetection. First, the optical absorption of graphene is much weaker than bulk materials due to its atomic thickness. Second, the photo-excited carriers in graphene have ultrashort lifetime before recombination. The ultrashort lifetime has been demonstrated in different experiments, including a study with time-resolved angle-resolved photoemission spectroscopy (ARPES), which shows that the two quasi-Fermi levels in conduction band and valence band merge within ~130 fs [36]. As a result of the weak absorption and the ultrashort carrier lifetime, the responsivities of most graphene photodetectors are limited to only tens of mA/W^{-1} [94-98]. There have been several approaches to increase the responsivity, such as incorporating optical cavities, optical antennas or plasmonic structures to enhance the absorption in graphene [99-101].

However, these approaches sacrifice the ultra-broadband advantage of graphene in exchange of improved responsivity, since the cavities, antennas and plasmonics structures can only operate near resonance.

In this chapter, I will describe a graphene photodetector with high responsivity without sacrificing the ultra-broadband advantage of graphene. It utilizes a gain mechanism to increase the responsivity. The photodetector is composed of two graphene layers sandwiching an ultra-thin tunneling barrier. When light is absorbed by the graphene layers, asymmetric tunneling between the two layers results in the photogating effect, which strongly modifies the conductivity of the channel graphene and provides huge phototransistor gain. Detailed mechanism will be described in Section 3.2. Similar gain mechanisms have also been used in quantum dot-graphene and MoS_2-graphene hybrid systems [46-47]. In those systems, quantum dots or MoS_2 is used as a strong light-absorbing material. When light is absorbed by this material, it transfers charges to graphene channel and produces the photogating effect. However, quantum dots and MoS_2 can only absorb in a narrow spectral range, which again sacrifices the ultra-broadband advantage of graphene.

This work was done in collaboration with Prof. Zhaohui Zhong's group. The device design and fabrication were performed by Chang-Hua Liu in Zhong group. I performed the optical characterization of the devices. The results of this work are published in *Nature Nanotechnol*ogy in 2014 [48] and are the basis of a submitted patent.

Section 3.2 Device structure and operating principle

The device structure of our photodetector is shown in Figure 3.1(a), which is based on a double-layer graphene heterostructure. It has a field effect transistor (FET) architecture, where a p-doped silicon wafer with 285 nm thermal oxide forms the back gate of the device, allowing electrical gating of the bottom layer graphene. Two graphene layers sandwiches a thin tunnel barrier, where the bottom graphene works as the channel and the top graphene works as a floating top gate. A voltage bias is applied between the source and drain, and the drain-source current is detected by the external circuit. The graphene used in our device is grown by chemical vapor deposition (CVD) on copper foil and then

transferred using Poly(methyl methacrylate) (PMMA) method. A 6-nm-thick intrinsic silicon layer is chosen as the tunnel barrier. In another device design that operates in the visible range, we choose a 5-nm-thick Ta_2O_5 layer as the tunnel barrier instead.

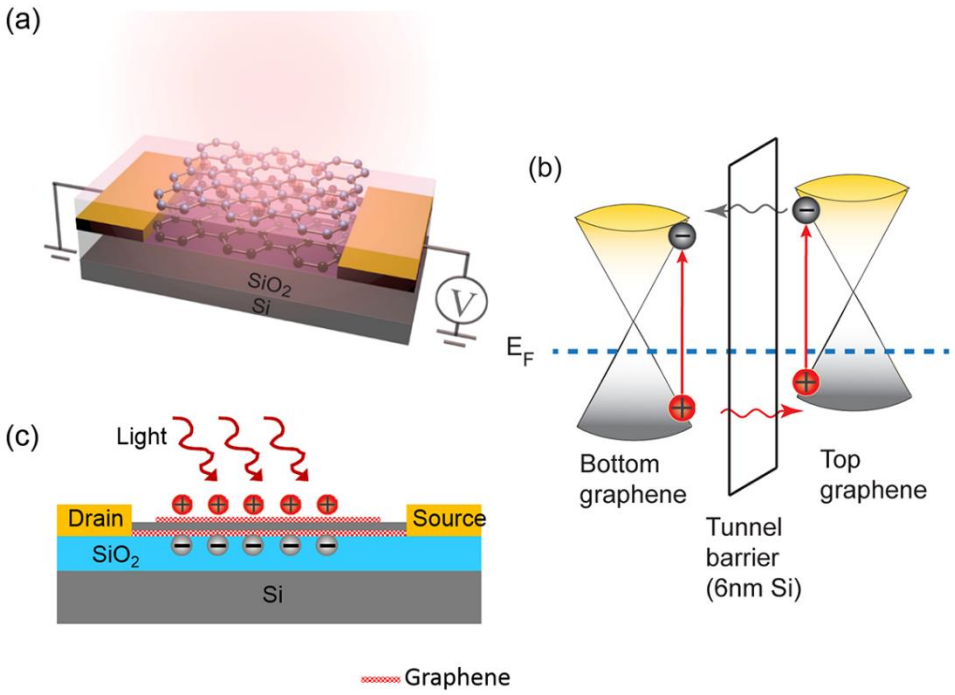

Figure 3.1 **The device structure and the mechanism of the double-layer graphene photodetector.** (a) The device structure. (b) The energy diagram and asymmetric tunneling under light illumination. (c) A schematic demonstrating the photogating effect under light illumination. (a) and (b) are adapted from Ref. 48.

The operating principle of the double-layer graphene photodetector can be understood from the band diagram shown in Figure 3.1(b). The top-layer graphene has heavier p-doping compared to the bottom-layer graphene. The average Fermi energy difference is ~0.12 eV, as determined from the gate-dependent transfer curves [48]. As a result of the doping difference, the energy band in the tunnel barrier is tilted due to charge transfer, which equilibrates the Fermi level of the two graphene layers. When light is absorbed by the two graphene layers, the tunneling of electrons and holes is asymmetric: Electrons tunnel preferentially from the top-layer graphene to the bottom-layer graphene, while holes tunnel preferentially from bottom to top, as indicated by Figure 3.1(b). After tunneling, because the tunneled electrons and holes are physically separated, they do not suffer from the ultrashort recombination time. They remain trapped in the separated two graphene layers for a period of time (denoted by τ_{lifetime}). This results in the photogating

effect, where the bottom graphene channel is gated by the top graphene under light illumination, as indicated by Figure 3.1(c).

Therefore, this device operates as a phototransistor with an optically controlled top gate. In a phototransistor, there is a so-called phototransistor gain that enhances the responsivity. The phototransistor gain originates from the fact that the photo-generated charges can remain trapped for a period of time and recirculate in the circuit many times. The phototransistor gain is given by $\tau_{\text{lifetime}}/\tau_{\text{transit}}$ [46], where τ_{lifetime} is the lifetime during which the tunneled carriers remain trapped in the two graphene layers; τ_{transit} is the transit time, which is related to the mobility of the channel material. Because of the high mobility of graphene, the transit time is small, which makes graphene an ideal material for utilizing the phototransistor gain [46]. It is worth emphasizing that because our approach of increasing responsivity does not reply on resonant behaviors like optical cavities or plasmonic structures, it preserves the ultra-broadband advantage of graphene, enabling ultra-broadband high responsivity photodetectors.

The operating principle described above is supported by direct measurement of the gate-dependent tunneling current [48]. We also scan a focused laser spot at different positions of the device while measuring the tunneling current, producing a 2D spatial mapping. The 2D spatial mapping shows that the tunneling current is generated from the overlapped region between the two graphene layers, further confirming the mechanism described above [48].

Section 3.3 Measurement of the infrared responsivity

To demonstrate the high responsivity across a broad spectrum, we characterize the double-layer graphene photodetector with different light sources from visible to mid-infrared ranges. We use continuous wave (CW) lasers at 532 nm, 800 nm and 900 nm wavelengths. For longer wavelengths, we use an optical parametric amplifier (OPA) and a difference frequency generation (DFG) system. The OPA is pumped by a 250 kHz Ti:sapphire regenerative amplifier (Coherent, RegA 9000), generating signal and the idler waves at wavelengths of 1.3 μm and 2.1 μm respectively. Both waves are sent to DFG to produce light with a wavelength of 3.2 μm. In the following I will describe only the optical

setup and experimental results at wavelengths of 1.3 μm, 2.1 μm, and 3.2 μm. Results of 532 nm, 800 nm, and 900 nm wavelengths can be found in Ref. 48.

The optical setup for characterizing the infrared response (wavelengths of 1.3 μm, 2.1 μm, and 3.2 μm) of the double-layer graphene photodetector is shown in Figure 3.2. It is a home-built infinite conjugate laser scanning microscope with a ZnSe objective lens (Edmund optics, 12 mm focal length). The graphene photodetector sample is placed on a 2D motorized stage with 100-nm position resolution (Newport MFA-PPD and VP-25XA). In order to focus precisely the laser spot onto the center of the graphene detector, we scan the 2D motorized stage and collect the reflected light with an auxiliary detector (Thorlabs DET10D or Infrared Associates, IS-2.0, depending on the wavelength), forming a 2D scanning reflective image to determine the exact position of the device. This method also allows us to measure precisely the laser spot size by scanning the laser spot across the edge of a metal contact. The power is calibrated by a thermopile broadband power meter (Melles Griot, 13PEM001). All the characterizations are done at room temperature with the graphene photodetector in vacuum to control the environmental doping of graphene. Another similar setup with scanning mirror is used for characterizing the graphene detector in the visible to near-infrared range [48,102].

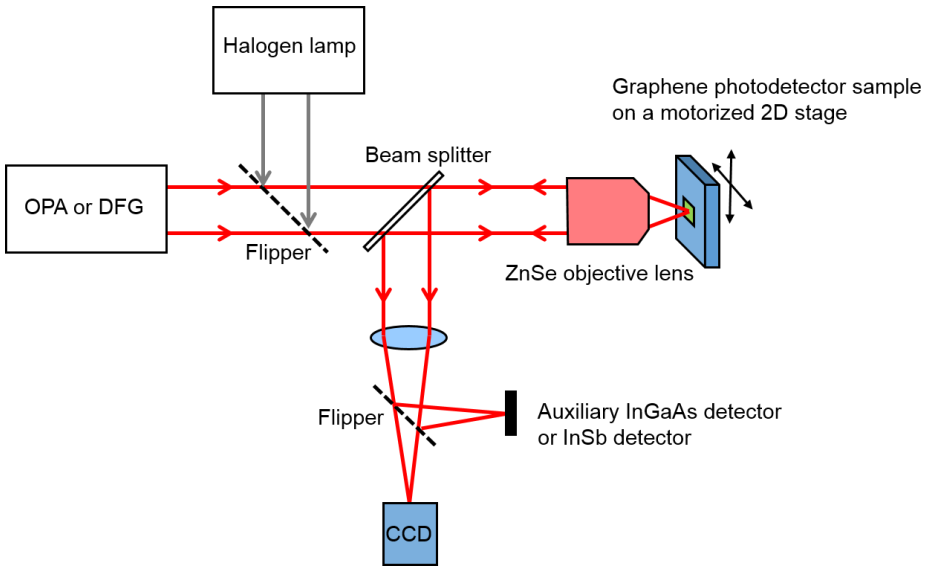

Figure 3.2 **The optical setup for characterizing the infrared response of the graphene photodetector.**

Figure 3.3 shows the response of the double-layer graphene photodetector when the illumination is at the wavelength of 1.3 μm. The minimum of the transfer curve (drain-source current as a function of back gate voltage V_g) shifts toward a more negative V_g value with the increase of laser power. Such a shift indicates an increase of n-doping. This observation supports the detection mechanism described in the previous section (see Figure 3.1): the asymmetric tunneling and the photogating effect provide n-doping to the bottom graphene channel. Similar shift in the transfer curves is observed when laser is at other wavelengths [48].

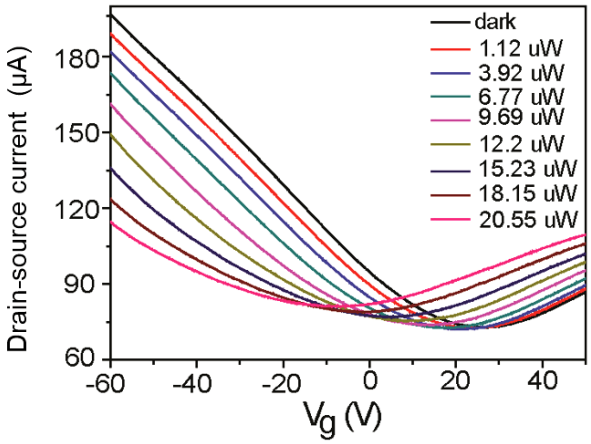

Figure 3.3 **The gate dependence of the drain-source current under different incident power.** The wavelength is at 1.3 μm. This figure is adapted from Ref. 48.

The photocurrent is obtained by subtracting the dark current from the drain-source current. In Figure 3.4(a-c) we show the gate dependence of the photocurrent at wavelengths of 1.3 μm, 2.1 μm, and 3.2 μm under different incident power. A 1.5 V drain-source bias voltage is applied to the bottom channel graphene. We can further calculate the power dependence of the photocurrent at different gate voltages, as shown by Figure 3.4(d-f). From the power dependence we observe a saturation of photoresponse at large incident power. This can be explained by the decrease of asymmetry in the band diagram (see Figure 3.1b) after opposite charges build up in the separated two graphene layers. From the measured photoresponse, we obtain responsivities of 4 A/W, 1.9 A/W, and 1.1 A/W at wavelengths of 1.3 μm, 2.1 μm and, 3.2 μm, respectively. This result demonstrates high

responsivity over a broad spectral range, which is much higher than the tens of mA/W^{-1} responsivity of many reported graphene-based detector [94-98].

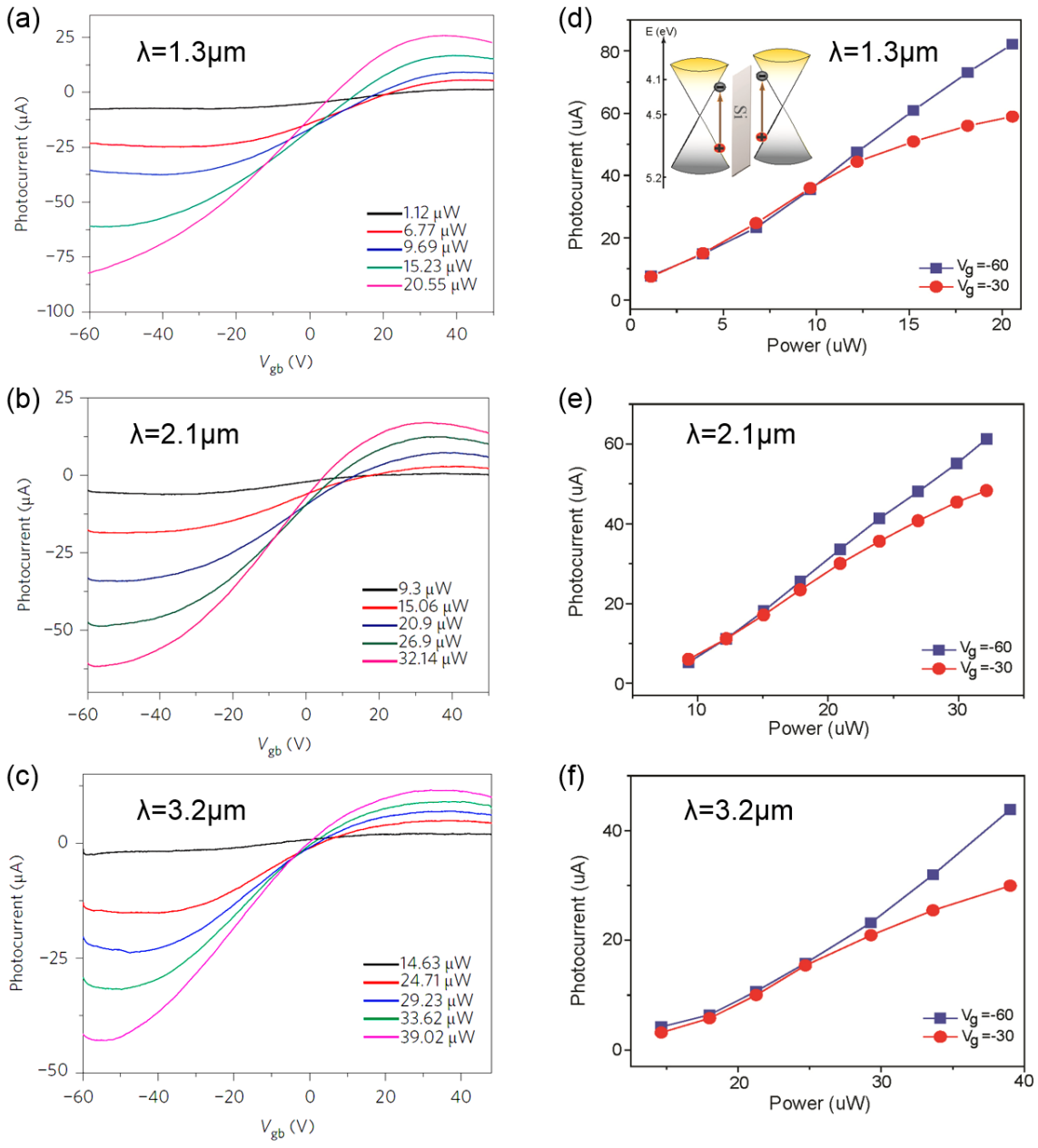

Figure 3.4 **The infrared response of the double-layer graphene photodetector.** (a-c) The gate dependence of the photocurrent under different incident power. (d-f) The power dependence of the photocurrent under different gate voltage. The wavelengths are at 1.3 μm (a,d), 2.1 μm (b,e) and 3.2 μm (c,f), respectively. This figure is adapted from Ref. 48.

Section 3.4 Temporal response with rest gate pulses

In the previous section, our measurements have demonstrated the high responsivity of the double-layer graphene photodetector. However, there is a trade-off between gain and operation speed, since we rely on τ_{lifetime}, the lifetime during which the tunneled carriers remain trapped in the two graphene layers, to boost the gain (see Section 3.2 and [46,47,103]). Therefore, the operation speed of our graphene photodetector is significantly slower than many other graphene photodetectors, which can have an ultrafast operation speed even up to 40 GHz [43].

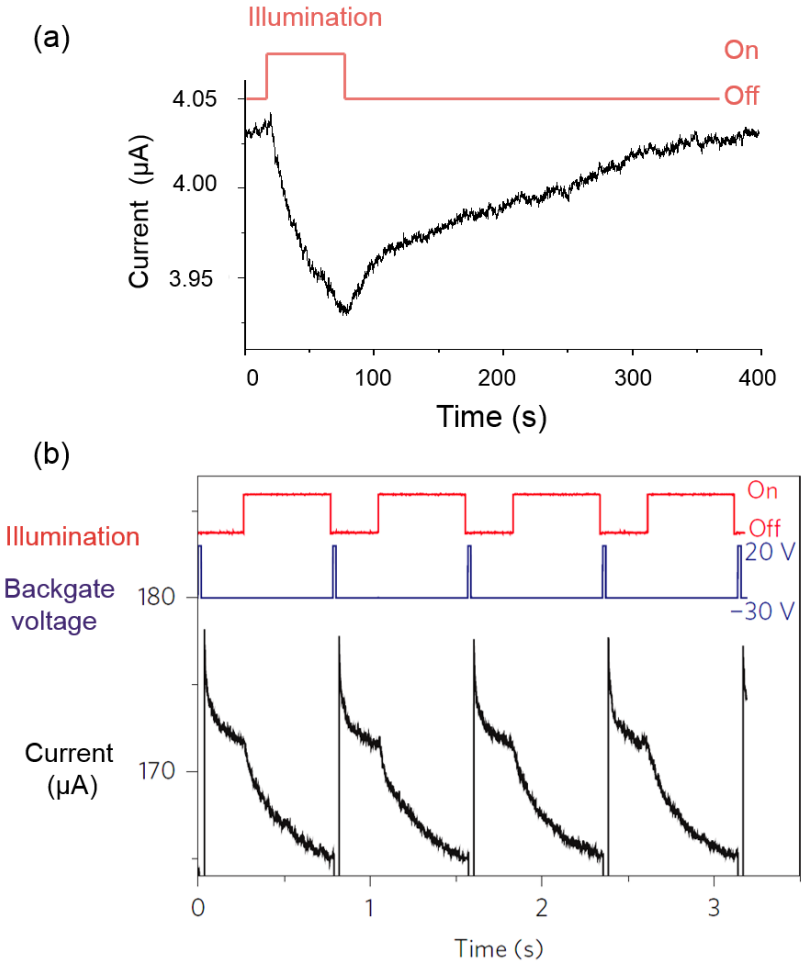

Figure 3.5 **The temporal response of the double-layer graphene photodetector** with (a) a constant back gate voltage and (b) with reset back gate pulses. The laser illumination is turned on and off by a mechanical shutter (light intensity shown by the red curves). In (b), the voltage pulses sent to the back gate is shown by the blue curve. The drain-source current is measured (black curve). This figure is adapted from Ref. 48.

Figure 3.5(a) shows the temporal response of our double-layer graphene photodetector. We turn on and off the laser illumination (λ=532 nm) with a mechanical shutter. From the shapes of the two curves in Figure 3.5(a), it is clearly seen that the measured current is not directly proportional to the illumination, which is different from common power detectors such as photodiodes. When the illumination is turned on and kept constant, the current changes gradually because the tunneled carriers continue accumulating in the two graphene layers and modifying the channel conductivity. When the illumination is turned off, it takes several hundred seconds for the trapped carrier in the two graphene layers to return to equilibrium. Therefore, the double-layer graphene photodetector is not a power detector with signal directly reflecting the incident power.

The slow operation speed can be improved with rest back gate pulses [46,47]. Positive back gate pulses can raise the Fermi level of the bottom channel graphene, facilitating the trapped electrons in the bottom graphene to move to the top graphene. In this experiment we use a voltage source (Keithley 2400 series) to produce 10 ms pulses, and we synchronize the pulses with the mechanical shutter such that the pulses are applied right after the shutter is off. The drain-source bias is 1V. As Figure 3.5(b) shows, the gate pulses quickly reset the channel conductivity (in this case to a larger value) and allow the graphene photodetector to make the next measurement. With the reset gate pulses, the graphene detector can operate with a speed of more than 1 Hz.

Section 3.5 Noise characterization and the noise-equivalent power

Noise-equivalent power (NEP) is one of the most practical figure of merit for photodetectors. It is defined as the optical power that yields a unity signal-to-noise ratio for a 1 Hz bandwidth, and can be calculated from the noise spectral density and responsivity [104]:

$$\mathrm{NEP} = \frac{\text{Noise spectral density}}{\text{Responsivity}}. \quad (1)$$

To obtain NEP, we first analyze the noise in the dark current waveform of the double-layer graphene photodetector. As shown in Figure 3.6(a), the dark current waveform is acquired

by a current preamplifier and a data acquisition card with a sampling rate of 10 kHz. The drain-to-source bias voltage applied to the bottom graphene layer is 1V in this measurement. The noise spectral density is defined as

$$S(f) = \lim_{T\to\infty} \frac{1}{\sqrt{T}} \sqrt{\left\langle \left| \int_{-T/2}^{T/2} I_{\mathrm{dark}}(t) e^{-i2\pi f t} dt \right|^2 \right\rangle}, \quad (2)$$

where $\langle\ \rangle$ denotes the expectation value, and $I_{\mathrm{dark}}(t)$ is the dark current waveform. The definition can be generalized to discrete finite sampling of the dark current $I_{\mathrm{dark}}(t_n)$:

$$S(f_n) = \frac{1}{\sqrt{F_S N}} \sqrt{\langle |\boldsymbol{I}_{\mathrm{dark}}(f_n)|^2 \rangle}, \quad (3)$$

where $\boldsymbol{I}_{\mathrm{dark}}(f_n)$ denotes the discrete Fourier transform of $I_{\mathrm{dark}}(t_n)$; F_S is the sampling rate; N is the number of data points. Notice that the Fourier transform used here is defined so that $S(f_n)$ is non-zero only at positive frequencies [105]. The unit of $S(f_n)$ is $A/Hz^{1/2}$. Figure 3.6(b) shows the noise spectral density calculated from Figure 3.6(a) using Eq. (3). We also confirm our measurement of noise spectral density with another instrument. We send the dark current to a fast Fourier transform (FFT) spectrum analyzer (Stanford Research Systems SR760). The measured noise spectral density is shown in Figure 3.6(c), which is consistent with the result in Figure 3.6(b).

NEP can be calculated using Eq. (1). The responsivity of graphene photodetector in the visible range can reach ~1000 A/W [48]. If the modulation frequency is 1 Hz, we can read from Figure 3.6(b-c) that the noise spectral density at this modulation frequency is ~ $10^{-8}\ A/Hz^{1/2}$, and therefore the NEP is ~ $10^{-11}\ W/Hz^{1/2}$. On the other hand, the responsivity in the infrared range (λ=1.3~3.2μm) is on the order of 1 A/W, which corresponds to a NEP of ~ $10^{-8}\ W/Hz^{1/2}$ at a modulation frequency of 1 Hz. The NEP values are comparable to commercial infrared detectors based on narrow-bandgap semiconductors.

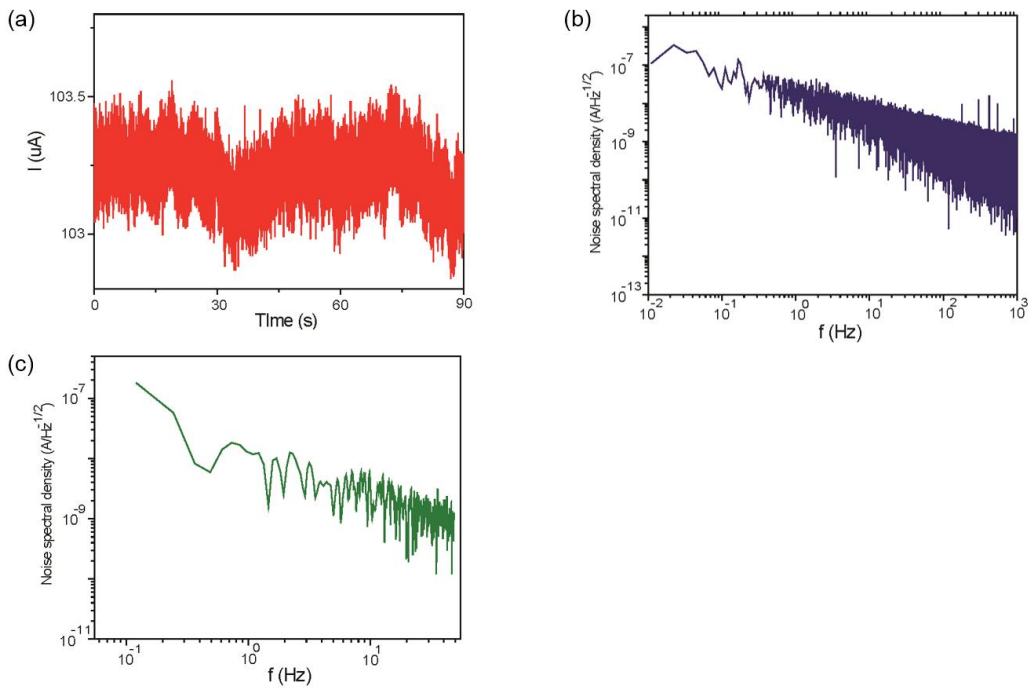

Figure 3.6 **The noise spectral density of the double-layer graphene photodetector.** (a) The dark current waveform. (b) The noise spectral density obtained by performing Fourier transform to the dark current waveform in (a). (c) The noise spectral density measured directly by using a commercial FFT spectrum analyzer. This figure is adapted from Ref. 48.

Section 3.6 Discussions

We have demonstrated that our double-layer graphene photodetector has high responsivity over a broad spectrum. There are several directions to further improve or modify the device for specific applications. To improve the NEP, the channel graphene can potentially be replaced with a semiconductor. Because a semiconductor has a bandgap, the dark current can be much smaller than graphene, and therefore the noise can be suppressed. Also, because the detection only requires very little absorption in graphene, it can be implemented as a transparent detector, by using a transparent substrate and a transparent gate electrode such as indium tin oxide (ITO) or graphene. The detector can also incorporate resonant plasmonic or antenna structures to further enhance the graphene absorption if the spectral bandwidth is not a concern. We will discuss in Chapter 6 that the responsivity can be enhanced with a photonic hypercrystal structure, which boosts the graphene absorption by guided resonance (see Section 6.5.2). Regarding the device physics, the detailed carrier dynamics of carrier tunneling, trapping, and equilibrating is

worth studying. With a better understanding of the carrier dynamics, it is possible to obtain a larger responsivity or a faster operation speed by further optimizing the material choice, thickness, and fabrication method of the tunnel barrier.

CHAPTER 4

Extraction of the complex optical conductivity of graphene by ellipsometry

Section 4.1 Chapter introduction

Two-dimensional (2D) materials have very distinct properties from their bulk counterparts [1-5]. As the dimension reduces from 3D to 2D, many important physical quantities require different descriptions. In particular, the refractive index is no longer well-defined in a truly 2D material, since the induced polarization per unit volume has rigorous definition only in 3D. A better physical quantity to describe the optical properties of a truly 2D material is its optical conductivity, which is associated with the induced surface current (see Section 1.3) [21-23]. Consequently, conventional methods of characterizing the optical properties of materials need modification. In this work, we develop a modified ellipsometry technique that can provide accurate and robust measurements of the optical conductivity of truly 2D materials.

The importance of characterizing the optical conductivity of 2D materials cannot be overemphasized. 2D materials have become unique building blocks for more complicated and sophisticated structures that create desired optical functionalities in optoelectronics and metamaterials [29,40,48,106,107]. Various 2D material-based optoelectronic devices, such as photodetectors and modulators, have been demonstrated. Examples include our works on the double-layer graphene photodetector and the photonic hypercrystal-graphene based optical modulator, which are reported in Chapter 3 and 6,

respectively. 2D material-based plasmonic structures and metamaterials have also been reported, including our work of graphene hyperbolic metamaterial [29], which will be discussed in Chapter 5. Reliable optical characterization of 2D materials is the key to realizing these devices and metamaterials. Accurate measurements of the optical conductivity is also important for testing theoretical predictions, from which we can gain knowledge of the underlying carrier physics.

The optical conductivity is a complex number, whose real part determines the loss. The real part is relatively easy to obtain by transmission or reflection measurements, which has been demonstrated in many previous works on graphene [26,108,109]. On the other hand, the imaginary part of the optical conductivity is closely related to many important phenomena in optics. For example, whether graphene supports transverse-electric (TE) or transverse-magnetic (TM) plasmons depends on the sign of the imaginary part of the optical conductivity (see Section 1.4.4) [58]. The imaginary part also determines the optical topological transition of a graphene-based hyperbolic metamaterial [29]. However, obtaining the imaginary part is not as straightforward as the real part, and in many cases (e.g. graphene) Kramers-Kronig relations is not applicable due to the broadband optical response. As a result, more sophisticated techniques have been developed to obtain the complex optical conductivity of 2D materials. For example, Li *et al.* extract the complex optical conductivity of graphene by carefully measuring the reflection and transmission together with the help of an interference layer and electrostatic gating [66]. However, such a technique requires additional fabrication steps, which is not always practical to the general need.

The technique we develop here is based on spectroscopic ellipsometry. More specifically, we modify the conventional data analysis in order to treat the truly 2D materials properly. In fact, ellipsometry has been used extensively to graphene in many previous works [110-115]. However, they have used a phenomenological approach that models graphene, just like any other bulk material, as a layer with a nonzero effective thickness and an effective refractive index. In contrast, we model a truly 2D material as an infinitely-thin sheet fully described by the surface conductivity. Our approach uses a

quantity with a clear physical definition, which allows a more direct connection to theoretical predictions and applications.

Experimentally, we have applied this technique to mono- and bilayer chemical-vapor-deposited (CVD) graphene, obtaining measurements of the optical conductivity from ultraviolet to mid-infrared wavelengths (from 230 nm to 7 μm). The mid-infrared properties are particularly interesting since graphene has been shown to be a good material for mid-infrared plasmonics and metamaterials [59,116]. We also study how chemical doping with nitric acid modifies the optical conductivity [28].

This work is published in *Applied Physics Letters* in 2014 [41]. In addition, it is the basis of a free data analysis software "Photonicvasefit" published on nanoHUB.org, which is developed in collaboration with Prof. Alexander V. Kildishev and Dr. Ludmila J. Prokopeva at Purdue University [117,118]. According to the record of nanoHUB.org, up to now this software have been used more than 600 times by users all over the world in the 2D material community.

Section 4.2 Basic principles of ellipsometry

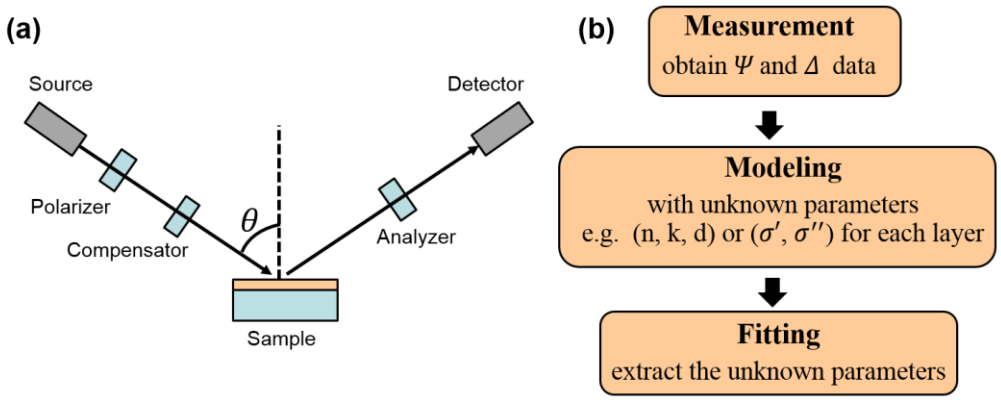

Figure 4.1 **Basic principles of ellipsometry.** (a) The schematic optical setup of a reflection ellipsometer. (b) The procedure of working with an ellipsometer.

Ellipsometry is the most accurate technique of measuring the optical constants and film thicknesses of a layered structure [119]. It is robust and requires no baseline correction or reference samples. Figure 4.1(a) shows the schematic setup of a reflection ellipsometer. Incident light with a controlled polarization state is sent to the sample, and the reflected

light is measured in the specular direction with an analyzer. With this setup, the ellipsometric angles Ψ and Δ, defined by $r_{\mathrm{p}}/r_s = (\tan\Psi)e^{i\Delta}$, can be obtained. Here r_{p} and r_{s} are the reflection coefficients for p and s light, respectively. In other words, an ellipsometer acquires the amplitude ratio and phase difference between r_{p} and r_{s}, rather than the absolute values of either. This is the reason why ellipsometry is a reference-free and robust technique. The measurement is insensitive to fluctuations of the light source and the environment.

When working with ellipsometry, measurement is usually straightforward and relatively simple, but the data analysis is key and rather complicated. The procedure is shown in Figure 4.1(b). First, we perform the measurement to obtain Ψ and Δ of the sample. This step is usually done at several different incident angles and at different wavelengths to obtain more information about the sample. Second, we need to model the Ψ and Δ of the layered structure in terms of analytical expressions that contain some unknown free parameters. In bulk materials, the unknown free parameters are usually refractive indexes and thicknesses, while in 2D materials, the complex conductivity is the unknown parameter. For simple samples with only one interface, the analytical expression can be derived from Fresnel equations, while for most more complicated layered structure, transfer matrix method is used to obtain the analytical expression. This second step is most important, which requires correct physical understanding of the sample as well as experience. In fact, the main contribution of our work is to propose the correct modeling of 2D materials, which will be discussed in Section 4.3. The third step is to fit the model to the acquired data of Ψ and Δ. By finding the values of the unknown parameters that minimize the error between the model and the experimental data, we obtain accurate numbers of these parameters.

Section 4.3 Modeling truly 2D materials

Figure 4.2(a) shows the conventional modeling in ellipsometry. For samples consisting of bulk layers, a model is constructed such that each layer is described by the refractive index (with real and imaginary parts) and the thickness. Actually, this conventional modeling has been applied to graphene by several groups to extract what they

call the effective refractive index of graphene [110-115]. However, such a modeling is phenomenological and lacks clear physical meaning. For a truly 2D material, it is more physical to model the layer by an infinitely thin sheet with an in-plane sheet optical conductivity σ, as shown in Figure 4.2(b). Interestingly, this is mathematically very similar to the treatment of metasurface, which will be discussed in Chapter 6. Here we discuss the simplest case where an infinitely thin sheet is sandwiched between semi-infinite medium 1 and medium 2. It can be extended to more complicated structures using the transfer matrix method. The reflection coefficients for s and p light can be derived by matching the boundary conditions of the Maxwell equations (see APPENDIX B):

$$r_{\mathrm{s}} = \frac{k_{1\mathrm{z}} - k_{2\mathrm{z}} - \sigma\omega\mu_0}{k_{1\mathrm{z}} + k_{2\mathrm{z}} + \sigma\omega\mu_0}\ , \quad r_{\mathrm{p}} = \frac{\varepsilon_1/k_{1\mathrm{z}} - \varepsilon_2/k_{2\mathrm{z}} - \sigma/\omega}{\varepsilon_1/k_{1\mathrm{z}} + \varepsilon_2/k_{2\mathrm{z}} + \sigma/\omega}\ , \tag{1}$$

where $k_{1\mathrm{z}}$, $k_{2\mathrm{z}}$ are the out-of-plane wave vectors in medium 1 and medium 2, respectively; ε_1, ε_2 are the permittivities of the two media. In an ellipsometric measurement of a 2D material, medium 1 and medium 2 are the air and the substrate. Eq. (1) is in fact a modified version of the Fresnel equation, which takes into account the surface conductivity at the interface. Ψ and Δ can therefore be calculated from Eq. (1) using the definition of $r_{\mathrm{p}}/r_{\mathrm{s}} = (\tan\Psi)e^{i\Delta}$. In this model, the real and imaginary parts of the optical conductivity σ are the unknown parameters of interest.

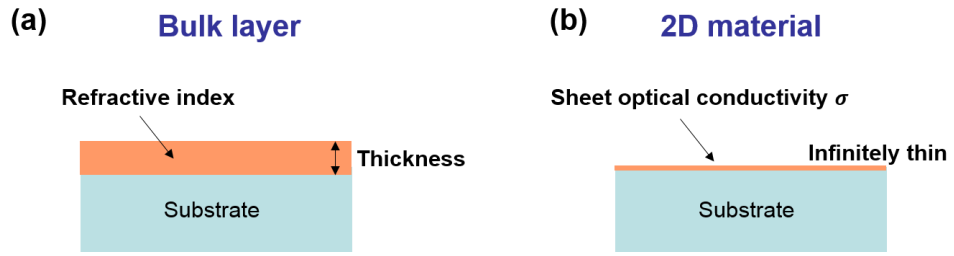

Figure 4.2 **Modeling a bulk layer (a) and a truly 2D material (b).**

Fitting the model to the experimental Ψ and Δ data gives the value of unknown parameters, which is done in MATLAB. In our MATLAB code, we apply the Marquardt-Levenberg algorithm to find the optical conductivity that minimizes the mean square error (MSE), which is defined by

$$\mathrm{MSE} = \sqrt{\frac{1}{3n-m}\sum_{i=1}^{n}\left[\left(N_i^{\mathrm{EXP}} - N_i^{\mathrm{MOD}}\right)^2 + \left(C_i^{\mathrm{EXP}} - C_i^{\mathrm{MOD}}\right)^2 + \left(S_i^{\mathrm{EXP}} - S_i^{\mathrm{MOD}}\right)^2\right]} \times 1000\,. \qquad (2)$$

Here n equals the number of wavelengths multiplied by the number of incidence angles acquired in the measurement; m is the number of fitting parameters; $N_i = \cos(2\Psi_i)$; $C_i = \sin(2\Psi_i)\cos\Delta_i$; $S_i = \sin(2\Psi_i)\sin\Delta_i$. The superscripts of EXP and MOD correspond to measured and model-predicted values, respectively. The subscript i indicates the particular set of data of a wavelength and an incident angle.

In our MATLAB code, the real and imaginary parts of the unknown optical conductivity σ as functions of wavelength are further parameterized. Because σ(λ) should be a smooth function, we have found that parameterization with cubic splines works very well. It is also usesful to parametrize σ(λ) with physical models that describes the dispersion of the 2D material [29], such as the analytical expression for graphene conductivity described in Section 1.3. We use transparent substrates in most experiments, whose refractive index is well described by the Sellmeier equation. The coefficients in the Sellmeier equation are obtained from measurements of bare substrates.

It should be noted that here we consider only the in-plane conductivity and neglect any out-of-plane response from the 2D material. This is justified for graphene, as *ab initio* calculation performed by our collaborators (private communication with Dr. JinLuo Cheng at University of Toronto) has shown that its out-of-plane conductivity is much weaker than the in-plane component.

Section 4.4 Experimental results of graphene conductivity

We report here the measurements on the optical conductivity of mono- and bilayer CVD graphene. The monolayer graphene is purchased from Bluestone Global Tech (Gratom-M-Cu); Bilayer CVD graphene is grown in-house by our collaborator [120]. Graphene layers are transferred onto CaF_2 substrates, which are transparent from ultraviolet to mid-infrared frequencies. It is worth noting that, although our technique can in principle be applied to arbitrary substrates, the choice of transparent substrates has advantages. Because transparent substrates have no absorption at the wavelengths of

interest, Δ from the bare substrates is either 0 or π. Any deviation from 0 or π can be unambiguously attributed to graphene, which aids the robustness of the optical conductivity extraction [110]. This is important because 2D materials usually have very small contribution to the measured quantities due to the atomic thickess. Using transparent substrates allows better extraction over a broad spectral range as long as the substrate maintains its transparency, while other contrast improvement methods in ellipsometry such as interference enhancement can only work in a narrow spectral range [113]. The substrates are wedged by 2º to avoid backside reflection; in this case because only one interface is present, the simple expression of Eq. (1) can be applied directly. To acquire data over a broader spectral range, we use two ellipsometers, Woollam M-2000 and Woollam IR-VASE, for wavelengths of 0.23 to 1.64 μm and 1.8 to 7μm, respectively. The longest wavelength is limited by the choice of CaF_2 substrates, which start to show some absorption at 8 μm. The angles of incidence used in the experiment are 47º, 57 º and 67 º. The spot size of M-2000 is about 3 mm by 5.5 mm at 57 degree. We mask the samples with scattering paper tissues (Kimwipes) for IR-VASE measurement because its spot size (8 mm by 20 mm at 57 degree) is larger than the graphene sample area (~ 10 mm by 10 mm). Bare CaF_2 substrates are measured and fitted by the Sellmeier equation to obtain the refractive index of CaF_2.

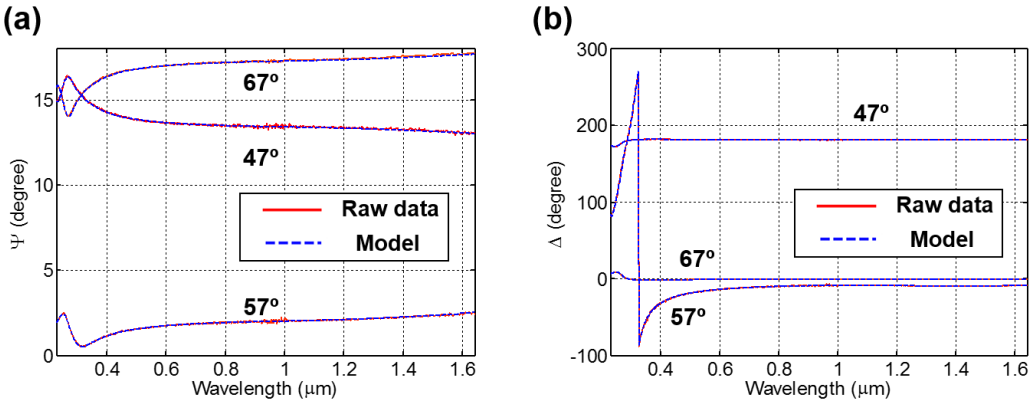

Figure 4.3 **The data and the fitting of the epllipsometry-based technique performed on monolayer graphene**. (a) The raw data of Ψ measured by Woollam M-2000 ellipsometer (red solid lines) and the Ψ values obtained by fitting our model to the data (blue dash lines). (b) The raw data of Δ measured by Woollam M-2000 ellipsometer (red solid lines) and the Δ values obtained by fitting our model to the data (blue dash lines).

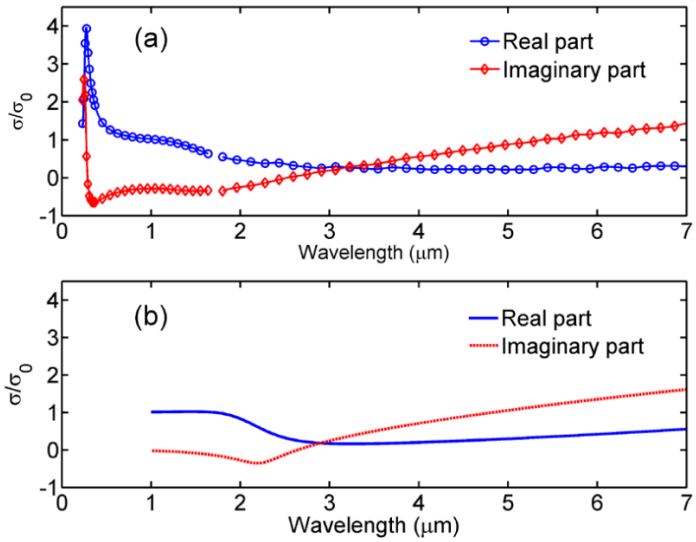

Figure 4.4 **The measured and the theoretical optical conductivity graphene.** (a) The extracted optical conductivity of monolayer CVD graphene. (b) The optical conductivity of monolayer graphene predicted by the non-interacting theory with a Fermi energy of 277 meV and a scattering rate (in units of energy) of 54 meV. The optical conductivity is normalized to the universal conductivity. The circles and diamonds are the control points of the cubic splines.

Figure 4.3 shows the raw data of Ψ and Δ acquired by Woollam M-2000 ellipsometer. By fitting with the analytical model described in Section 4.3, we can obtain very good match between the data and the model, as demonstrated by the figure. This is an indication that our model describes the 2D material very well. Figure 4.4(a) shows the optical conductivity of the monolayer CVD graphene extracted from the fit. The quality of the fit can be quantified by the MSE defined by Eq. (2). The MSEs of the M-2000 and the IR-VASE measurements shown in Figure 4.4(a) are 0.88 and 4.65 respectively, indicating good fitting quality. As shown in Figure 4.4(a), we observe a value of the optical conductivity very close to σ_0, the universal conductivity of graphene, around 1 μm. Also, there is a peak in the real part located at the wavelength of 270 nm (photon energy = 4.6 eV), which is associated with the exciton-shifted van Hove singularity at M point (see Section 1.3). These results are consistent with previous reports [24,26,108,110]. Notably, we obtain both the real and imaginary parts of the optical conductivity, while most previous works measure only the real part. To understand the measured conductivity, we plot in the Figure 4.4(b) the theoretical conductivity predicted by a non-interacting linear response theory (see Section 1.3) for comparison [21-23]:

$$\sigma(\omega) = \frac{\sigma_0}{2}\left(\tanh\frac{\hbar\omega+2E_F}{4k_BT} + \tanh\frac{\hbar\omega-2E_F}{4k_BT}\right) - i\frac{\sigma_0}{2\pi}\log\left[\frac{(\hbar\omega+2E_F)^2}{(\hbar\omega-2E_F)^2+(2k_BT)^2}\right] + i\frac{4\sigma_0}{\pi}\frac{E_F}{\hbar\omega+i\hbar\gamma}. \quad (3)$$

In Eq. (3), the first two terms and the third term are contributed by the interband and the intraband transition, respectively. σ_0 is the universal conductivity defined by $e^2/(4\hbar)$; E_F is the Fermi energy relative to the Dirac point (positive regardless of p-doing or n-doping); γ is the intraband scattering rate. Figure 4.4(b) is plotted with a Fermi energy of 277 meV and a $\hbar\gamma$ value of 54 meV, which provide the closest match to the measured optical conductivity. We plot only the infrared wavelengths, since the theory within the independent-particle picture does not work properly in the ultraviolet to visible range, where many-body corrections are required [26,27,110].

It should be noted that although the theory reproduces the main features of the measured optical conductivity, some details are different. In particular, the measured conductivity shows a smeared feature around 2 μm compared to the theoretical curves. A possible explanation is the presence of a non-uniform distribution of the Fermi energy within the measuring spot size, which is supported by Figure 4.5, the measurements performed with 10 times smaller spot size by using a focusing accessory of the M-2000 ellipsometer. In this figure, we perform the measurement at 5 different positions of the sample. The measured optical conductivity curves associated different positions overlap almost perfectly for wavelengths below 700 nm, but deviate in the long-wavelength side of the spectrum. This indicates that the Fermi energy measured at different positions are different, and there is a non-uniform distribution across the sample. Because the electrons are free to move within graphene, the Fermi levels at different positions must line up. Therefore, as represented by the inset of Figure 4.5, the inhomogeneity is actually a result of different potential energies at different positions. This can be due to a nonhomogeneous distribution of charged impurities or dopants. It is also possible to attribute part of the broadening around 2 μm in Figure 4.4(a) to the damping in the interband transition, which is not included in the theoretical conductivity described by Eq. (3).

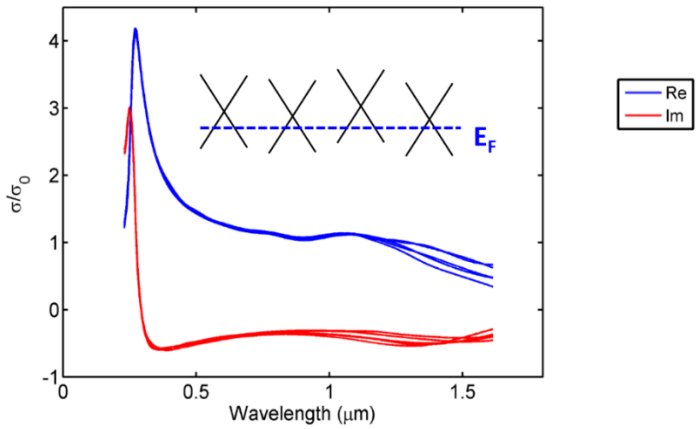

Figure 4.5 **The optical conductivity measured with a 10-times smaller spot size by using a focusing accessory.** Different curves correspond to the results obtained at different positions in the graphene sample. There are artificial fluctuations because the instrument signal-to-noise ratio is lower when using the focusing accessory. The inset represents the inhomogeneity in potential energy.

In Figure 4.6 we plot the extracted optical conductivity of mono- and bilayer CVD graphene versus photon energy. As expected for bilayer graphene, the real part of the conductivity approaches twice the universal conductivity for near-infrared photon energies. Notably, the M-point peak in the real conductivity of the bilayer graphene is at 4.4 eV, which is red-shifted from the 4.6 eV peak of monolayer graphene. The observed red shift of the exciton-shifted van Hove singularity is consistent with previous reported measurements and first-principle calculations for bilayer graphene [26,27]. In addition, the bilayer graphene shows a small peak at 0.4 eV in the real part of the conductivity, as indicated by the arrow in Figure 4.6 (b). This peak, associated with the interlayer coupling energy, has been observed in exfoliated bilayer graphene in the literature [26,121,122]. Compared with the reported exfoliated bilayer graphene results, the peak we observe in CVD bilayer graphene is less pronounced.

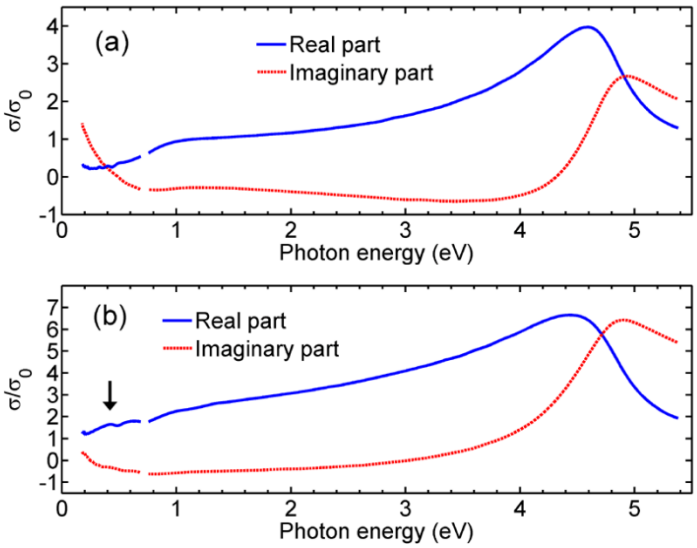

Figure 4.6 **The extracted optical conductivity of mono- and bilayer CVD graphene versus photon energy.** (a) The extracted optical conductivity of monolayer CVD graphene. (b) The extracted optical conductivity of bilayer CVD graphene. The optical conductivity is normalized to the universal conductivity. The arrow in part (b) indicates the peak at 0.4 eV associated with the interlayer coupling energy of bilayer graphene.

The samples reported in Figure 4.4, Figure 4.5 and Figure 4.6 are unintentionally p-doped by the environment. Our technique is also applied to study how chemical doping modifies the optical conductivity. Chemical doping is performed by placing the sample in a container with nitric acid vapor for 15 minutes [28]. The sample is then washed to remove excess nitric acid on the graphene surface. Figure 3 shows the optical conductivity of monolayer graphene before and after the chemical doping by nitric acid vapor. According to the theoretical conductivity described by Eq. (3), one way to obtain the Fermi energy is by identifying the photon energy of the local minimum in the imaginary conductivity [66]. The nitric acid chemical doping therefore pushes the Fermi energy to 530 meV (p-doped relative to the Dirac point), as the imaginary-part local minimum occurring at the wavelength of 1.16 μm corresponds to a photon energy of $2E_F$. The real part in the near-infrared region is decreased due to Pauli blocking. On the other hand, the optical conductivity at wavelengths below 0.6 μm shows negligible change. Although it has been reported that doping can modify the position and the shape of the exciton-shifted van Hove singularity peak, our doping change is not as strong as the electrolyte gating used in the literature to see this effect clearly [123]. Similar results with another dopant called magic blue will also be reported in Chapter 5.

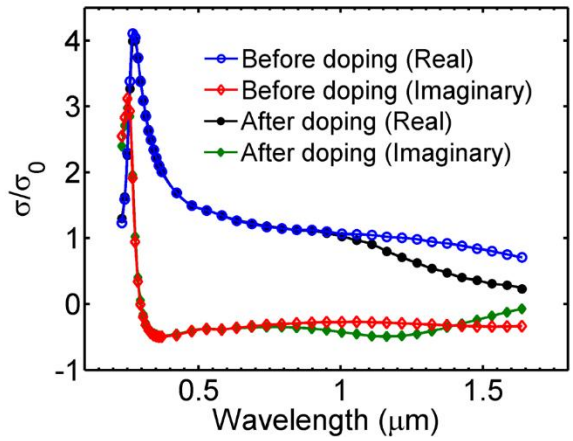

Figure 4.7 **The extracted optical conductivity of monolayer CVD graphene before and after chemical doping by nitric acid vapor.** The optical conductivity is normalized to the universal conductivity. The markers are the control points of the cubic splines.

Section 4.5 Discussion

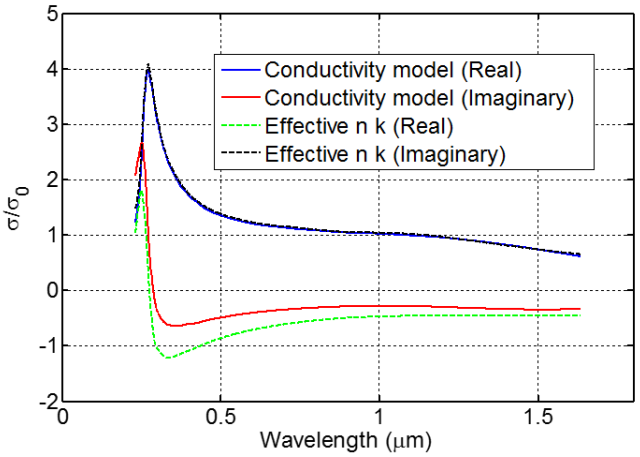

Figure 4.8 **The optical conductivity extracted from the same set of experimental data using different modeling approaches.** The solid lines are obtained using the model developed in this work. The dash lines are obtained using the conventional bulk-layer model.

In this chapter we have demonstrated a technique based on spectroscopic ellipsometry that measures the complex optical conductivity of 2D materials. In our technique, 2D materials are described by the optical conductivity, in contrast to the conventional approach that models the material phenomenologically with an effective refractive index and an effective thickness [110-115]. We emphasize that although the effective refractive index can be converted into optical conductivity, the results obtained in this way is not correct. This is because a 2D material has very different in-plane and out-

of-plane responses, and therefore modeling it as an isotropic material with an effective refractive index is not appropriate. Although it is possible to model the layer with anisotropic refractive indexes and an effective thickness, the increase of the number of unknowns is not economic in fitting and can result in unstable fitting. Figure 4.8 shows the optical conductivity extracted from the same set of experimental data using different modeling approaches. The solid lines are obtained using the modeling developed in this work. The dash lines are obtained by modeling graphene conventionally as an isotropic layer with an unknown effective refractive index and a fixed thickness d of 3.35 Å [110]. After extracting the effective refractive index n, it is converted to conductivity using

$$\sigma = \omega d \varepsilon_0 [\varepsilon_2 + i(1 - \varepsilon_1)], \tag{4}$$

where $\varepsilon_1 + i\varepsilon_2$ is the relative permittivity, which equals n^2. We can see from Figure 4.8 that the conventional modeling gives correct real part but incorrect imaginary part of the optical conductivity. Therefore, our modeling approach should be used for truly 2D materials, especially when the imaginary part of the conductivity needs to be determined accurately.

CHAPTER 5

Mid-infrared graphene hyperbolic metamaterials

Section 5.1 Chapter introduction

Section 5.1.1 Materials with hyperbolic dispersion

Hyperbolic materials are anisotropic materials in which the permittivities associated with different polarization directions exhibit opposite signs [124-126]. Such anisotropic behavior results in an isofrequency surface in the shape of a hyperboloid, as plotted in Figure 5.1(d). In general, arbitrary optical waves can be expanded by plane waves (denoted by $e^{i\mathbf{k}\cdot\mathbf{r}}$). The points on an isofrequency surface represent the $\mathbf{k}$ vectors of all plane waves allowed to propagate in the material at a given frequency. Figure 5.1 shows the isofrequency surfaces and the corresponding dispersion relations of air, isotropic materials, elliptical anisotropic materials and hyperbolic materials. We can see that hyperbolic materials support plane waves with extremely high k values (the so-called high-k modes), and as a result of the large surface area of the isofrequency surface, hyperbolic materials exhibit an enhanced photonic density of states (PDOS). Many interesting applications have been enabled by hyperbolic materials. For example, the spontaneous emission rate of quantum emitters can be modified if they are brought close to a hyperbolic material [127], and similarly, the scattering cross section of small scatters near a hyperbolic material is enhanced [128]. The near-field radiative heat transfer associated with hyperbolic materials becomes super-Planckian [129]. Also, the propagating high-k modes supported by hyperbolic materials have been exploited to achieve sub-diffraction-limited

images using a hyperlens [130], and to create cavities with deep subwavelength dimensions [131].

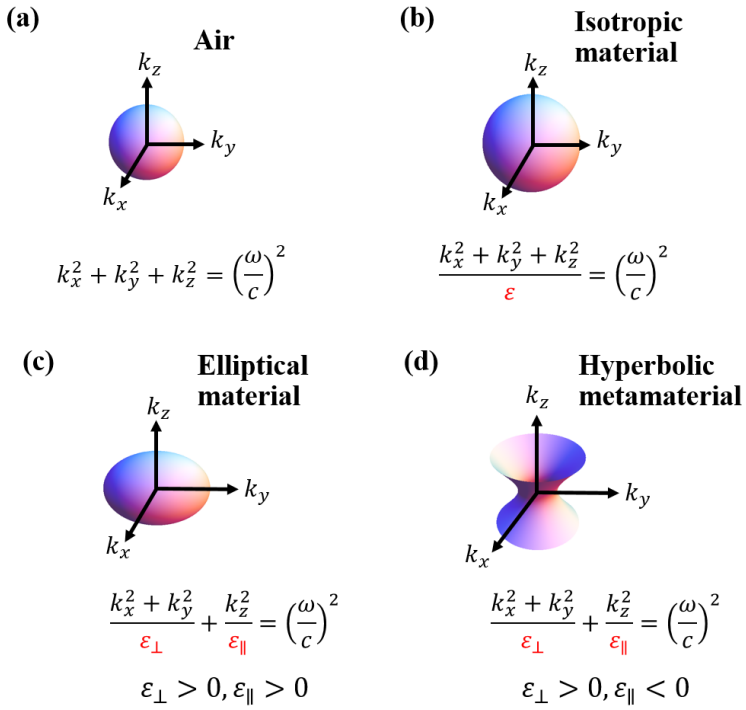

Figure 5.1 **Isofrequency surfaces and dispersion relations for air (a), an isotropic material (b), an elliptical anisotropic material (c), and a hyperbolic material (d).**

There are natural materials such as bismuth, graphite and hexagonal boron nitride, which exhibit hyperbolic dispersion in specific spectral ranges [132-134]. In particular, we will report in Chapter 6 a photonic hypercrystal-based perfect absorber, in which we use hexagonal boron nitride as the hyperbolic material. Another way to obtain hyperbolic dispersion in materials is by making metamaterials, which will be discussed in the next section.

Section 5.1.2 Hyperbolic metamaterials

The advances of metamaterials and metasurfaces have enabled the creation of artificial materials with various desirable properties [11,12,135,136]. These artificial metamaterials consist of carefully engineered structures that are small enough to be homogenized into effective media. By designing the constituent structures, we are no longer restricted by the material properties given by nature, and can even create extreme properties such as negative refractive index, epsilon-near-zero or large nonlinearity [137-

139]. Among artificially-structured materials, hyperbolic metamaterials (HMMs) are designed to attain effective media in which the permittivities in different directions have opposite signs. Therefore, HMMs exhibit the hyperbolic isofrequency surface plotted in Figure 5.1(d). Because HMMs are engineered materials, the hyperbolic dispersion can be designed for the particular wavelengths of interest, which opens up new applications beyond what natural hyperbolic materials are capable of.

HMMs are most commonly realized with two categories of structures: metal-dielectric multilayers [127,130,131] and metallic nanorod arrays [140]. The former structure can be fabricated layer by layer using vapor deposition, and the latter is often obtained by electrochemical deposition of a metal on porous anodic aluminum oxide. In both cases, metal is the essential element to provide the conducting electrons that make the extreme anisotropicity possible. Metals can also be replaced by doped semiconductors for realizing HMMs in the infrared range [141]. In this work, we explore another possibility — realizing HMMs with graphene-dielectric multilayers.

Section 5.1.3 Motivation for graphene HMM

While metal is the most common conducting constituent element for metamaterials, graphene provides another useful building block, i.e., a truly two-dimensional (2D) conducting sheet whose conductivity can be controlled by doping. In this work, we explore the realization of a particular HMM, in which the role of the metal in providing a conducting layer is taken over by graphene [29,106,107,142-144,145-147]. Graphene is a 2D semimetal with a thickness of only one atom [1,2]. It has been shown that doped graphene is a good infrared plasmonic material in terms of material loss [59]. As a truly 2D material that only conducts in the plane, graphene by nature has the anisotropicity required for HMMs. As the thinnest material imaginable, graphene also makes an ideal building block for multilayer structures, as it enables the minimum possible period and therefore the highest possible cutoff for the high k-modes [142,148], which has been limited in metal and semiconductor-based HMMs by the non-negligible thickness of those materials. The conductivity of graphene, unlike that of metals, can be effectively modulated by electrical gating (see Section 1.4.1 and Section 5.5). This unique advantage has been demonstrated in other graphene-based metamaterials [149], and can potentially be

exploited to realize a tunable HMM in which the PDOS can be controlled electronically on demand. In addition, graphene shows much richer optoelectronic behavior than metals, and the massless Dirac quasiparticles in graphene also give rise to very different carrier dynamics compared to other semiconductors. Various photodetection mechanisms, such as photothermoelectric, photovoltaic, bolometric, photo-gating, and photo-Dember effects, have been demonstrated with graphene (see Section 1.4.2) [44,45,48,49]. Graphene multilayer structures can therefore serve as a unique platform in optoelectronics, which incorporates the unusual photonic behavior of HMMs into graphene detectors or other optoelectronic devices.

In this work we report the first experimental realization of a multilayer structure of alternating graphene and Al_2O_3 layers, a structure similar to the metal-dielectric multilayers commonly used in creating visible-wavelength HMMs. In fact, before our work there have been a large body of theoretical work on graphene-based HMM with similar structures [29,106,107,142-144,145-147]. The main contribution of our work is the development of practical design, experimental realization and sample characterization. We demonstrate that the fabricated metamaterial experiences an optical topological transition from elliptic to hyperbolic dispersion. The results of this work are published in *Nature Communications* in 2016 [29].

Section 5.2 Effective-medium approximation

Section 5.2.1 Theory

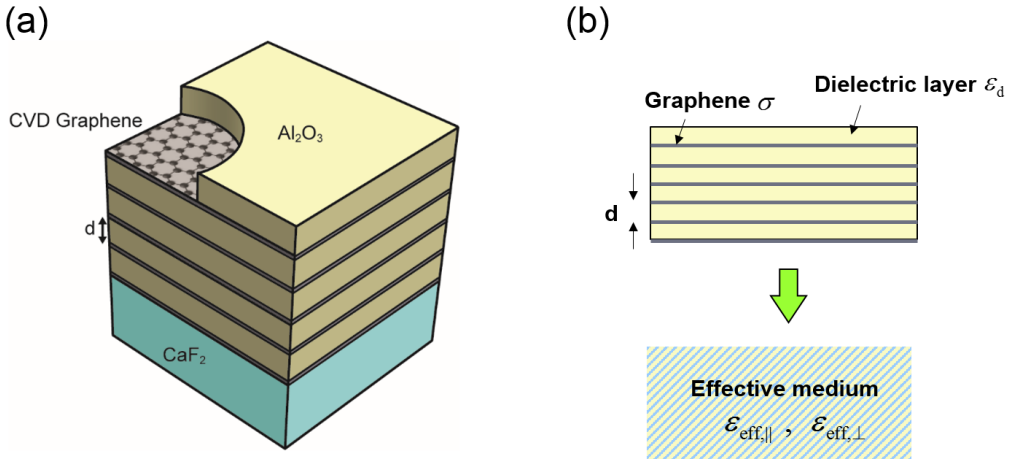

Figure 5.2 **Graphene hyperbolic metamaterial.** (a) The schematic of the graphene hyperbolic metamaterial, which consists of graphene-dielectric multilayers. (b) A schematic representing the homogenization of the graphene-dielectric multilayers into an effective medium.

The advances of metamaterials and metasurfaces are particularly enabled by the homogenization methods, which allow for intuitive understanding and easy prediction for complicated structures. Various homogenization methods have been developed to obtain the effective properties of complicated structures [150-152]. In the case of our graphene HMM, the homogenization is rather straightforward because of the simple layered structure. Figure 5.2 shows the structure of the graphene HMM, which consists of alternating dielectric and graphene layers. The graphene-dielectric multilayer structure can be homogenized and viewed as a metamaterial using the effective medium approximation (EMA), as represented by Figure 5.2(b). To derive the effective parameters, we start with the dispersion of the TM-polarized Bloch wave supported by this periodic structure (see APPENDIX C for the derivation), which is given by

$$\cos(Kd) = \cos(k_d d) - i\frac{\sigma Z_0}{2\varepsilon_d}\left(\frac{k_d}{k_0}\right)\sin(k_d d). \tag{1}$$

K is the Bloch wave vector; $k_d = \sqrt{\varepsilon_d k_0^2 - k_t^2}$; $k_0 = 2\pi/\lambda$ and k_t is the transverse wave vector; ε_d is the permittivity of the dielectric layer; d is the dielectric thickness; σ is the optical conductivity of graphene. Z_0 is the vacuum impedance. Here we have treated

graphene as an infinitely thin layer fully described by its in-plane sheet conductivity, which is appropriate for truly 2D materials like graphene. In the long-wavelength limit ($Kd \ll 1$ and $k_d d \ll 1$), Eq. (1) can be simplified to

$$\frac{k_t^2}{\varepsilon_{eff,\perp}} + \frac{K^2}{\varepsilon_{eff,\parallel}} = k_0^2 \,, \tag{2}$$

with the effective out-of-plane and in-plane permittivities given by

$$\varepsilon_{eff,\perp} = \varepsilon_d,$$

$$\varepsilon_{eff,\parallel} = \varepsilon_d + i\frac{\sigma Z_0}{2\pi}\left(\frac{\lambda}{d}\right). \tag{3}$$

The long-wavelength approximation made here is especially accurate in our case because $d/\lambda <$ 1/300 ($d \sim$ 10 nm and $\lambda >$ 3μm in our sample). Eq. (3) is derived for TM polarization. Similar homogenizing procedure can be repeated for the TE polarization, in which case both the effective in-plane and out-of-plane permittivities are given by $\varepsilon_d + i\sigma Z_0(\lambda/d)/(2\pi)$. As a result, the graphene-dielectric multilayers form a uniaxial anisotropic metamaterial. It is worth noting that Eq. (3) can also be derived quasi-statically by averaging the surface current in graphene and the transverse displacement current in the dielectric within a unit cell, which is done in APPENDIX D.

Here we focus our discussion on the TM polarization because it exhibits the interesting anisotropicity that enables hyperbolic dispersion. As indicated by Eq. (3), the out-of-plane permittivity $\varepsilon_{eff,\perp}$ is the same as the constituent dielectric and is always positive. This is because graphene is a truly 2D material that only conducts in plane. On the other hand, the in-plane permittivity $\varepsilon_{eff,\parallel}$ can be negative if

$$\text{Im}\,\sigma > 2\pi(d/\lambda)(\varepsilon_d/Z_0). \tag{4}$$

When this criterion is satisfied, the long-wavelength isofrequency surface described by Eq. (2) becomes a hyperboloid, and we obtain a HMM. Such an isofrequency surface allows the existence of propagating high-k modes, which can be traced back to coupled plasmon modes in the graphene-dielectric multilayer structure [107]. The criterion described by Eq. (4) determines the wavelength at which the optical topological transition between elliptical

and hyperbolic dispersions occurs. In addition, the real part of the optical conductivity should be as small as possible, since it contributes to the loss in the HMM.

Section 5.2.2 Validity of effective-medium approximation

In the previous section, EMA is derived for an infinite periodic system, but an actual metamaterial sample must have finite number of periods (5 periods are used in our sample). Therefore, it is important to examine the validity of EMA, especially the dependence on the number of periods in the multilayer structure. In addition, it is clear that the validity of EMA also depends on the wave vectors, because as K and k_t increase, the long-wavelength approximation from Eq. (1) to Eq. (2) eventually breaks down. Here we discuss the validity of EMA in the low-k and the high-k regimes separately.

As will be discussed in Section 5.4, we characterize the metamaterial with an infrared ellipsometer. An ellipsometer probes the low-k modes of the metamaterial, as it measures the sample with free-space plane waves, and the transverse wave vector k_t associated with free-space plane waves is very small ($k_t d = k_0 \sin\theta d \ll 1$, where θ is the angle of incidence). Therefore, an ellipsometer is an appropriate tool to probe the effective permittivity of a metamaterial. This is because in the low-k regime, we can accurately take the long-wavelength limit to homogenize the metamaterial, as we did to obtain Eq. (2) from Eq. (1).

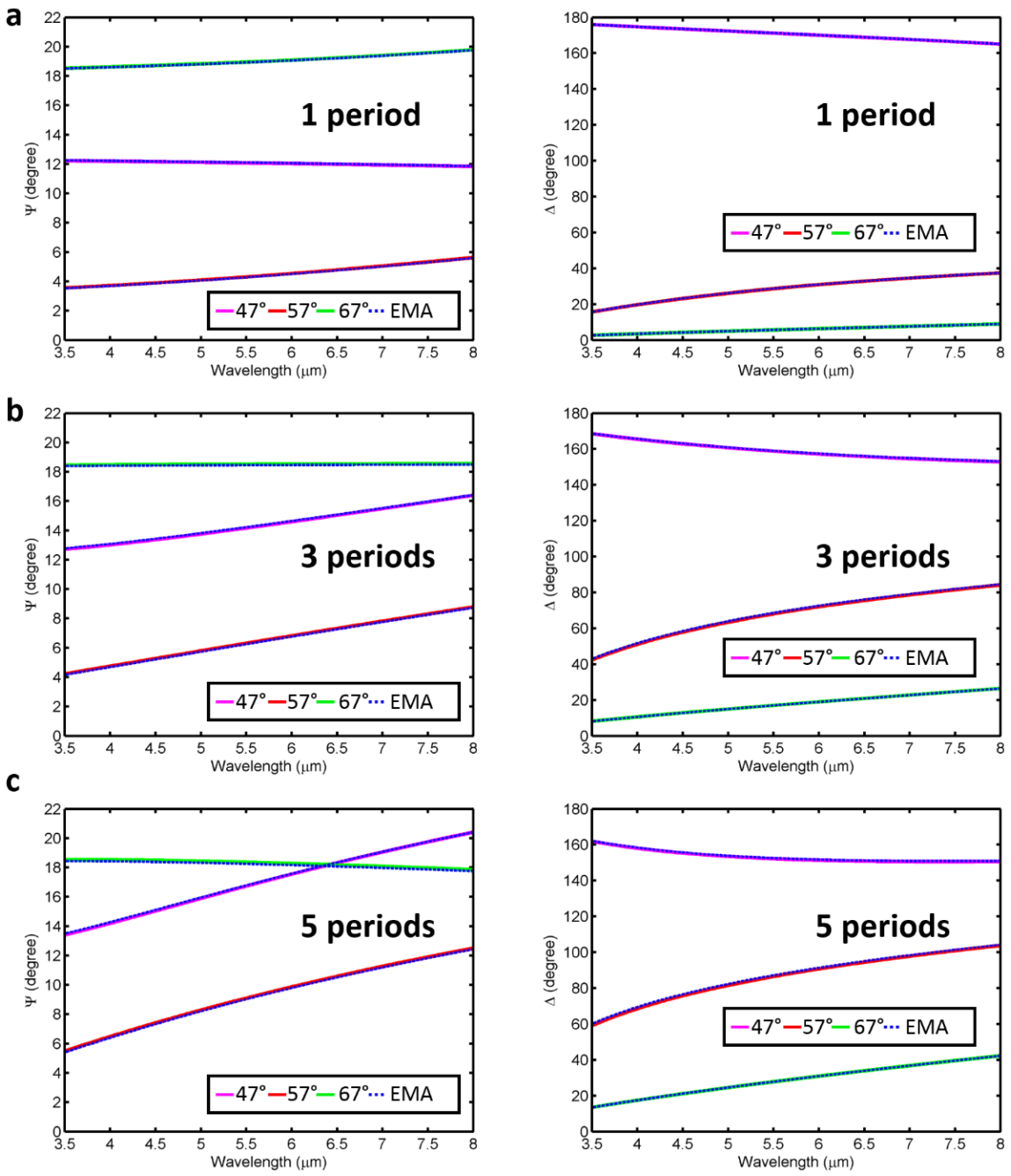

Figure 5.3 **Calculation of the ellipsometric angles Ψ and Δ for 1-period, 3-period and 5-period structures on a CaF_2 substrate.** (a), (b), and (c) correspond to 1-period, 3-period and 5-period structures, respectively. The calculation is performed for incident angles of 47º, 57 º and 67 º. For all structures, the solid lines, which are calculated with the exact transfer-matrix method, match very well with the dash lines, which are obtained with the EMA. The parameters used in the calculation are the same as the experimental conditions described in Figure 5.8.

To study the validity of the EMA in the low-k regime probed by an ellipsometer, we simulate the ellipsometric angles Ψ and Δ, the quantities an ellipsometer acquires, with two methods: the transfer-matrix method that calculates graphene-dielectric multilayer structure rigorously and the EMA that homogenizes the structure into an anisotropic layer. The results are shown in Figure 5.3, in which samples with 1-period, 3-period and 5-period structure on a CaF_2 substrate are calculated. We find that in the low-k regime, EMA can reproduce the optical properties accurately even for one period of the graphene-dielectric unit cell. It is worth noting that the highly accurate match between the EMA and the rigorous calculation is remarkable, which is not often observed in other metamaterials. This can be attributed to the fact that the period of the graphene HMM is so small ($d/\lambda < 1/300$ in our case) that the quasi-static limit is reached satisfactorily (see APPENDIX D). Furthermore, Figure 5.3 implies that the effective permittivities of a graphene HMM retrieved from a low-k measurement such as ellipsometry are independent of the number of layers. Similar result showing that low-k optical properties are insensitive to the number of periods has also been reported in the literature for HMMs made of metal-dielectric multilayers [153]. This is very different from what has been reported for fishnet negative-index metamaterials [135,154], in which the coupling between layers can in some cases significantly alters the effective parameters, and therefore a sufficient number of layers must be chosen in order to reach the convergence of the effective optical properties.

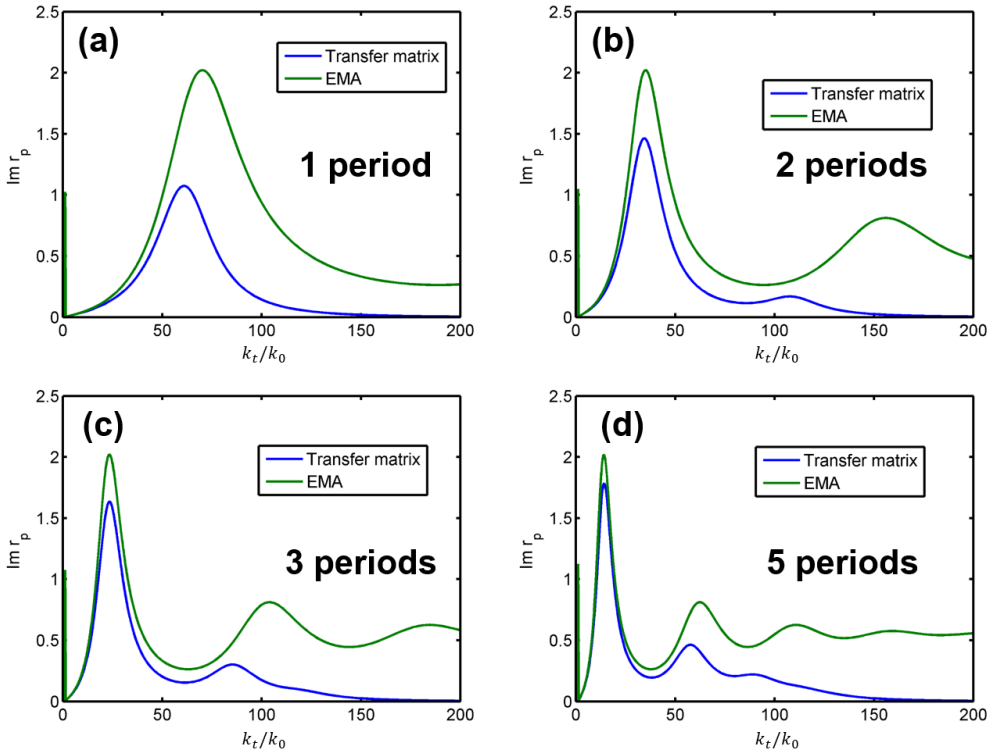

Figure 5.4 **Calculation of Im r_p, the imaginary part of the Fresnel reflection coefficient, in the high-k regime.** (a), (b), (c) and (d) correspond to 1-period, 2-period, 3-period and 5-period structures on a CaF_2 substrate, respectively. The blue and green lines are calculated by the transfer-matrix method and EMA respectively. The parameters used in the calculation are the same as the experimental conditions in Figure 5.8. The wavelength is 7 μm.

In spite of the high accuracy of the EMA in the low-k regime, it is still necessary to examine the EMA in the high-k regime. In fact, the high-k regime is where the real interest of HMM lies, as the enhanced PDOS and subwavelength imaging all rely on the existence of propagating high-k modes. In particular, we need to investigate how the number of periods influences the high-k optical properties. The existence of propagating high-k modes in HMM can be manifested by the nonzero Im r_{p}, the imaginary part of the Fresnel reflection coefficients for p-light [106,148], which is directly connected to the Purcell factor. In Figure 5.4 we show the calculation of Im r_{p} in the high-k regime as the function of the transverse k-vector k_t for 1-period, 2-period, 3-period and 5-period structures. As shown by all panels in Figure 5.4, the EMA overestimates Im r_{p}, and the correct value calculated by the transfer-matrix method experiences a cut-off for large k_t/k_0. This is because when k_t/k_0 becomes large enough, the long-wavelength assumption eventually breaks down. Comparing different panels in Figure 5.4, we see that

by increasing the number of layers, the results from the EMA become closer to the transfer-matrix method calculations before the cut-off. In our experimental realization, we choose to make 5 periods, which can provide optical properties reasonably close to the effective medium up to $k_t \approx 50k_0$.

Section 5.3 Design and fabrication of graphene HMM

Section 5.3.1 Design

As indicated by Eq. (3) and (4), graphene with a large positive Im σ and a small Re σ is desirable in realizing a HMM. Therefore, it is important to look at the optical conductivity of graphene in order to design the multilayer structure properly. While most previous theoretical work has concentrated on using high-mobility graphene, which is often obtained by mechanical exfoliation or epitaxial growth, we use chemical-vapor-deposited (CVD) graphene because it is the most realistic choice for practical fabrication of a multilayer structure [155]. Growth of large area CVD graphene is well-established, and it can be transferred onto arbitrary surfaces. In spite of its advantage in fabrication, CVD graphene often has a higher degree of disorder, which is manifested by its reduced mobility (usually on the order of thousands $\mathrm{cm^2\,V^{-1}\,s^{-1}}$). As a result of the lower crystal quality, the stronger carrier scattering in typical polycrystalline CVD graphene enhances the free-carrier absorption at THz frequencies, which can be understood from the theoretical optical conductivity of graphene (see Section 1.3) [21-23]

$$\sigma(\omega) = \frac{\sigma_0}{2}\left(\tanh\frac{\hbar\omega+2E_\mathrm{F}}{4k_\mathrm{B}T} + \tanh\frac{\hbar\omega-2E_\mathrm{F}}{4k_\mathrm{B}T}\right) - i\frac{\sigma_0}{2\pi}\log\left[\frac{(\hbar\omega+2E_\mathrm{F})^2}{(\hbar\omega-2E_\mathrm{F})^2+(2k_\mathrm{B}T)^2}\right] + i\frac{4\sigma_0}{\pi}\frac{E_\mathrm{F}}{\hbar\omega+i\hbar\gamma}, \quad (5)$$

where σ_0 equals $e^2/(4\hbar)$, E_F is the Fermi energy relative to the Dirac point (positive regardless of p-doping or n-doping), and γ is the intraband scattering rate. In this expression, the first two terms correspond to interband transitions, while the third term is the Drude-like intraband conductivity. Figure 5.5 shows the plot of the theoretical optical conductivity given by Eq. (5) with parameters typical for doped polycrystalline CVD graphene.

To realize a good HMM, we need graphene with a large positive imaginary conductivity to interact with light, but with a small real conductivity to minimize the material loss. As indicated by Figure 5.5, graphene is lossy at high frequencies when $\hbar\omega > 2E_F$ due to interband transitions. On the other hand, at low frequencies when $\hbar\omega \lesssim \hbar\gamma$, graphene also exhibits a large loss due to the intraband free-carrier absorption enabled by scattering. Because CVD graphene typically has a $\hbar\gamma$ of tens of meV, it is a lossy material at THz frequencies [56]. As shown by Figure 5.5, however, there is a spectral range between the two lossy regions such that the imaginary part of the conductivity exceeds the real part. As this spectral range lies in the mid-infrared part of the spectrum, CVD graphene-based HMM operates better in the mid-infrared than the THz region. Also, Figure 5.5 indicates that doping can improve the properties of graphene for realizing a HMM. A large E_F can turn off the interband absorption by the Pauli blocking and increase the Im σ required for achieving negative $\varepsilon_{\text{eff},\parallel}$. Furthermore, doping can also suppress the intraband scattering by screening charged impurities [56,156].

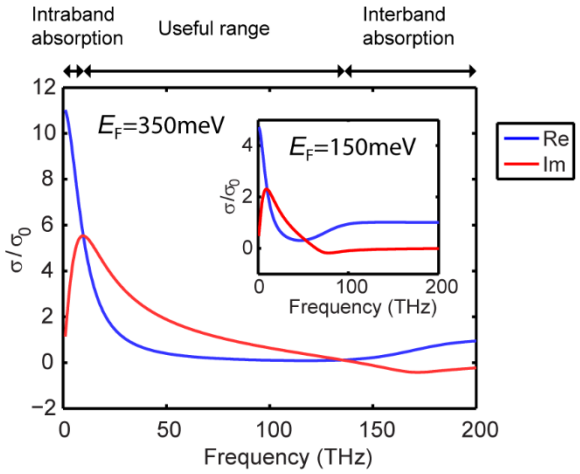

Figure 5.5 **The theoretical optical conductivity of graphene.** It is plotted with E_F = 350 meV and $\hbar\gamma$ = 40 meV. These numbers correspond to heavily-doped CVD graphene. At the high-frequency end of the spectrum, graphene is lossy because of the interband absorption. At the low-frequency end, graphene is again lossy due to the intraband free-carrier absorption. There is a useful spectral range in between, where the imaginary part of the optical conductivity exceeds the real part. In this particular example, the useful wavelengths range from 2 to 30 μm in the mid-infrared. The inset shows another example of lightly-doped CVD graphene with E_F = 150 meV and $\hbar\gamma$ = 40 meV. The useful wavelength range is smaller when the doping is lower.

Therefore, we design the graphene-dielectric multilayer structure shown in Figure 5.2(a) such that it operates as a HMM in the mid-infrared range. The structure consists of 5 periods of alternating CVD graphene and dielectric spacers. We choose Al_2O_3 as the material for the dielectric spacer because it has negligible loss at the mid-infrared wavelengths up to 8 μm, and depositing thin Al_2O_3 layers with such thickness is a well-established process. Using Eq. (4), we design the dielectric thickness to be ~10 nm to create an optical topological transition in the mid-infrared range.

Section 5.3.2 Fabrication

The sample fabrication procedure is described as fellows. A CaF_2 wedge is used as the substrate, which is wedged by 2° to avoid backside reflection for the following ellipsometry characterization. The CVD graphene is grown on copper foil (Graphenea Inc.) and transferred to the substrate using the standard poly(methyl methacrylate) (PMMA) transfer technique [155,157]. The copper foil is etched using an ammonium persulfate solution. The size of the CVD graphene we transfer is about 10 mm by 10 mm. After transferring each graphene layer, we dope the graphene chemically by soaking the sample in a 0.25 mM solution of Tris(4-bromophenyl)ammoniumyl hexachloroantimonate ("magic blue") in dichloromethane for 10 minutes, and then rinse the sample with dichloromethane [158,159]. A sub-monolayer p-dopant is left on the graphene surface (see supplymentary materials of Ref. 29). The Al_2O_3 dielectric layer is deposited by atomic layer deposition (ALD) at 150 ºC using Trimethylaluminium as the Al precursor and H_2O as the oxygen precursor. The number of cycles used in the ALD process is calibrated to grow ~10 nm of Al_2O_3 on graphene, with the thickness characterized by an ellipsometer (Woollam M-2000). The procedure is repeated to fabricate 5 periods of the graphene-Al_2O_3 unit cell. We have also confirmed that the chemical doping with Tris(4-bromophenyl)ammoniumyl hexachloroantimonate does not affect the Al_2O_3 layer and the substrate. We have found that although nitric acid can also p-dope graphene effectively [41,56], it is not a good dopant for making the multilayer structure because of the damage to the thin Al_2O_3 layer. We also characterize the graphene-dielectric multilayer structure with the Woollam M-2000 ellipsometer after depositing each Al_2O_3 layer and after

transferring each graphene layer (see APPENDIX E). With the acquired ellipsometry data, we extract an average Al_2O_3 thickness of 10.4 nm.

Section 5.4 Sample characterization

Section 5.4.1 Optical conductivity of monolayer graphene

Because graphene is the key building block of the metamaterial, it is important to have an accurate measurement on the optical conductivity of the actual monolayer CVD graphene used to fabricate the multilayer sample. Although the theoretical optical conductivity given by Eq. (5) provides a good guideline for designing the graphene HMM, real CVD graphene layers can have imperfections or extrinsic properties that are not taken into account by Eq. (5). We therefore need to characterize actual graphene samples and examine the scope of validity of Eq. (5). In Chapter 4, we have reported in detail an ellipsometry-based technique we developed to measure the optical conductivity of truly 2D materials [41]. In this technique, the analysis used in conventional ellipsometry is modified to handle the infinitely thin 2D material whose properties are fully described by the 2D optical conductivity. As described in Section 5.3, we dope graphene chemically with "magic blue" in order to obtain more desirable optical conductivity. To characterize the optical conductivity with our ellipsometry technique, we prepare a sample with chemically-doped monolayer CVD graphene on a wedged CaF_2 substrate. For comparison, a sample with unintentionally-doped CVD graphene is also prepared and characterized. Notice that even without chemical treatment, unintentionally-doped CVD graphene is p-doped due to adsorbed gas molecules and residual ammonium persulfate from the transfer process [160,161].

The measurement is performed with the same procedure described in Chapter 4. Two different ellipsometers to cover a broad spectral range: Woollam M-2000 and Woollam IR-VASE are used for the wavelengths from 230 nm to 1.64 μm and the wavelengths above 2 μm, respectively. The data are acquired at three angles of incidence: 47 º, 57 º, and 67 º. The spot sizes of M-2000 and IR-VASE are 3 mm by 5.5 mm and 8

mm by 20 mm respectively when the incident angle is 57º. We mask the samples with scattering paper tissues (Kimwipes) for the IR-VASE measurement because the spot size is larger than the graphene area. Figure 5.6(a) shows the optical conductivities of both samples measured with our ellipsometry technique. The optical conductivities shown here are mathematically parameterized by cubic splines without assuming an *a priori* theoretical expression like Eq. (5). Consistent with Figure 5.5, in the mid-infrared range the chemically-doped graphene has a larger imaginary conductivity, which is necessary for creating the extreme anisotropicity in the metamaterial.

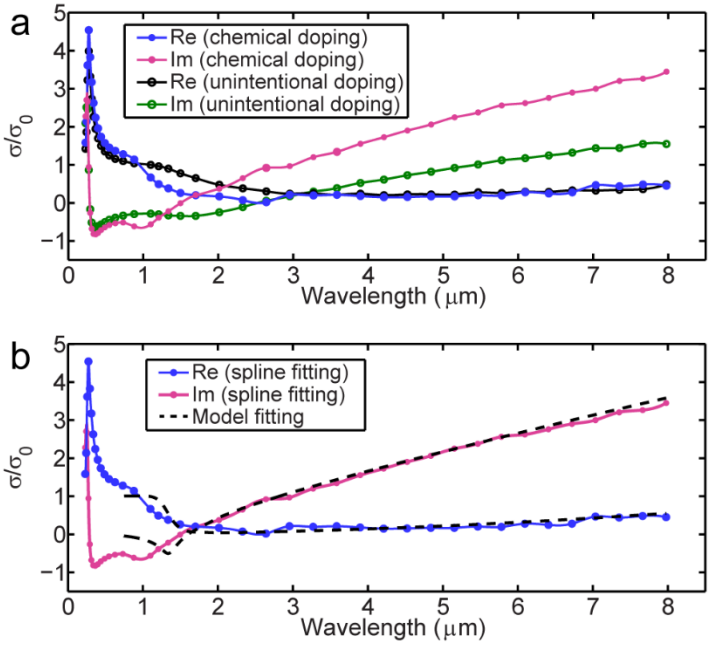

Figure 5.6 **The optical conductivity of CVD graphene measured by ellipsometry.** (a) The real and imaginary part of the optical conductivity of the chemically-doped CVD graphene (blue and magenta curves) and the unintentionally-doped CVD graphene (black and green curves). These curves are mathematically expressed by cubic splines, and the markers denote the control points of the splines. The chemically-doped CVD graphene has a larger imaginary conductivity in the mid-infrared range. (b**)** The real and imaginary part of the optical conductivity of the chemically-doped CVD graphene. The blue and magenta curves are obtained by fitting with cubic splines, and the black dash lines are obtained by using the model given by Eq. (5). The model fitting is consistent with the spline fitting in the mid infrared.

Although the spline-fitted conductivity of actual CVD graphene sample shown in Figure 5.6(a) is useful in many applications, a conductivity model based on a theoretical expression such as Eq. (5) provides more physical insight and requires fewer unknown parameters to perform the fit. The latter is important when we want to parameterize the homogenized metamaterial, which will be discussed in Section 5.4.2. Therefore, in Figure

5.6(b) we examine how well Eq. (5) works for the actual chemically-doped CVD graphene sample. We express the optical conductivity $\sigma(\omega)$ by the model of Eq. (5) with E_{F} and γ being the only two unknown fitting parameters. The optical conductivity extracted in this way is shown by the dash lines in Figure 5.6(b). We also show in the same figure the spline-fitted conductivity obtained from the same set of experimental data. It is apparent that the conductivity based on Eq. (5) overlaps very well with the spline-fitted conductivity throughout the mid-infrared range, assuring the validity of using Eq. (5) for the mid-infrared metamaterials. We extract from the fit that E_{F} = 460 meV and $\hbar\gamma$ = 23 meV. A mobility of ~2000 $\mathrm{cm^2V^{-1}s^{-1}}$ can be calculated from these numbers using the formula $\mu = e\pi\hbar V_{\mathrm{F}}^2/(\hbar\gamma\, E_{\mathrm{F}})$, which can be derived from the relation between the DC conductivity and the mobility. Here μ is the mobility and V_{F} is the Fermi velocity.

In the mid-infrared range, the optical conductivity is mostly determined by the intraband transitions, which are described by the Drude-like term in Eq. (5). Our result is consistent with Ref. 56, which shows that the Drude model can successfully fit the measured absorption spectrum of CVD graphene over a broad range of infrared wavelengths. We do not apply Eq. (5) to the ultraviolet and visible wavelength range because the many-body correction has been shown to be important there [26,27]. There is some discrepancy between the model and spline fits in the near infrared (around 1.5 microns, i.e. near the wavelength corresponding to the interband transitions close to the Fermi level). The origin of this discrepancy is not quantitatively understood, but may be related to spatial inhomogeneity in the Fermi energy (see Figure 4.5 of the previous chapter) or other disorder effects. Since the optical topological transition wavelength of our HMM is very far from this spectral region, and the fit is excellent over the entire mid-infrared, the failure of the simple model in the near-infrared region does not affect the behavior of the material in the mid-infrared, which is the region of concern in this work. Eq. (5) thus provides an excellent description for the mid-infrared conductivity.

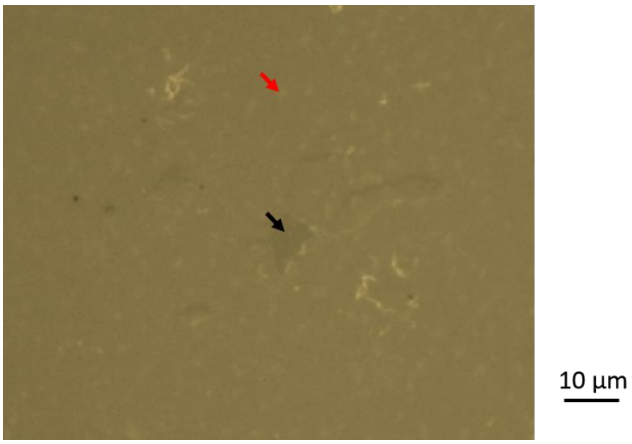

Figure 5.7 **Optical image of monolayer CVD graphene transferred on a CaF_2 substrate.** The red and black arrows indicate the multilayer patch and the crack, respectively.

Other imperfections that are typically present in transferred CVD graphene samples, such as the existence of small multilayer graphene patches and cracks, can also contribute to the deviations observed in Figure 5.6(b) [157]. In practice, CVD graphene obtained experimentally is not a perfectly continuous monolayer. Figure 5.7 shows an image of CVD graphene transferred to a CaF_2 substrate taken in an optical microscope. Although most of the area is monolayer graphene, there are inevitably some multilayer patches (indicated by the red arrow) and some cracks (indicated by the black arrow) [157]. Therefore, instead of being perfectly monolayer, a real sample of large-area CVD graphene is a combination of predominantly monolayer with some zero layer and multilayers.

Section 5.4.2 Effective permittivities of the graphene HMM

The numerical simulation in Section 5.2.2 has shown that the graphene-dielectric multilayer structure can be treated accurately as a metamaterial with the effective permittivities given by Eq. (3). In this section we use infrared ellipsometry to measure the effective permittivities of the fabricated graphene-dielectric multilayer sample. As discussed also in Section 5.2.2, ellipsometry is appropriate for measuring the effective permittivity of a metamaterial since it probes the sample with free-space plane waves, and the transverse wave vector ($k_0 \sin\theta$) associated with free-space plane waves is very small ($k_0 \sin\theta d \ll 1$, where θ is the angle of incidence). We are therefore probing the low-k modes of the metamaterial, ensuring the validity of the long-wavelength approximation.

The ellipsometer measurement is performed with the same condition described in Section 5.4.1. The raw data obtained by the infrared ellipsometry, the ellipsometric angles Ψ and Δ of the graphene-dielectric multilayer sample, are shown in Figure 5.8(a-b). The effective permittivities can be extracted by fitting the acquired data with appropriate analytical model. As discussed in Section 4.2, correct modeling of the sample is the key in ellipsometry, which requires prior knowledge about the sample. A minimal number of unknown parameters should be used to maintain the robustness of the fit. Since our simulation in Section 5.2.2 has demonstrated that the EMA is an accurate description for the multilayer structure, we can apply Eq. (3) in fitting the data. More precisely, we fit the experimental data to an analytical model that includes a layer of an anisotropic material on a CaF_2 substrate, with the permittivities of the anisotropic material given by Eq. (3). In Eq. (3), we know everything except the optical conductivity of graphene σ, as we have measured the thickness d independently after depositing each Al_2O_3 layer (see APPENDIX E), and we have measured the refractive index of the ALD-grown Al_2O_3 in the relevant spectral range independently with a separate sample with an Al_2O_3 film on a CaF_2 wedge. We can further parameterize the optical conductivity σ of graphene using Eq. (5). As shown by Figure 5.6(b), the expression of Eq. (5) is a good description for the optical conductivity of actual CVD graphene in the mid-infrared range. Therefore, we can apply Eq. (5) and parameterize the unknown optical conductivity with only E_F and γ. As a result of the independent knowledge of the sample, only two unknowns, E_F and γ, are sufficient to fit the experimental data of the multilayer metamaterial.

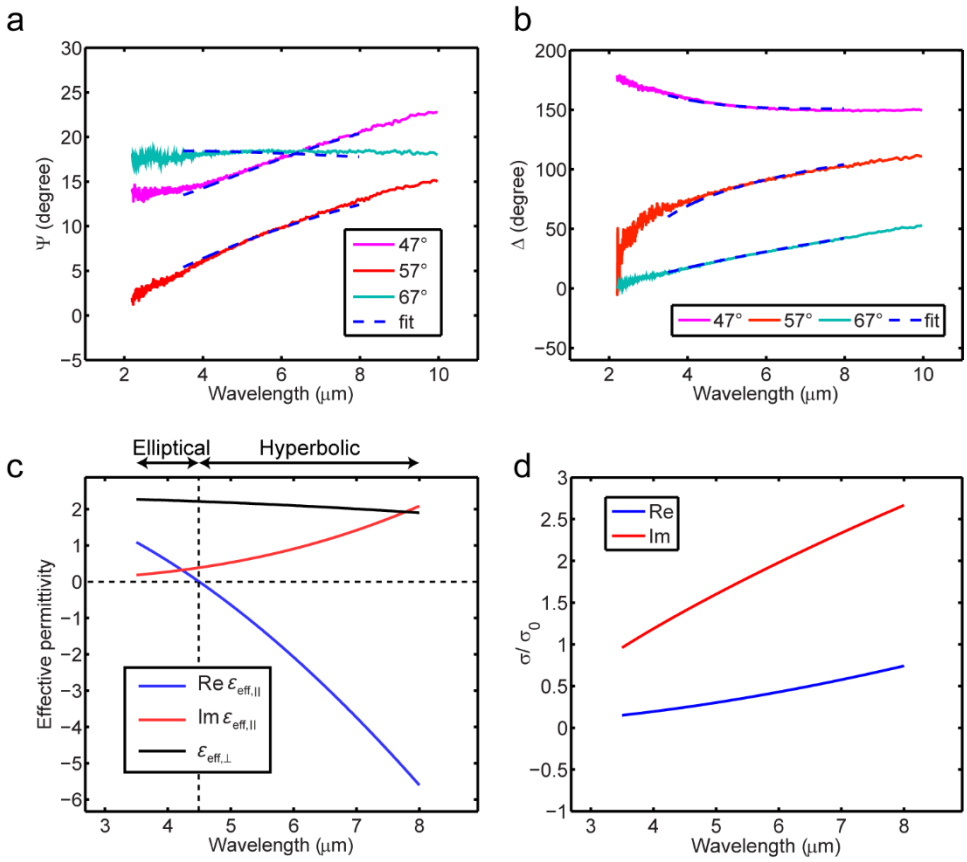

Figure 5.8 **Extraction of the effective permittivities of the graphene HMM, in which the graphene layers are chemically doped by magic blue.** (a) and (b) The ellipsometric angles Ψ and Δ acquired from the graphene-dielectric multilayer structure. The measurement is performed at incident angles of 47º, 57 º and 67 º. The blue dash lines show the fitting by homogenizing the multilayer structure into a metamaterial with the effective permittivities given by Eq. (3). (c) The extracted effective permittivities of the metamaterial, which exhibits an optical topological transition from elliptical to hyperbolic dispersion at 4.5 μm. (d) The extracted optical conductivity of the constituent CVD graphene in the metamaterial. The Al_2O_3 thickness in this sample is 10.4 nm, and there are 5 periods of the graphene-dielectric unit cell.

The fitted results of the ellipsometric angles Ψ and Δ are plotted as the blue dash lines in Figure 5.8(a) and (b), which match the experimental data very well. We restrict the fitting wavelengths range to 3.5 μm ~ 8 μm, where the lower bound is limited by the requirement of intraband-only response because of the application of Eq. (5), and the upper bound is due to the limited transparent spectral range of Al_2O_3. We emphasize that, we are able to reproduce all six Ψ and Δ curves acquired at different incident angles with only two free parameters in the fitting, which is a good indication that the model correctly reflects the essential physics. The extracted E_F is 365 meV, and the extracted $\hbar\gamma$ is 41 meV. The

extracted E_F is lower than the value we typically obtain from chemically-doped monolayer CVD graphene (as shown in Section 5.4.1), because some dopants are lost in the ALD process due to the vacuum environment and the elevated temperature. The obtained scattering rate $\hbar\gamma$ is higher than the value of graphene on CaF_2 substrate shown in Figure 5.6. This can be explained by the fact that the carrier scattering in graphene depends on the surrounding environment, from which we conclude that sandwiching graphene between Al_2O_3 increases the carrier scattering.

Figure 5.8(c) shows the effective permittivities of the graphene metamaterial given by the extracted values of E_F and γ, which is the main result of this work. As the figure indicates, $\varepsilon_{eff,\perp}$ is always positive because it equals the permittivity of Al_2O_3. On the other hand, the real part of $\varepsilon_{eff,\parallel}$ changes from a positive value to a negative value at 4.5 μm, indicating an optical topological transition from an elliptical metamaterial to a hyperbolic metamaterial. This graphene metamaterial is therefore a transverse epsilon-near-zero metamaterial at the wavelength of 4.5 μm [143]. The imaginary part of $\varepsilon_{eff,\parallel}$ is several times smaller than the real part in most of the spectral range with hyperbolic dispersion, indicating that the loss of this HMM is reasonably low. In Figure 5.8(d), we plot the optical conductivity of the constituent graphene sheet of the metamaterial using the extracted E_F and γ.

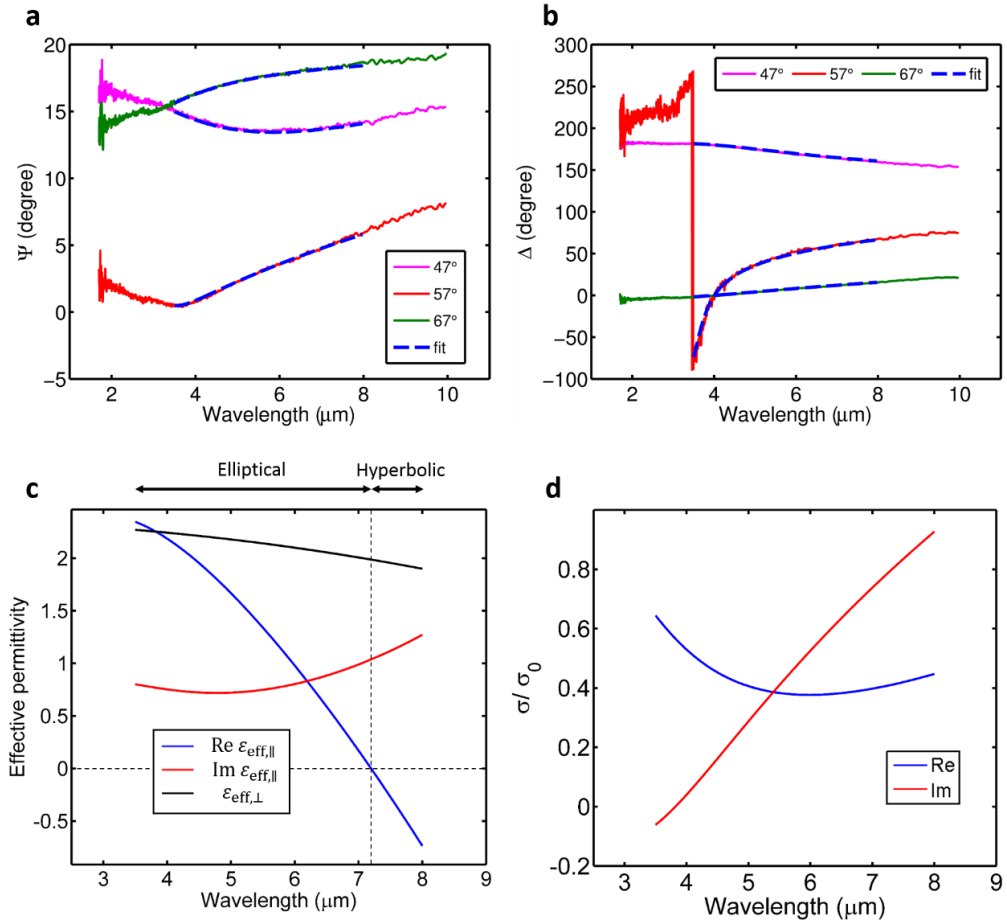

Figure 5.9 **Extraction of the effective permittivities of the graphene metamaterial, in which the CVD graphene is unintentionally doped.** (a) and (b) The ellipsometric angles Ψ and Δ acquired from the graphene-dielectric multilayer structure, respectively. The measurement is performed at incident angles of 47º, 57 º and 67 º. The blue dash lines show the fitting by homogenizing the multilayer structure into a metamaterial with the effective permittivities given by Eq. (3). (c) The extracted effective permittivities of the metamaterial, which exhibits a topological transition from elliptical to hyperbolic dispersion at 7.2 μm. (d) The extracted optical conductivity of the constituent CVD graphene in the metamaterial. The Al_2O_3 thickness in this sample is 10.3 nm, and there are 5 periods of the graphene-dielectric unit cell.

For comparison, we have also fabricated another graphene-dielectric multilayer sample with the same structure, except that the CVD graphene in this sample is not chemically doped. The unintentionally CVD graphene is still lightly p-doped due to the adsorbed gas molecules and residual ammonium persulfate. Figure 5.9(a) and (b) show the acquired ellipsometric angles Ψ and Δ of this sample. In fitting the data of this sample, we have found that we cannot obtain a satisfactory fit with the same procedure performed for Figure 5.8. This is because the optical conductivity of lightly-doped graphene is not purely contributed by the intraband response even at mid-infrared wavelengths, and therefore Eq. (5) cannot describe well an actual graphene sample when there is an inhomogeneity in the

Fermi energy. To account for the Fermi energy inhomogeneity, we assume the distribution in Fermi energy throughout the sample can be approximated by a Gaussian distribution, and fit the ellipsometric data with 3 free parameters: E_{FC}, s and γ, where E_{FC} and s are the center and standard deviation of the Gaussian distribution that describes the inhomogeneity of Fermi energy. With these 3 free parameters, we can obtain a satisfactory fit, as shown in Figure 5.9(a) and (b). The extracted values are E_{FC}=166 meV, s=47 meV and $\hbar\gamma$=44 meV. The extracted effective permittivities of this metamaterial and the optical conductivity of the constituent graphene are plotted in Figure 5.9(c) and (d).

As expected, the optical topological transition wavelength of this unintentionally-doped metamaterial sample is red-shifted compared to the chemically-doped sample, demonstrating the tunability of the metamaterial by doping. This sample is hyperbolic for wavelengths longer than 7.2 μm. However, as shown by Figure 5.9(c), the imaginary part of $\varepsilon_{\mathrm{eff},\parallel}$ is larger than its real part in the hyperbolic range. In terms of the material loss of a HMM, the unintentionally-doped sample is clearly not as good as the chemically-doped sample reported in Figure 5.8.

Section 5.5 Discussions

Our characterization by the infrared ellipsometry demonstrates that the graphene-dielectric multilayer structure indeed experiences an optical topological transition from an elliptical to a hyperbolic dispersion in the mid-infrared range, confirming the theoretical predictions of previous works [29,106,107,142-144,145-147] and representing the first experimental realization of graphene-based HMM. Our metamaterial sample has an optical topological transition at a wavelength of 4.5 μm and maintains good hyperbolic properties up to 8 μm. The upper bound of the wavelength range is limited by the absorption in Al_2O_3 and CVD graphene. While the absorption in the dielectric layer can be overcome by replacing Al_2O_3 with other infrared transparent materials such as ZnSe, the absorption in CVD graphene is limited by the quality of graphene. Recently, there have been reports of growth of large-area CVD graphene with a quality of single-crystal graphene [7] and new transfer process for CVD graphene without degrading the mobility [8]. With higher quality CVD graphene, the free-carrier absorption resulted from scattering could potentially be

suppressed. The transition wavelength, as determined by Eq. (4), can be shifted by choosing the dielectric thickness or controlling the doping of graphene. The latter has been demonstrated by our two samples shown in Figure 5.8 and Figure 5.9, which have the same structure but different doping levels. Shifting the transition wavelength farther into the infrared can be done by using lightly-doped graphene or thicker dielectric. On the other hand, blue shifting the transition wavelength is limited by the highest doping and the thinnest dielectric layers achievable in practice. While the structure reported in this work has only 5 periods, the procedure developed here can be repeated to scale up the graphene HMM. Some applications of HMMs do not require a large number of periods; for example, only a few periods is sufficient to produce a Purcell factor close to a semi-infinite structure, according to the theoretical calculations in Ref. 107.

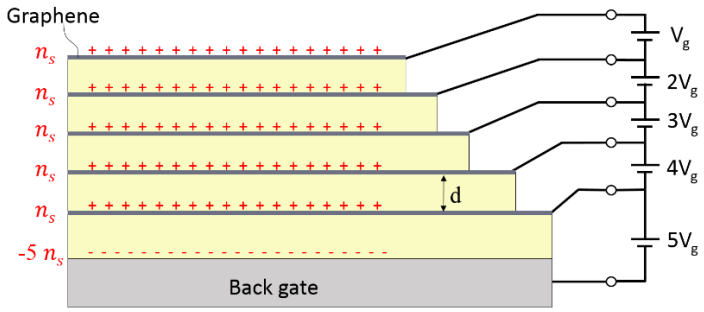

Figure 5.10 **A potential structure to electrically gate the graphene-based metamaterial.** Here n_s is the surface charge density. The voltage V_g equals $n_s d/\varepsilon$, where ε is the DC permittivity of the dielectric.

Graphene offers opportunities for realizaing active metamaterials because of the electrically tunability of its conductivity, as discussed in Section 1.4.1. In our current experimental realization, the doping of graphene is controlled by chemical doping. However, the graphene HMM would have a more significant impact if the control can be done by electrical gating. Electrical gating is commonly used in graphene-based field-effect transistors (FETs), in which the carrier concentration of one graphene layer is controlled by the gate voltage. A similar idea can potentially be applied to graphene-based metamaterials with multiple graphene layers, as shown in Figure 5.10. In order to gate the metamaterial such that the carrier concentration of all graphene layers change together, different voltages need to be applied to each graphene layer. Application of a single voltage to a top contact would result in an inhomogeneous density distribution due to interlayer

screening. It can be calculated from electrostatics that the voltage profile shown in Figure 5.10 can induce the same surface charge density n_s in all layers. Because the CVD graphene-based metamaterial studied in this work is fabricated by a layer-transfer method, each graphene layer could be accessed independently by patterning with photolithography. The challenge of realizing such electrically tunable graphene HMM is to obtain high quality dielectric layer that can withstand the applied voltage.

CHAPTER 6

Metasurface perfect absorber based on the guided resonance of a photonic hypercrystal

Section 6.1 Chapter introduction

Absorbers are of great interest to technologies of detectors, sensors, solar cells, stealth, optical modulators, and thermal emitters. Thanks to recent progress in metamaterials, metasurfaces, and plasmonics, many new concepts have been introduced into the design of absorbers [162-167]. Here we report a new type of perfect absorbers based on the guided resonance of a photonic hypercrystal (PHC) [168-171]. We show that a PHC slab is able to confine light to a deep subwavelength thickness, and therefore can be treated as a metasurface [11,12]. By incorporating the PHC slab with a dielectric spacer and a back reflector, a Salisbury screen absorber is formed [172]. We show that critical coupling can be obtained in this absorber, which realizes an absorption close to unity [30].

As discussed in Section 5.1.1, hyperbolic materials have attracted a lot of attention because of the various applications associated with the propagating high-k modes and the enhanced photonic density of states [124-126]. As most of the interesting behaviors of hyperbolic materials reside in the propagating high-k modes, however, there is a large k-vector mismatch between the propagating modes in the free space and in a hyperbolic material. This results in difficulties in accessing the high-k modes in hyperbolic materials with simple far-field optics. On the other hand, PHCs can bridge the k-vector mismatch and enable applications that are directly accessible from the far field. This can be performed

very efficiently via guided resonance [173-178]. A PHC is essentially a photonic crystal that includes a hyperbolic material as the constituent element [168]. It combines the unique material dispersion of a hyperbolic material with the band formation from the periodic structure. Because of the high-k modes supported in hyperbolic materials, the unit cell of the PHC can have deep subwavelength dimension and still form photonic band structure. Many interesting applications are enabled by PHCs, including creating Dirac dispersion [169], making better Veselago lenses [170], and enhancing the spontaneous emission from quantum dots [171].

Guided resonance, originating from the resonant coupling to the leaky guided modes, has been exploited extensively in photonic crystals and dielectric gratings [173-178]. Guided resonance provides a route to access efficiently the leaky confined modes from the free space. It has been applied to realize perfect absorbers [174], filters, and high reflectors [175]. It has also been used for engineering thermal emission [176] and improving light extraction from light-emitting diodes (LEDs) [177]. In this work, we extend the idea and exploit the guided resonance of a PHC slab. The use of PHC here is particularly attractive because hyperbolic materials are able to support high-k modes, and therefore light can be confined to a thickness much smaller than a wavelength. In fact, we will show that the thickness can be so small that the PHC slab can be treated as a metasurface. Similar deep subwavelength light confinement enabled by hyperbolic materials has been reported in the literature to create three-dimensional resonators with size as small as $\lambda/86$ [131,134].

In this work, we will show that the PHC slab serves as an angle-insensitive, 2D-like resonator, as the field is tightly confined in the thickness direction while more extended in the lateral direction. It can therefore be treated as a metasurface. The PHC slab is especially suitable for combining with graphene to enhance the otherwise weak light-graphene interaction. The combined system of a PHC slab and graphene creates an active metasurface that can be tuned by electrical gating [30,179]. In this work, we will show an example of such a combined system — a graphene-PHC optical modulator — in Section 6.5. The PHC can also be used for enhancing the absorption by graphene for graphene-based photodetectors.

Section 6.2 Guided resonance in a PHC slab

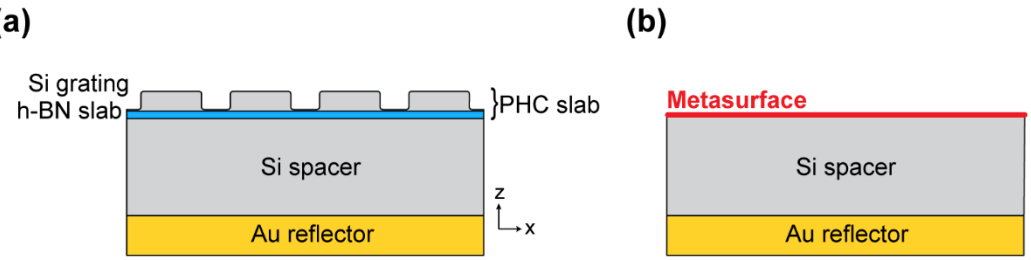

Figure 6.1 **The PHC-based perfect absorber and its equivalent Salisbury screen absorber.** (a) The schematic of the PHC-based perfect absorber. The thickness of the h-BN slab (light blue) is 50 nm. The Si grating (light grey) has a period of 590 nm and a duty cycle of 0.68. The heights of the dielectric grating is 130 nm (from the top of the grating to the Si/h-BN interface) and 10 nm (from the valley of the grating to the Si/h-BN interface). The thickness of the dielectric spacer (light grey) is 640 nm. The corners are rounded with a radius of 20 nm in the FEM simulation. (b) The equivalent Salisbury screen absorber, with the PHC slab treated as a metasurface.

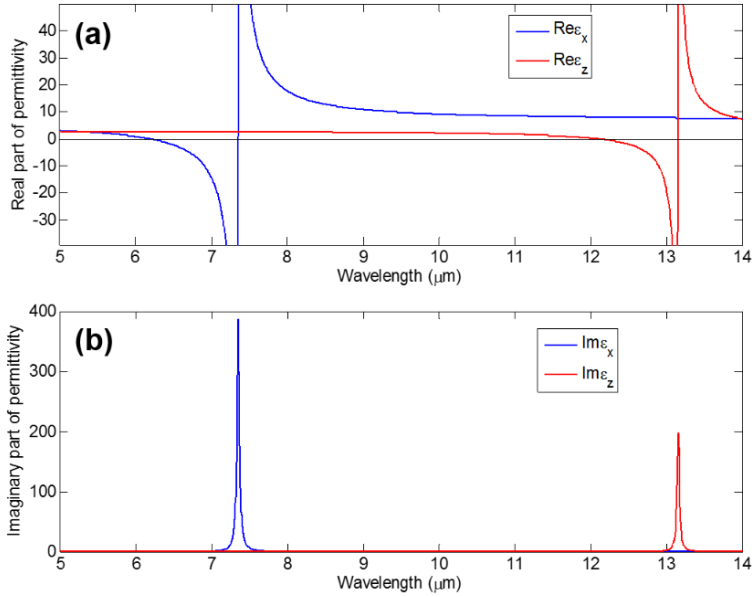

Figure 6.2 **The real (a) and imaginary (b) parts of the anisotropic permittivities of h-BN** measured by Dr. Joshua Caldwell at Naval Research Laboratory.

The geometry of the PHC-based perfect absorber is shown in Figure 6.1(a), which consists of a PHC slab, a dielectric spacer, and a metallic back reflector. The PHC slab is formed by a slab of a hyperbolic material and a subwavelength dielectric grating on top. The period of the dielectric grating is chosen to be much larger than the metamaterial limit but much smaller than the free-space wavelength [168]. In this example, we choose the dielectric to be amorphous silicon (refractive index =3.74, lossless [180]) for both the

grating and the spacer. We choose the hyperbolic material to be hexagonal boron nitrite (h-BN), whose permittivities are plotted in Figure 6.2. h-BN has a layered crystal structure similar to graphite, with the layers held together by the weak van der Waals force. As a results, it has very different in-plane and out-of-plane optical phonon frequencies, and becomes a natural type-I hyperbolic material at wavelengths between 12.1 and13.2 μm, and a type-II hyperbolic material between 6.2 and 7.4 μm [132,134,181,182]. The back reflector is made of Au. We design the PHC-based perfect absorber to operate at the wavelength near 12.6 μm. The period of the Si grating is 590 nm. The thicknesses of the h-BN slab and the spacer are 50 nm and 640 nm, respectively. Other detailed dimensions are listed in the caption of Figure 6.1(a).

The PHC-based absorber is simulated by the full-wave finite-element method (FEM) with a commercial package (COMSOL 5.1). The simulation is further confirmed with the rigorous coupled-wave analysis (RCWA) [183]. The simulated absorption spectrum for the TM polarization is plotted in Figure 6.3, which clearly shows a total absorption of 99.97 % at 12.62 μm, and almost all the absorption is achieved within the very thin h-BN slab (thickness ~ λ/252). Only a small percentage is absorbed by Au. For comparison, we also simulate the same structure but with the Si grating removed, which exhibits weak and featureless absorption. This reveals the important role played by the periodicity in a PHC.

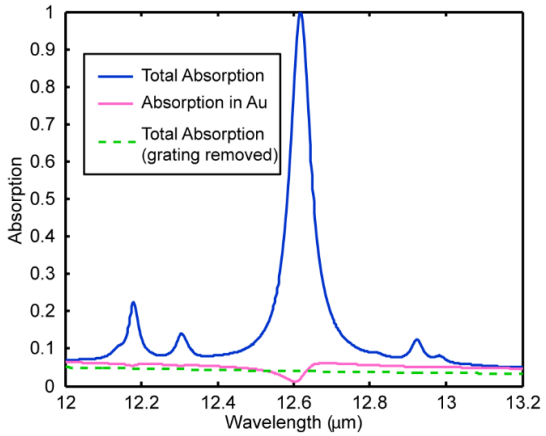

Figure 6.3 **Simulated absorption spectrum of the PHC-based perfect absorber plotted in Figure 6.1 (a).** The simulation is performed under TM polarization and normal incidence. The total absorption is 99.97% at the wavelength of 12.62 μm. h-BN and Au are the only lossy materials in the simulation, and almost all the absorption is achieved by the very thin h-BN slab. For comparison, we also simulate the same structure but with the Si grating removed (green dash line).

The physical origin of the strong absorption can be attributed to the guided resonance of the PHC slab formed by the h-BN slab and the Si grating. Each peak in the absorption spectrum shown in Figure 6.3 is associated with a specific waveguide mode of the h-BN slab, and the presence of the grating perturbs the waveguide mode and turns it into a leaky guided mode. The dispersion relation $\beta(\omega)$ of the waveguide modes in a slab of a hyperbolic material in a symmetric cladding environment can be obtained by solving (see APPENDIX F and Ref. 184)

$$\frac{\alpha_2/k}{\varepsilon_2/\varepsilon_x} = \tan(kh/2), \qquad \text{(even modes)} \qquad (1)$$

$$\frac{\alpha_2/k}{\varepsilon_2/\varepsilon_x} = -\cot(kh/2), \qquad \text{(odd modes)} \qquad (2)$$

where $\alpha_2 = \sqrt{\beta^2 - \varepsilon_2(\omega/c)^2}$ and $k = \sqrt{\varepsilon_x(\omega/c)^2 - (\varepsilon_x/\varepsilon_z)\beta^2}$. ε_2 is the permittivity of amorphous Si. ε_x and ε_z are the permittivities of h-BN in x- and z-directions. h is the thickness of the h-BN slab. Notice that each mode has two branches, labeled as the backward and the forward branches [184]. The backward branch is tightly confined, and its group velocity and phase velocity have opposite signs, which is an important feature of a type-I hyperbolic waveguide [184].

The main peak of Figure 6.3 is designed for the backward branch of the TM_0 mode. This can be shown by the Figure 6.4. The analytic H_y, E_x and E_z fields of the counter-propagating TM_0 waveguide modes of the backward branch are plotted in panels (a-c). Panels (d-f) show the FEM simulation of the H_y, E_x and E_z fields of the PHC-based perfect absorber at resonance. By comparing Figure 6.4(d-f) with (a-c), it is clear that the guided resonance of the PHC slab originates from the TM_0 waveguide mode in the h-BN slab. Other absorption peaks in Figure 6.3(a) are associated with higher-order waveguide modes. Field enhancement (electric field enhances ~21 times compared to the incident field) and deep subwavelength confinement are observed inside the h-BN slab at resonance.

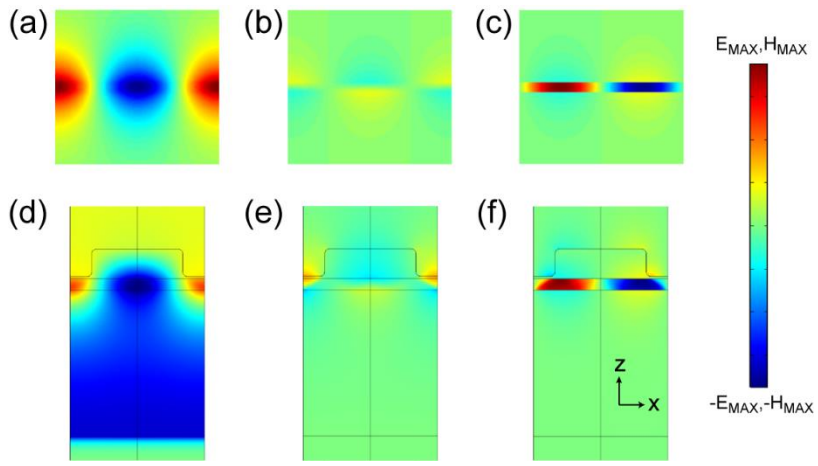

Figure 6.4 **Guided resonance of the PHC-based perfect absorber.** (a) H_y, (b) E_x and (c) E_z of the counter-propagating TM_0 waveguide modes (backward branch) in a waveguide of a 50nm-thick h-BN slab sandwiched by amorphous silicon at the wavelength of 12.62 μm. (d) H_y, (e) E_x and (f) E_z of the PHC-based perfect absorber simulated using FEM at the wavelength of 12.62 μm. E_x and E_z are plotted with a quarter cycle time difference relative to H_y.

It is worthy emphasizing that the period of the PHC is deep subwavelength (~ λ/21), in marked contrast to other guided-resonance structures, which often have periods on the order of the wavelength. This is a unique feature of PHC [168], which can be traced back to the high-k modes supported by the hyperbolic material. It enables the angle-insensitive performance and the metasurface homogenization that will be discussed later. The resonant frequency of the PHC-based absorber can be controlled with the period of the subwavelength grating or the thickness of the h-BN slab. Figure 6.5(a) shows the absorption spectra of the PHC-based absorbers with different grating periods, demonstrating the tuning of the resonant frequency. Furthermore, we show in Figure 6.5(b) the absorption of the PHC-based absorber as a function of the angle of incidence. The absorption spectra with different angles of incidence are also plotted in Figure 6.9(b). Interestingly, the response of the PHC-based absorber is insensitive to the angle of incidence, which is advantageous for wide-angle applications. This is a surprising feature, as guide-resonance structures are usually angle-sensitive due to the requirement of in-plane momentum match [162]. In our case, however, because the hyperbolic waveguide mode has extremely high k-vectors, the requirement of in-plane momentum match is achieved almost entirely by the deep subwavelength periodicity of the grating, while the k-vector of the incident wave (which depends on angle) plays little role.

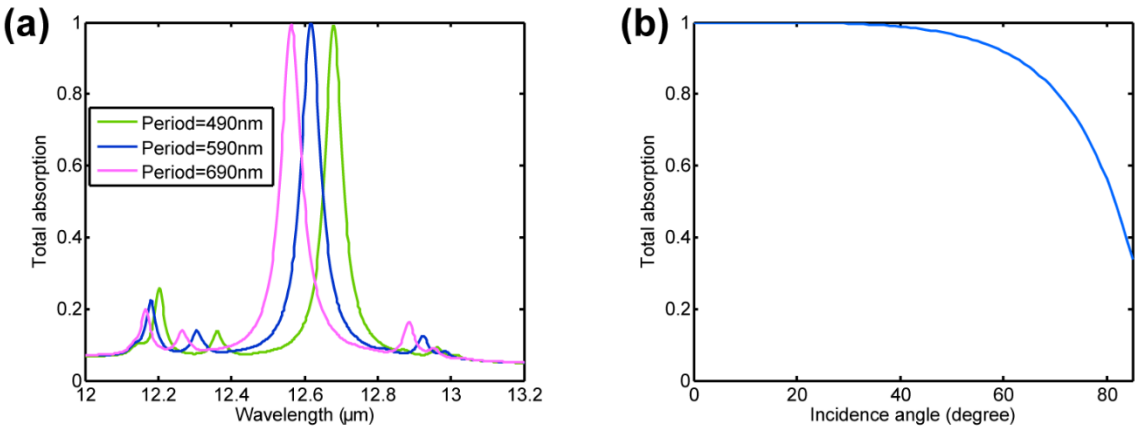

Figure 6.5 **Period and angular dependence of the PHC-based perfect absorber.** (a) Shift of the resonant frequency by varying the period of the subwavelength grating. All other dimensions are kept the same as Figure 6.1 (a). (b) Angular dependence of the total absorption of the PHC-based absorber. Wavelength is fixed at 12.62 μm in evaluating the absorption.

Section 6.3 Extract the metasurface parameters of a resonant PHC slab

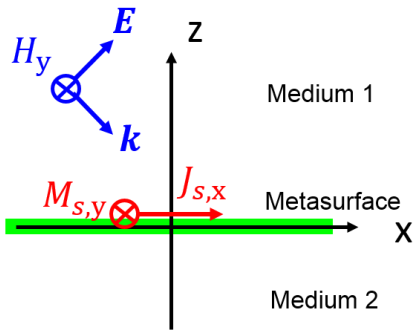

Figure 6.6 **A schematic representation of a metasurface excited with a TM incident wave.**

In this section, I will show that the PHC slab, formed by the Si grating and the h-BN slab, can be homogenized and treated as a metasurface. This is because the PHC slab has deep subwavelength thickness ($\sim \lambda/252$) and period ($\sim \lambda/21$). Such a treatment provides intuitive understanding of the operating principle of the PHC-based absorber and enables straightforward design. Here I apply the method in Ref. 185 to extract the effective parameters of the metasurface from the simulation of the complex reflection and transmission coefficients of the PHC slab. As plotted in Figure 6.6, we consider a metasurface sandwiched between medium 1 and medium 2. This metasurface is treated as an infinitely thin layer that exhibits interesting interaction with light. From the symmetry

argument (the structure has mirror symmetry with respect to xz plane), the response of the structure can be separated into TM and TE modes and discussed independently [186]. Here we consider only the TM mode because h-BN exhibits hyperbolic dispersion only in this polarization. A metasurface can support effective electric and magnetic surface currents, $J_{\mathrm{s,x}}$ and $M_{\mathrm{s,y}}$, which are given by

$$\begin{pmatrix} J_{\mathrm{s,x}} \\ M_{\mathrm{s,y}} \end{pmatrix} = \begin{pmatrix} \sigma_{\mathrm{e}} & \chi \\ \chi' & Z_{\mathrm{m}} \end{pmatrix} \begin{pmatrix} E_{\mathrm{x}} \\ H_{\mathrm{y}} \end{pmatrix}, \tag{3}$$

where σ_{e} and Z_{m} are the electric sheet conductivity and magnetic sheet impedance, respectively. χ and χ' are the magnetoelectric coupling terms. These four effective parameters (σ_{e}, Z_{m}, χ, and χ') describe the properties of the metasurface. To extract these parameters from simulation, we can use the boundary conditions at $z = 0$:

$$\begin{cases} -H_y^{(1)} + H_y^{(2)} = J_{\mathrm{s,x}} = \sigma_{\mathrm{e}} E_x^{(\mathrm{av})} + \chi H_y^{(\mathrm{av})} \\ -E_x^{(1)} + E_x^{(2)} = M_{\mathrm{s,y}} = \chi' E_x^{(\mathrm{av})} + Z_{\mathrm{m}} H_y^{(\mathrm{av})} \end{cases}, \tag{4}$$

where $E_x^{(\mathrm{av})} = \frac{1}{2}\left(E_x^{(1)} + E_x^{(2)}\right)$, $H_y^{(\mathrm{av})} = \frac{1}{2}\left(H_y^{(1)} + H_y^{(2)}\right)$. The superscripts of (1) and (2) denote the medium in which the field is evaluated. At normal incidence, Eq. (4) can be formulated into an expression that connects σ_{e}, Z_{m}, χ,and χ' to the S-parameters [185].

$$\begin{pmatrix} \sigma_{\mathrm{e}} Z_0 \\ \chi \\ Z_{\mathrm{m}}/Z_0 \\ \chi' \end{pmatrix}$$

$$= 2 \begin{pmatrix} \frac{(-1+S_{11})}{n_1} - \frac{S_{21}}{n_2} & 1 + S_{11} + S_{21} & 0 & 0 \\ \frac{S_{12}}{n_1} + \frac{(1-S_{22})}{n_2} & 1 + S_{12} + S_{22} & 0 & 0 \\ 0 & 0 & 1 + S_{11} + S_{21} & \frac{(-1+S_{11})}{n_1} - \frac{S_{21}}{n_2} \\ 0 & 0 & 1 + S_{12} + S_{22} & \frac{S_{12}}{n_1} + \frac{(1-S_{22})}{n_2} \end{pmatrix}^{-1}$$

$$\times \begin{pmatrix} -1 - S_{11} + S_{21} \\ 1 - S_{12} + S_{22} \\ (1-S_{11})/n_1 - S_{21}/n_2 \\ -S_{12}/n_1 + (1-S_{22})/n_2 \end{pmatrix}. \tag{5}$$

The S-parameters are related to the Fresnel reflection and transmission coefficients by

$$\begin{aligned} S_{11} &= -r_{12} \\ S_{22} &= -r_{21} \\ S_{12} &= (n_1/n_2)t_{21} \\ S_{21} &= (n_2/n_1)t_{12}\,. \end{aligned} \tag{6}$$

Here are a few comments about the convention I use. In the convention of S-parameter S_{ij}, i and j label the receiving and exciting sides, respectively. On the other hand, another convention applies to r_{ij} and t_{ij}, which represent the reflection and transmission coefficients for waves sending from medium i to medium j. The sign of r_{ij} is defined for the electric fields. Temporal dependence in the form of $e^{-i\omega t}$ is assumed.

Full-wave FEM electromagnetic simulation is performed to obtain the reflection and transmission coefficients of the PHC slab (the simulation is performed without the back reflector). Using Eq. (5), we can treat the PHC slab as a metasurface and extract the effective parameters. The extracted σ_{e}, Z_{m}, χ, and χ' are plotted in Figure 6.7. We note that $\chi = -\chi'$, which is a consequence of reciprocity. More importantly, it can been seen that the response of the metasurface is dominated by the electric sheet conductivity, since Z_{m}/Z_0, χ and χ' are all negligible compared to $\sigma_{\mathrm{e}}Z_0$, where Z_0 is the vacuum impedance. Therefore, the PHC slab is effectively an infinitely thin sheet with an electric sheet conductivity σ_{e}. We will show in the next section that this gives a quantitatively accurate description for the PHC slab.

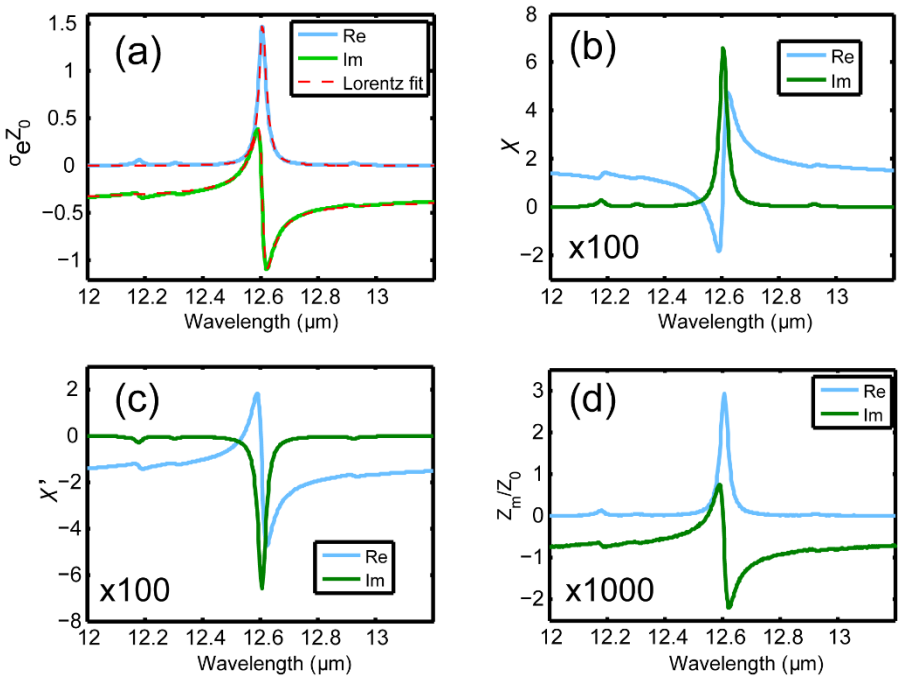

Figure 6.7 **Parameters for the equivalent metasurface of the PHC slab.** (a) σ_e (b) χ (c) χ'(d) Z_m. Notice that (b) and (c) are scaled by 100 times, and (d) is scaled by 1000 times for clarity. We also perform a Lorenz fit to (a).

The metasurface exhibits the resonant behavior of a Lorentz oscillator, which is shown by Figure 6.7(a). We fit the electric sheet conductivity σ_e to this expression:

$$\sigma_e(\omega) = \frac{\sigma_M}{-i(\omega-\omega_0)+\gamma} + ip\ , \tag{7}$$

where ip is added to account for the constant phase shift due to an effective thickness. Eq. (7) produces a very good fit, from which we extract a quality factor $Q = \omega_0/(2\,\gamma)$=399. This value is very close to $\omega(\frac{d\varepsilon_z'}{d\omega})/(2\varepsilon_z'')$=390 for h-BN, where ε_z' and ε_z'' are the real and imaginary part of the permittivity of h-BN in z-direction; this is an estimated quality factor obtained simply by assuming the electric field is only in z-direction, entirely inside h-BN, and damped only by the material loss [187].

Section 6.4 Critical coupling of the metasurface perfect absorber

Because the PHC slab is effectively a metasurface, the absorber can be viewed as a Salisbury screen, as plotted in Figure 6.1(b), and the resonant metasurface provides the required electric sheet conductivity σ_{e} for critical coupling. As mentioned in the last section, we treat the PHC slab as a metasurface with the electric sheet conductivity σ_{e} only, since the contributions from magnetic sheet impedance Z_{m} and magnetoelectric coupling terms χ and χ' are negligible. Therefore, interestingly enough, the PHC slab is treated mathematically the same way we did in Chapter 4 and 5 for graphene. The critical coupling condition for the effective Salisbury screen can be derived as follows [30]. The reflection coefficient of the Salisbury screen is given by

$$r = \frac{r_{12}+(1+r_{12}+r_{21})r_{23}e^{i2k_{2z}d}}{1-r_{21}r_{23}e^{i2k_{2z}d}}, \tag{8}$$

where r_{23} is the Fresnel reflection coefficient of the Si/Au interface. k_{2z} is the z component of wave vector in Si. d is the spacer thickness. The critical coupling condition is satisfied when the numerator of Eq. (8) equals zero, i.e.

$$r_{12} + (1 + r_{12} + r_{21})r_{23}e^{i2k_{2z}d} = 0\ . \tag{9}$$

At normal incidence, we can write down simple analytical expressions for r_{12} and r_{21} using the modified Fresnel equations for an interface with a sheet electric conductivity σ_{e} sandwiched between two media: (see APPENDIX B and Ref. 30).

$$\begin{aligned} r_{12} &= (n_1 - n_2 - \sigma_{\mathrm{e}}Z_0)/(n_1 + n_2 + \sigma_{\mathrm{e}}Z_0) \\ r_{21} &= (n_2 - n_1 - \sigma_{\mathrm{e}}Z_0)/(n_1 + n_2 + \sigma_{\mathrm{e}}Z_0)\ , \end{aligned} \tag{10}$$

where n_1 and n_2 are the refractive indexes for air and Si, respectively. By inserting Eq. (10) into Eq. (9), we can obtain the value of σ_{e} required for critical coupling.

$$\sigma_{\mathrm{e}}Z_0 = n_1 - n_2\frac{1-r_{23}e^{i2k_{2z}d}}{1+r_{23}e^{i2k_{2z}d}} \tag{11}$$

Therefore, if we can design a metasurface to provide this electric sheet conductivity, we can achieve perfect absorption. This condition can be used to guide the design of the

appropriate PHC slab. We plot Eq. (11) as a function of the spacer thickness d, as shown in Figure 6.8. Since we cannot obtain arbitrary values for the real and imaginary parts of σ_e with the PHC slab, Figure 6.8 suggests that the most practical design for critical coupling is to choose a thickness d not too far from $\lambda/(4n_2) = 844$nm. With this choice, it is easier to design the PHC slab since the required Im σ_e is not too extreme. On the other hand, the required Re σ_e is essentially independent of d, according to Figure 6.8. Furthermore, because the required Im σ_e can be tuned by changing the spacer thickness d, as long as we can design a metasurface with sufficient Lorentz oscillator strength, we also always find a spacer thickness d to achieve critical coupling.

In Figure 6.8 we also mark the σ_e value required for critical coupling when d=640nm, which is the spacer thickness used in our design of the PHC-based perfect absorber (see the caption of Figure 6.1). In the inset, we mark the σ_e provided by the PHC slab, as extracted in Section 6.3. We can see that the PHC slab indeed provides appropriate electric sheet conductivity for critical coupling.

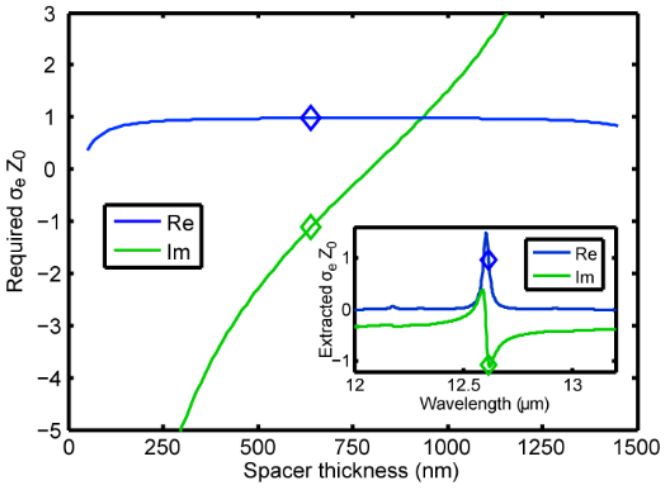

Figure 6.8 **The electric sheet conductivity σ_e required to achieve critical coupling as a function of the spacer thickness.** It is plotted for $n_1 = 1$ (air), $n_2 = 3.74$ (amorphous Si) and $n_3 = 11.91 + 89.21$ i (Au) at a wavelength of 12.62 μm. The markers indicate the σ_e value at the spacer thickness of 640 nm, the thickness used in our design shown by Figure 6.1(a). The inset shows the effective electric sheet conductivity σ_e provided by the PHC slab (same as Figure 6.7 a), with the σ_e value at the operating wavelength (12.62 μm) of our PHC-based absorber indicated by markers.

We can further verify that that the equivalent Salisbury screen reproduces accurately the behaviors of the PHC-based absorber. In Figure 6.9(a) we use two different methods to calculate the absorption spectra of the PHC-based absorber for different spacer

thicknesses. The solid lines in this figure are obtained with the full-wave FEM simulation of the detailed geometry plotted in Figure 6.1(a). In the same figure, the cross markers are obtained by homogenizing the PHC slab into a metasurface and treating the absorber as a metasurface Salisbury screen, as shown by Figure 6.1(b). For the Salisbury screen, the absorption is calculated semi-analytically using Eq. (8) and Eq. (10) together with the extracted electric sheet conductivity σ_e plotted in Figure 6.7(a). It can be seen that the semi-analytical calculation of the Salisbury screen reproduces excellently the full-wave simulation of the detailed geometry. Notice that in Figure 6.9(a) the critical coupling condition is satisfied when d =640 nm and λ = 12.62μm, as well as when d =840 nm and λ = 12.595 μm.

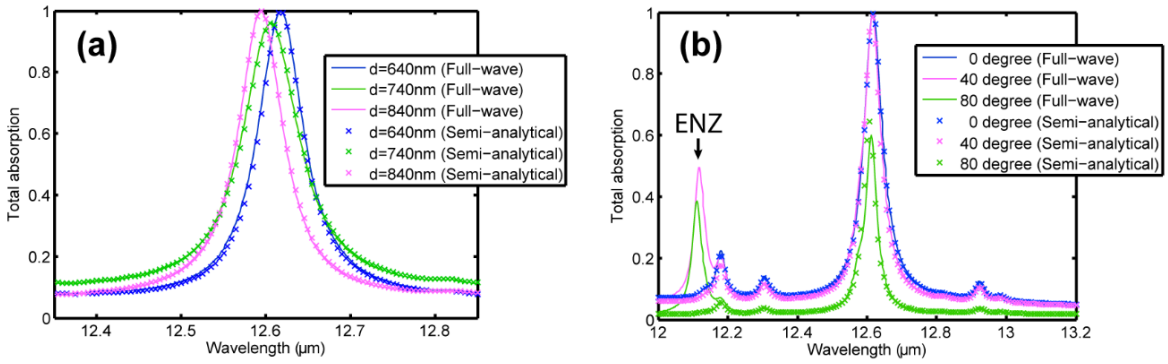

Figure 6.9 **(a) The absorption spectra of the PHC-based absorber with different spacer thicknesses. (b) The absorption spectra of the PHC-based absorber at different incidence angles.** The results obtained from both full-wave FEM simulation (geometry shown by Figure 6.1a) and semi-analytical calculation (with PHC homogenized as a metasurface, as shown in Figure 6.1b) are plotted for comparison.

Another verification for the equivalent metasurface Salisbury screen is given by Figure 6.9(b). Recall that in Section 6.3 the effective surface conductivity σ_e is extracted from the simulation performed at normal incidence. Therefore, we still need to check if the σ_e extracted at normal incidence also works for oblique incident angles. We plot in Figure 6.9(b) the angular dependence of the absorption spectra, obtained by both the full-wave simulation of detailed geometry and the semi-analytical calculation of the equivalent Salisbury screen. It shows that the semi-analytical calculation reproduces the full-wave simulation very well, except that there is a slight deviation at very large angle, and the semi-analytical calculation also misses the peak occurring at the wavelength of 12.1 μm for oblique angles. At this wavelength, h-BN becomes an epsilon-near-zero (ENZ)

material, which can offer field enhancement to the z-component of the electric field [188]. The effective metasurface cannot capture this feature because of the lack of out-of-plane response. Nevertheless, this peak associated with ENZ is not relevant to the behaviors of the PHC since h-BN is no longer a hyperbolic material at this wavelength.

To conclude this section, our analysis verifies our understanding of the mechanism of the PHC-based perfect absorber: It is a Salisbury screen in which the PHC slab works as a metasurface to provide the appropriate surface conductivity for critical coupling. This understanding is quantitatively accurate, and can be used as a guidance for designing the PHC-based perfect absorber

Section 6.5 Applications

Section 6.5.1 Graphene-PHC optical modulator

The PHC-based perfect absorber can combine with an electrically tunable material such as graphene to make optical modulators, as plotted in Figure 6.10(a). The dimensions of the device structure of Figure 6.10(a) are the same as those in Figure 6.1(a) except that the spacer thickness is changed to 710 nm, since the presence of graphene changes the critical coupling condition. To gate graphene, the silicon spacer can be slightly doped to be part of the gate electrode [31], and the h-BN slab serves as the gate dielectric [189]. Doping can introduce some free-carrier absorption in the spacer; however, the doping concentration can be very low because we only need to gate one atomic layer of graphene. Alternatively, we can use intrinsic silicon as the spacer, which becomes part of the gate dielectric. Such a design would decrease the capacitance and therefore require a larger applied voltage. It is also possible to use two graphene layers to sandwich the h-BN slab; in this case the two graphene layers serve as the gate electrodes and the h-BN slab as the gate dielectric [32]. Here we present only the simulation results of the device structure plotted in Figure 6.10(a), which has one graphene layer.

By incorporating the PHC slab with graphene, the effective metasurface becomes dynamically tunable. Because of the atomic thickness, graphene itself does not have enough interaction with light to modulate light effectively, and therefore graphene-based

modulators usually need to incorporate resonant structures such metallic metasurfaces [30], micro rings [32], or to pattern graphene into a plasmonic structure [33]. Similarly, our PHC slab serves as a resonant structure to enhance the otherwise weak light-graphene interaction. It should be noted that by nature the PHC slab can work together with graphene very well, because the electric field is tightly confined into a deep subwavelength thickness. It forms a very thin, almost 2D-like cavity that can interact efficiently with 2D materials. This device structure offers several advantages for optical modulation. One important advantage is that we can design for critical coupling, which minimizes the reflection when the modulator is in the OFF state and enables good modulation depth [30,33]. Another advantage is the high operation speed, as the high mobility of graphene has enabled modulators operating up to 30 GHz [30,32]. Also, in our case h-BN is particularly a good match for graphene, since they share very similar lattices such that h-BN can help maintain the good mobility of graphene [190]. Such a graphene-h-BN combined system has been studied in the literature [182,191].

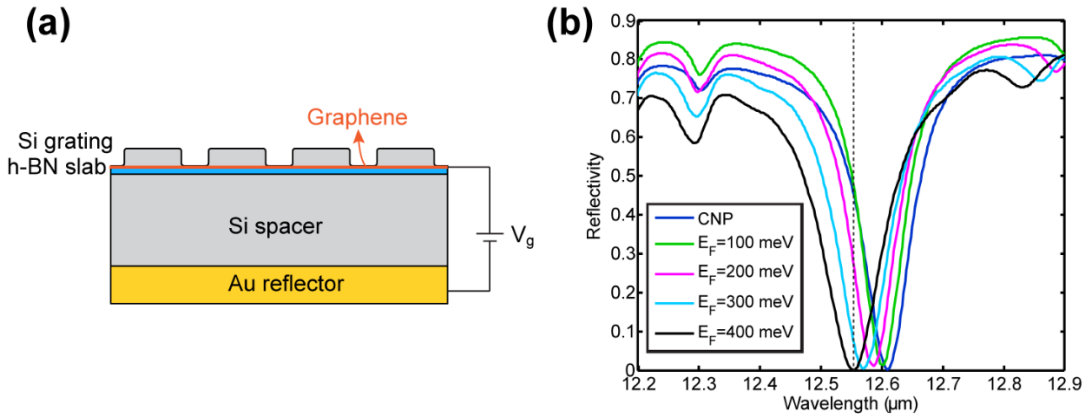

Figure 6.10 **The graphene-PHC optical modulator.** (a) The device structure of the graphene-PHC optical modulator. (b) The reflection spectra of the optical modulator when graphene is gated to different Fermi energies. The dash line marks the operating wavelength at 12.55 μm. E_F=100 meV and 400 meV correspond to the ON and OFF state of the optical modulator, respectively.

Figure 6.10(b) shows the reflection spectra of the graphene-PHC optical modulator when graphene is gated to different Fermi energies. To model graphene in the FEM simulation, we assign a surface current at the boundary, with the amplitude proportional to the in-plane electric field. The highest Fermi energy simulated is 400 meV, which is a value often achieved experimentally with electrical gating. The optical conductivity of graphene is simply taken as the universal conductivity $\sigma_0 = e^2/(4\hbar)$ when graphene is gated to the

charge neutrality point (CNP). For other Fermi energies, the simulation is done with the optical conductivity of graphene given by the theoretical expression (see Section 1.3) [21-23]

$$\sigma(\omega) = \frac{\sigma_0}{2}\left(\tanh\frac{\hbar\omega+2E_\mathrm{F}}{4k_\mathrm{B}T} + \tanh\frac{\hbar\omega-2E_\mathrm{F}}{4k_\mathrm{B}T}\right) - i\frac{\sigma_0}{2\pi}\log\left[\frac{(\hbar\omega+2E_\mathrm{F})^2}{(\hbar\omega-2E_\mathrm{F})^2+(2k_\mathrm{B}T)^2}\right] + i\frac{4\sigma_0}{\pi}\frac{E_\mathrm{F}}{\hbar\omega+i\hbar\gamma}, \quad (12)$$

where E_F is the Fermi energy relative to the Dirac point, and γ is the intraband scattering rate. We choose $\hbar\gamma$ to be 20 meV, which is a reasonable value for chemical-vapor-deposited (CVD) graphene [29]. Notice from Figure 6.10(b) that we have designed the modulator such that critical coupling is achieved when E_F=400 meV, and in this case light is almost perfectly absorbed (absorption=99.98 %) at the wavelength of 12.55 μm. This optical modulator is designed to operate at a center wavelength of 12.55 μm, and its ON state and OFF state correspond to E_F =100 meV and 400 meV, respectively. The modulation depth, defined by $(1 - R_\mathrm{OFF}/R_\mathrm{ON})$, can achieve 99.96 %, where R_OFF and R_ON are the reflectivities of the OFF and ON state. This good modulation depth is made possible by the critical coupling design that minimizes R_OFF. Another figure of merit for optical modulators is the insertion loss, which is defined by $-10\log(R_\mathrm{ON})$ in the unit of dB. Our graphene-PHC optical modulator exhibits an insert loss of 3.2 dB.

Section 6.5.2 Absorption enhancement for graphene-based photodetection

The same device structure shown in Figure 6.10(a) can also be used to enhance the absorption in graphene, which can apply to graphene-based photodetectors and sensors to improve the responsivity. Since the field is confined and enhanced within a deep subwavelength thickness, the PHC slab forms an ultra-thin, 2D-like cavity that enhances the absorption in graphene. This is especially useful for those detection mechanisms that rely on absorption over the whole area (in contrast to the mechanisms relying on junctions), such as bolometric and photogating effects (see Section 1.4.2) [45,48]. In particular, we can also combine this PHC-based absorber with our double-layer graphene photodetector reported in Chapter 3. This can be done by replacing the single layer graphene in Figure

6.10(a) with a double-layer graphene heterostructure (two graphene layers sandwiching a tunneling barrier) [48]. In this case we can further increase the responsivity by utilizing phototransistor gain together with an enhanced absorption.

The absorption enhancement is shown in Figure 6.11, where we plot the absorption by the graphene for the same device shown by Figure 6.10(a). It can be seen that, at the CNP, the monolayer graphene can absorb up to 39 % of the light, which is ~ 17 times enhancement compared to the 2.3% absorption for suspended graphene.

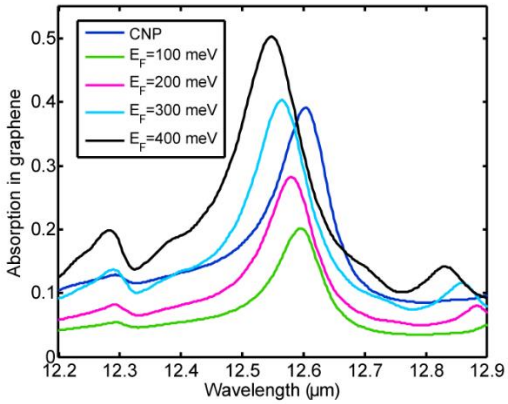

Figure 6.11 **The absorption by the graphene layer for the device plotted in Figure 6.10(a).**

Section 6.6 Discussions

It is worth emphasizing that the PHC slab forms a special resonator with 2D-like nature. The field is tightly confined in the thickness direction (thickness=50 nm) while more extended in the lateral direction (period=590 nm). This is different from resonators based on localized surface plasmons, which are tightly confined in three dimensions, and also different from photonic crystal resonators, which do not have deep subwavelength confinement. We have also shown the angle insensitivity of the PHC, which is dramatically different from many resonators associated with extended modes [162]. As a result of this 2D-like natre, the PHC is particularly suitable for incorporating with graphene to make optical modulators and better detectors, as discussed in Section 6.5.

Regarding the restrictions of the current design of the PHC-based perfect absorber, because h-BN is used as the hyperbolic material in this work, the operating spectral range is limited to the small spectral window where h-BN exhibits the hyperbolic dispersion.

However, there are many other natural hyperbolic materials that cover entire spectrum from ultraviolet to far infrared [132]. Furthermore, the required hyperbolic dispersion can also be obtained with hyperbolic metamaterials (HMMs), which can be engineered for the desired spectral range [124-127]. In particular, the graphene HMM described in Chapter 5 can also be used here for mid-infrared operation [41]. Another restriction of the current design is the polarization. It works only for TM polarization due to the use of the one-dimensional grating structure. The current design can potentially be extended to make polarization-independent perfect absorbers by using 2D periodic structures such as disc or hole arrays.

CHAPTER 7

Conclusion

Section 7.1 Summary

In this thesis, I have addressed several key frontiers of graphene research specifically for applications in optoelectronics and metamaterials. The first frontier, regarding the understanding of fundamental optical properties of graphene, is investigated in Chapter 2 and Chapter 4. In Chapter 2, I have conducted experimental studies on the nonlinear harmonic generation in graphene at THz frequencies. The fact that we observe no detectable THz harmonic generation reveals the fundamental role played by strong carrier-carrier scattering, which had been neglected by published theories of nonlinearity. In Chapter 4, I have developed an ellipsometry-based technique that allows for the reliable measurement of the optical conductivity of graphene and other 2D materials. This technique can have wide applications for the 2D material community; therefore I have worked with collaborators at Purdue University to develop a free software based on this technique. It is called Photonicvasefit, which is now available on nanohub.org and has been used by users around the world.

Chapter 3 and Chapter 4 address the second frontier — the new opportunities in physics and applications enabled by fabricating complex graphene layered structures. In Chapter 3, we have developed a novel double-layer graphene photodetector, in which two graphene layers are separated by a tunneling barrier to allow photogating of the graphene channel. With the help of phototransistor gain, this photodetector is broadband and has a responsivity several orders higher than conventional graphene detectors. In Chapter 5, I

have fabricated a graphene-dielectric multilayer structure and shown with ellipsometry that the structure forms a metamaterial with hyperbolic dispersion in the mid-infrared range. This represents the first experimental realization of a graphene-based hyperbolic metamaterial.

The third frontier — the opportunity arising from combining graphene with a metasurface — is addressed in Chapter 6. A novel metasurface realized with a photonic hypercrystal slab is proposed. I have shown by numerical simulation that this metasurface can be used to form a Salisbury screen perfect absorber. By combining this metasurface with graphene, the guided resonance in the photonic hypercrystal can enhance the otherwise weak light-graphene interaction. I have shown examples of optical modulators and better photodetectors that are enabled by such a combination.

Section 7.2 Future directions

I have demonstrated that graphene is a promising building block for optoelectronics and metamaterials with many examples in the thesis. One of the most useful properties of graphene is the fact that the optical conductivity is highly tunable by electrical gating, which was not fully explored in my work. For example, the graphene hyperbolic metamaterial reported in Chapter 5 can incorporate a gating structure (see Section 5.5) to create a metamaterial with highly tunable photonic density of state. However, creating such a three-dimensional tunable metamaterial is technologically non-trivial because of the need to control many layers of graphene simultaneously. On the other hand, it is much easier and more practical to make electrically tunable metasurfaces with graphene, as graphene and metasurfaces share the same reduced dimensionality compared to their bulk counterparts. In Chapter 6, we have proposed making tunable metasurfaces by combining graphene with a photonic hypercrystal slab. Although our numerical simulations have shown good tunability, future experimental demonstrations are still needed. In my opinion, the combination of graphene and metasurface is a promising research direction, not only because new functionalities can be created, but also because it is technologically practical.

Another promising future direction is graphene plasmonics. So far it is limited by the quality of chemical-vapor-deposited (CVD) graphene, as the defect scattering results

in free-carrier absorption. However, with the rapid advance in growth and transfer of CVD graphene [7,8], it is likely that graphene plasmonics will achieve its potential in the near future. In particular, loss has been the most critical obstacle for plasmonics, which damps the collective oscillation and converts the energy into heat. High-quality graphene has been identified theoretically as an ideal plasmonic material with exceptionally low loss in the infrared to THz ranges [59]. More interestingly, it is possible to compensate for the loss in graphene by optical pumping, as population inversion can be established within ~130 fs after the pump pulse arrives [36]. In addition, because the carrier density can be tuned by electrical gating, graphene is a plasmonic material with tunability.

As a member in the whole family of 2D materials, graphene can combine with other 2D materials to make heterostructures. For example, heterostructure of graphene and MoS_2 has been exploited to make photodetectors [47]. This area is currently in the research stage. Basic phenomena such as charge transfer and heat transfer between different 2D materials are still under study. Nevertheless, with the diversity of the 2D materials, it is anticipated that 2D heterostructures and van der Waals crystals can bring new material properties and novel device concepts in the future.

Section 7.3 Contributions

Here is a list of my publications and other contributions during my period as a Ph.D. student in Prof. Ted Norris's group at the University of Michigan.

Journal papers

1. Y. C. Chang, A. V. Kildishev, E. E. Narimanov, and T. B. Norris, "Metasurface perfect absorber based on guided resonance of a photonic hypercrystal," *in preparation*.
2. Y. C. Chang, C. H. Liu, C. H. Liu, S. Zhang, S. R. Marder, E. E. Narimanov, Z. Zhong, and T. B. Norris, "Realization of mid-infrared graphene hyperbolic metamaterials," *Nature Communications* **7,** 10568 (2016).
3. Y. C. Chang, A. V. Kildishev, E. E. Narimanov, C. H .Liu, C. H. Liu, S. Zhang, S. R. Marder, Z. Zhong, and T. B. Norris, "Mid-infrared hyperbolic metamaterial based on graphene-dielectric multilayers," *Proc. of SPIE* **9544,** 954417 (2015).
4. C. H. Liu, Y. C. Chang, S. Lee, Y. Zhang, Y. Zhang, T. B. Norris, and Z. Zhong, "Ultrafast lateral photo-Dember effect in graphene induced by nonequilibrium hot carrier dynamics," *Nano Lett.* **15,** 4234 (2015).

5. Y. C. Chang, C. H. Liu, C. H. Liu, Z. Zhong, and T. B. Norris, "Extracting the complex optical conductivity of mono- and bilayer graphene by ellipsometry," *Appl. Phys. Lett.* **104**, 261909 (2014).
6. C. H. Liu, Y. C. Chang, T. B. Norris, and Z. Zhong, "Room temperature ultra-broadband and high responsivity graphene photodetectors," *Nature Nanotechnology* **9**, 273 (2014). **** First two authors contribute equally.***
7. S. L Chen, Y. C. Chang, C. Zhang, J. G. Ok, T. Ling, T. B. Norris, and L. J. Guo, "Efficient real-time detection of terahertz pulse radiation based on photoacoustic conversion by carbon nanotube-nanocomposite," *Nature Photonics* **8**, 537 (2014).
8. A. M. DaSilva, Y. C. Chang, T. B. Norris, and A. H. MacDonald, "Enhancement of photonic density of states in finite graphene multilayers,"*Phy. Rev. B* **88**, 195411 (2013).
9. M. J Paul, Y. C. Chang, Z. J. Thompson, A. Stickel, J. Wardini, H. Choi, E. D. Minot, B. Hou, J. A. Nees, T. B. Norris, and Yun-Shik Lee, "High-field terahertz response of graphene," *New Journal of Physics* **15**, 085019 (2013).

Conference

1. Y. C. Chang, A. V. Kildishev, E. E. Narimanov, and T. B. Norris, "Metasurface Perfect Absorber Based on Guided Resonance of Hypercrystal" CLEO: QELS_Fundamental Science, 2016.
2. T. B. Norris, Y. C. Chang, C. H .Liu, C. H. Liu, S. Zhang, S. R. Marder, and Z. Zhong, "Mid-infrared hyperbolic metamaterial based on graphene-dielectric multilayers," SPIE Optics+Photonics 2015.
3. L. J. Prokopeva, Y. C. Chang, N. K. Emani, T. B. Norris, and A. V. Kildishev, "In-the-cloud optimization tool for retrieving experimentally fitted conductivity," SPIE Optics+Photonics 2015.
4. Y. C. Chang, C. H. Liu, C. H. Liu, Z. Zhong, and T. B. Norris, "Mid-infrared hyperbolic metamaterial based on graphene-dielectric multilayers," CLEO: QELS_Fundamental Science, 2015.
5. C. H. Liu, Y. C. Chang, S. Lee, Y. Zhang, Y. Zhang, T. B. Norris, and Z. Zhong, "Lateral photo-Dember effect in graphene," CLEO: QELS_Fundamental Science, 2015.
6. Y. C. Chang, C. H. Liu, Z. Zhong, and T. B. Norris, "Extracting the complex optical conductivity of true two-dimensional layers by ellipsometry," CLEO: Science and Innovations, 2014.
7. C. H. Liu , Y. C. Chang , N. Dissanayake , Y. Zhang , and Z. Zhong, "Hot Carrier Transport at the Graphene-Metal Interface Induced by Strong Lateral Photo-Dember Effect," APS March Meeting, 2013.
8. C. H. Liu, Y. C. Chang, T. B. Norris, and Z. Zhong, "Room Temperature Ultra-Broadband and High Responsivity Photodetectors Based on Graphene Double-Layer Heterostructures," MRS fall meeting, 2013.

Software

1. Development of the free ellipsometric fitting tool “PhotonicVASEfit” on nanohub.org (https://nanohub.org/resources/photonicvasefit)

APPENDICES

APPENDIX A

Derivation of the optical conductivity of graphene

Section A. 1 Universal interband conductivity

When there is no Pauli blocking, it can be calculated from the Fermi's golden rule that the interband conductivity of graphene $\sigma_{\text{inter}}(\omega)$ equals $\sigma_0 = e^2/(4\hbar)$ [24,192]. Here I follow the derivation of Ref. 192. When graphene interacts with light, the Hamiltonian perturbed by light can be obtained by replacing $\mathbf{p}$ with $\mathbf{p} + e\mathbf{A}$.

$$\mathcal{H} = v_{\mathrm{F}}\boldsymbol{\sigma} \cdot (\mathbf{p} + e\mathbf{A}) = \mathcal{H}_0 + \mathcal{H}' e^{i\omega t}, \tag{1}$$

where $\mathbf{A} = \mathbf{A_0}e^{i\omega t} = (i\mathbf{E_0}/\omega)e^{i\omega t}$. Without loss of generality, we assume the electric field is in x direction. $\mathcal{H}_0 = v_{\mathrm{F}}\boldsymbol{\sigma} \cdot \mathbf{p}$ is the unperturbed Dirac Hamiltonian. According to Eq. (1), we can write the interaction Hamiltonian as

$$\mathcal{H}' = iev_{\mathrm{F}}\sigma_x \frac{\mathrm{E}_0}{\omega}, \tag{2}$$

where $\sigma_x = \begin{pmatrix} 0 & 1 \\ 1 & 0 \end{pmatrix}$. Next, we need to calculate the matrix element $\langle \mathrm{f}|\mathcal{H}'|\mathrm{i}\rangle$, where

$$|\mathrm{i}\rangle = \frac{1}{\sqrt{2}}\begin{pmatrix} e^{-i\theta_{\boldsymbol{q}}/2} \\ -e^{i\theta_{\boldsymbol{q}}/2} \end{pmatrix} |\boldsymbol{q}\rangle \quad , \tag{3}$$

$$|\mathrm{f}\rangle = \frac{1}{\sqrt{2}}\begin{pmatrix} e^{-i\theta_{\boldsymbol{q}'}/2} \\ e^{i\theta_{\boldsymbol{q}'}/2} \end{pmatrix} |\boldsymbol{q}'\rangle \tag{4}$$

are the initial and final states (see Section 1.2). By straightforward calculation, we can then obtain

$$|\langle \mathrm{f}|\mathcal{H}'|\mathrm{i}\rangle|^2 = e^2 v_\mathrm{F}^2 \frac{|\mathrm{E}_0|^2}{\omega^2} \sin^2\theta_{\boldsymbol{q}} \delta_{\boldsymbol{q}\boldsymbol{q}'} \quad . \tag{5}$$

Notice that the $\sin^2\theta_{\boldsymbol{q}}$ factor in Eq. (5) indicates that an x-polarized electromagnetic field cannot induce interband transition for a state with $\theta_{\boldsymbol{q}} = 0$ [193]. From the Fermi's golden rule, the transition rate is given by

$$w_{\mathrm{i}\to\mathrm{f}} = \frac{2\pi}{\hbar} |\langle \mathrm{f}|\mathcal{H}'|\mathrm{i}\rangle|^2 \delta(E_\mathrm{f} - E_\mathrm{i} - \hbar\omega) \quad , \tag{6}$$

The power absorbed by graphene per unit area can be expressed in terms of the transition rate

$$P_\mathrm{abs} = 4\hbar\omega \sum_{\mathrm{i,f}} w_{\mathrm{i}\to\mathrm{f}} \, , \tag{7}$$

where we sum over all initial and final states. The factor of 4 is due to the spin and valley degeneracies. Inserting Eq. (5) and Eq. (6) into Eq. (7), we get

$$\begin{aligned} P_\mathrm{abs} &= 4\hbar\omega \, \frac{2\pi}{\hbar} e^2 v_\mathrm{F}^2 \frac{|\mathrm{E}_0|^2}{\omega^2} \int \frac{\mathrm{d}^2\boldsymbol{q}}{(2\pi)^2} \sin^2\theta_{\boldsymbol{q}} \delta(2\hbar v_\mathrm{F} q - \hbar\omega) \\ &= \frac{e^2}{2\hbar} |\mathrm{E}_0|^2 \qquad . \end{aligned} \tag{8}$$

On the other hand, we can express the power absorbed by graphene per unit area in terms of the optical conductivity.

$$P_\mathrm{abs} = 2 \, \mathrm{Re} \, (\mathrm{J} \cdot \mathrm{E}_0{}^*) = 2 \, \mathrm{Re} \, \sigma_\mathrm{inter} \, |\mathrm{E}_0|^2, \tag{9}$$

where J is the surface current induced by the electromagnetic field. Notice that in this convention, the physical electric field is $\mathrm{E}_0 e^{i\omega t} + \mathrm{E}_0{}^* e^{-i\omega t} = 2|\mathrm{E}_0|\cos(\omega t + \phi)$, where $\mathrm{E}_0 = |\mathrm{E}_0| e^{i\phi}$. By comparing Eq. (8) and Eq. (9), we obtain the interband conductivity of graphene:

$$\sigma_\mathrm{inter} = \frac{e^2}{4\hbar} \, , \tag{10}$$

which is the universal conductivity of graphene.

Section A. 2 Drudic intraband conductivity

The easiest way to derive the intraband conductivity of graphene is by taking a semi-classical approach. Here we follow the derivation in Ref. 25. Consider doped graphene with a Fermi energy of E_{F} such that $E_{\mathrm{F}} \gg k_{\mathrm{B}}T$. We start with the Boltzmann equation

$$\frac{\partial}{\partial t} f_{\boldsymbol{k}}(t) - \frac{\partial}{\hbar \partial \boldsymbol{k}} f_{\boldsymbol{k}}(t) \cdot e\boldsymbol{E}(t) = 0, \tag{11}$$

where $f_{\boldsymbol{k}}(t)$ is the momentum distribution function. The exact solution of Eq. (11) is given by

$$f_{\boldsymbol{k}}(t) = F_0(\boldsymbol{k} - \boldsymbol{k}_0(t)), \tag{12}$$

where

$$F_0(\boldsymbol{k}) = 1/\{1 + \exp[(v_{\mathrm{F}}\hbar k - E_{\mathrm{F}})/k_{\mathrm{B}}T]\} \tag{13}$$

is the Fermi-Dirac function, and

$$\boldsymbol{k}_0(t) = -(e/\hbar) \int_{-\infty}^{t} \boldsymbol{E}(t')dt' \tag{14}$$

comes the semi-classical equation of motion. The Fermi velocity is denoted by v_{F}. We can then calculate the surface current in graphene:

$$\boldsymbol{j}(t) = -\frac{gev_{\mathrm{F}}}{(2\pi)^2} \int d^2\boldsymbol{k}\, \frac{\boldsymbol{k}}{k} f_{\boldsymbol{k}}(t), \tag{15}$$

where $g = 4$ due to the spin and valley degeneracies. In the case that $k_0(t) \ll k_{\mathrm{F}} \triangleq E_{\mathrm{F}}/(v_{\mathrm{F}}\hbar)$ and $T \to 0$, Eq. (15) can be approximated to

$$\boldsymbol{j}(t) \cong -env_{\mathrm{F}} \frac{\boldsymbol{k}_0(t)}{k_{\mathrm{F}}}, \tag{16}$$

where n is the carrier density. We can now switch to the frequency domain by letting $\boldsymbol{j}(t) = \mathbf{J}(\omega)e^{-i\omega t}$, $\boldsymbol{k}_0(t) = \mathbf{k}_0(\omega)\, e^{-i\omega t}$ and $\boldsymbol{E}(t) = \mathbf{E}(\omega)\, e^{-i\omega t}$. Eq. (14) can be written as $\mathbf{k}_0(\omega) = e\mathbf{E}/(i\hbar\omega)$. The surface current is then given by

$$\begin{aligned} \mathbf{j}(\omega) &\cong -\frac{env_{\mathrm{F}}e\mathbf{E}(\omega)}{(ik_{\mathrm{F}}\hbar\omega)} \\ &= i\frac{4\sigma_0}{\pi}\frac{E_{\mathrm{F}}}{\hbar\omega}\mathbf{E}(\omega), \end{aligned} \tag{17}$$

where $\sigma_0 = e^2/(4\hbar)$ is the universal conductivity of graphene. We can further apply the relaxation-time approximation by replacing ω with $\omega + i\gamma$, where γ is the intraband scattering rate [59]. Therefore, we obtain the Drudic intraband conductivity of graphene

$$\sigma_{\text{intra}}(\omega) = i\frac{4\sigma_0}{\pi}\frac{E_{\text{F}}}{\hbar\omega + i\hbar\gamma}. \tag{18}$$

APPENDIX B

Transfer matrix of an interface with a sheet conductivity

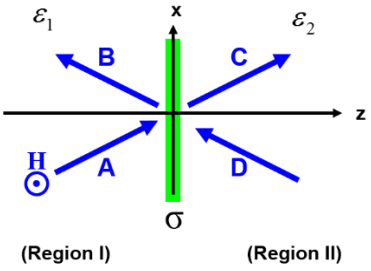

Figure A. 1 **The schematic of an interface with a sheet conductivity σ sandsiched by two media.**

The transfer matrix method is very useful for calculating optical responses of layered media [194]. Here we extend the conventional transfer matrix to allow an interface to have a sheet conducitivity. Consider an interface with a sheet conductivity σ sandwiched by two media with permittivities of ε_1 and ε_2, as shown by **Error! Reference source not ound.**. The sheet conductivity can come from either a graphene layer (as in Chapter 4 and 5), or a metasurface (as in Chapter 6). The magnetic field and the electric field in TM polarization can be expressed as:

$$H_y = \begin{cases} \left(Ae^{ik_{1z}z} + Be^{-ik_{1z}z}\right)e^{ik_t x} & \text{(Region I)} \\ \left(Ce^{ik_{2z}z} + De^{-ik_{2z}z}\right)e^{ik_t x} & \text{(Region II)} \end{cases}$$

$$E_x = \begin{cases} \dfrac{k_{1z}}{\omega\varepsilon_1}\left(Ae^{ik_{1z}z} - Be^{-ik_{1z}z}\right)e^{ik_t x} & \text{(Region I)} \\ \dfrac{k_{2z}}{\omega\varepsilon_2}\left(Ce^{ik_{2z}z} - De^{-ik_{2z}z}\right)e^{ik_t x} & \text{(Region II)} \end{cases}, \qquad (19)$$

where $k_{1z}^2 + k_t^2 = \varepsilon_1 \left(\frac{\omega}{c}\right)^2$ and $k_{2z}^2 + k_t^2 = \varepsilon_2 \left(\frac{\omega}{c}\right)^2$. The boundary conditions require

$$\begin{aligned} E_x^{(I)} &= E_x^{(II)} \\ H_y^{(I)} - H_y^{(II)} &= J_{sx} = \sigma E_x \end{aligned}, \tag{20}$$

where we allow discontinuity in the magnetic fields because of the presnsence of surface current. The superscripts indicate the medium in which the filed is evaluated. By rearrngeing the boundary conditions Eq. (20), we can obtain the transfer matrix that connects the fields across the interface for TM polarization:

$$\begin{pmatrix} C \\ D \end{pmatrix} = \frac{1}{2} \begin{pmatrix} 1 + \frac{k_{1z}}{k_{2z}} \frac{\varepsilon_2}{\varepsilon_1} - \frac{\sigma Z_0}{\varepsilon_1} \frac{k_{1z}}{k_0} & 1 - \frac{k_{1z}}{k_{2z}} \frac{\varepsilon_2}{\varepsilon_1} + \frac{\sigma Z_0}{\varepsilon_1} \frac{k_{1z}}{k_0} \\ 1 - \frac{k_{1z}}{k_{2z}} \frac{\varepsilon_2}{\varepsilon_1} - \frac{\sigma Z_0}{\varepsilon_1} \frac{k_{1z}}{k_0} & 1 + \frac{k_{1z}}{k_{2z}} \frac{\varepsilon_2}{\varepsilon_1} + \frac{\sigma Z_0}{\varepsilon_1} \frac{k_{1z}}{k_0} \end{pmatrix} \begin{pmatrix} A \\ B \end{pmatrix} . \tag{21}$$

We can further obtain the reflection coefficient for TM polarization using the derived transfer matrix Eq. (21).

$$r_p = \frac{\varepsilon_1 / k_{1z} - \varepsilon_2 / k_{2z} - \sigma / \omega}{\varepsilon_1 / k_{1z} + \varepsilon_2 / k_{2z} + \sigma / \omega}, \tag{22}$$

which is a modified version of the Fresnel equation. Similarly, we can derive the transfer matrix and reflection coefficient for TE polarization.

$$\begin{pmatrix} C \\ D \end{pmatrix} = \frac{1}{2} \begin{pmatrix} 1 + \frac{k_{1z}}{k_{2z}} - \sigma Z_0 \frac{k_0}{k_{2z}} & 1 - \frac{k_{1z}}{k_{2z}} - \sigma Z_0 \frac{k_0}{k_{2z}} \\ 1 - \frac{k_{1z}}{k_{2z}} + \sigma Z_0 \frac{k_0}{k_{2z}} & 1 + \frac{k_{1z}}{k_{2z}} + \sigma Z_0 \frac{k_0}{k_{2z}} \end{pmatrix} \begin{pmatrix} A \\ B \end{pmatrix}, \tag{23}$$

$$r_s = \frac{k_{1z} - k_{2z} - \sigma \omega \mu_0}{k_{1z} + k_{2z} + \sigma \omega \mu_0} . \tag{24}$$

APPENDIX C

Derivation of the dispersion relation of the Bloch waves in graphene-dielectric multilayers

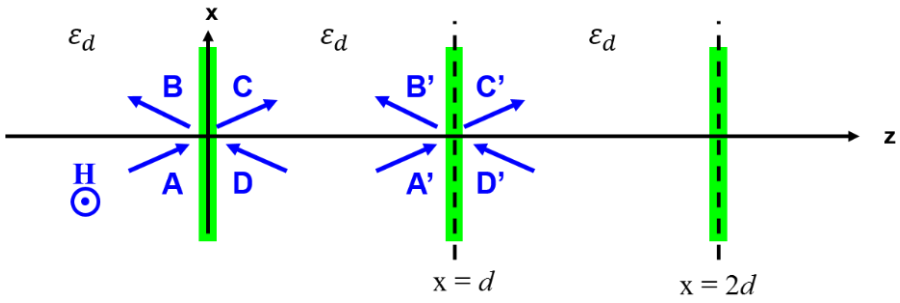

Figure A. 2 **The schematic of a periodic structure consisting of graphene-dielectric multilayers.**

Here we show the derivation of the dispersion relation of the TM Bloch waves in the graphene-dielectric multilayers. Consider an infinite periodic graphene-dielectric multilayers shown in Figure A. 2. The field at $x = d^-$ can be obtained from the field at $x = 0^-$ using the transfer matrix associated with progation in the dielectric and the transfer matrix associated with the interface:

$$\begin{aligned}\begin{pmatrix} A' \\ B' \end{pmatrix} &= \begin{pmatrix} e^{ik_d d} & 0 \\ 0 & e^{-ik_d d} \end{pmatrix} \begin{pmatrix} C \\ D \end{pmatrix} \\ &= \begin{pmatrix} e^{ik_d d}\left[1-\dfrac{\sigma Z_0}{2\varepsilon_d}\left(\dfrac{k_d}{k_0}\right)\right] & e^{ik_d d}\dfrac{\sigma Z_0}{2\varepsilon_d}\left(\dfrac{k_d}{k_0}\right) \\ -e^{-ik_d d}\dfrac{\sigma Z_0}{2\varepsilon_d}\left(\dfrac{k_d}{k_0}\right) & e^{-ik_d d}\left[1+\dfrac{\sigma Z_0}{2\varepsilon_d}\left(\dfrac{k_d}{k_0}\right)\right] \end{pmatrix} \begin{pmatrix} A \\ B \end{pmatrix},\end{aligned} \tag{25}$$

where we have used Eq. (21), the transfer matrix we derived in APPENDIX B. k_d represents the z-component of the wavevector in the dielectric. To find the Bloch wave, we need to solve this eigenvalue problem

$$\begin{pmatrix} A' \\ B' \end{pmatrix} = e^{iKd} \begin{pmatrix} A \\ B \end{pmatrix}, \tag{26}$$

where K is the Bloch wave vector. We therefore obtain the characteristic equation of the eigenvalue problem

$$Det \begin{pmatrix} e^{ik_d d}\left[1-\frac{\sigma Z_0}{2\varepsilon_d}\left(\frac{k_d}{k_0}\right)\right]-e^{iKd} & e^{ik_d d}\frac{\sigma Z_0}{2\varepsilon_d}\left(\frac{k_d}{k_0}\right) \\ -e^{-ik_d d}\frac{\sigma Z_0}{2\varepsilon_d}\left(\frac{k_d}{k_0}\right) & e^{-ik_d d}\left[1+\frac{\sigma Z_0}{2\varepsilon_d}\left(\frac{k_d}{k_0}\right)\right]-e^{iKd} \end{pmatrix} = 0 . \tag{27}$$

With some algebra, the characteristic equation can be written in this form

$$\cos(Kd) = \cos(k_d d) - i\frac{\sigma Z_0}{2\varepsilon_d}\left(\frac{k_d}{k_0}\right)\sin(k_d d), \tag{28}$$

which gives the dispersion relation for TM Bloch wave. With the same procedure, we can also derive the dispersion relation for TE Bloch waves in the graphene-dielectric multilayers, which is given by

$$\cos(Kd) = \cos(k_d d) - i\frac{\sigma Z_0}{2}\left(\frac{k_0}{k_d}\right)\sin(k_d d) \ . \tag{29}$$

APPENDIX D

Derivation of the effective permittivities of graphene-dielectric multilayers using quasi-static approximation

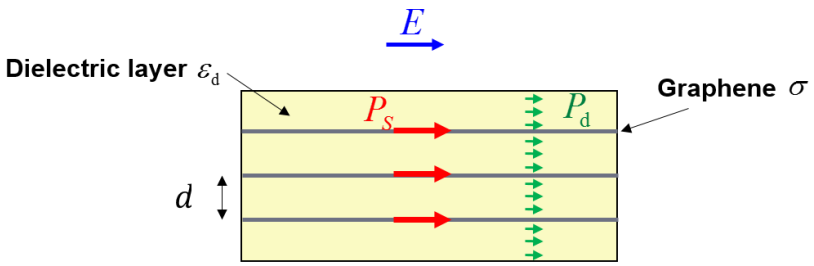

Figure A. 3 **The schematic of the graphene-dielectric multilayers in the quasi-static approximation.**

Because the period of the graphene hyperbolic metamaterial is much smaller than the wavelength, we can use quasi-static approximation to derive the effective permittivities. As plotted in Figure A. 3, when the electric field E is parallel to the interfaces, surface current J_s is generated in graphene. Surface current J_s is given by

$$J_s = \sigma E \,, \tag{30}$$

where σ is the optical conductivity of graphene. Because the surface current is related to surface polarization by $J_s = \frac{dP_s}{dt} = -i\omega P_s$, we can write

$$P_s = i\frac{\sigma E}{\omega} \,. \tag{31}$$

On the other hand, the polarization in the dielectric induced by the electric field is given by

$$P_{\mathrm{d}} = (\varepsilon_{\mathrm{d}} - 1)\varepsilon_0 E\ . \tag{32}$$

Next, we can average the polarization over a unit cell with thickness of d:

$$\begin{aligned} P_{\mathrm{average}} &= P_{\mathrm{d}} + \tfrac{P_s}{d} \\ &= \left(\varepsilon_{\mathrm{d}} - 1 + i\tfrac{\sigma}{\omega\varepsilon_0 d}\right)\varepsilon_0 E \\ &= (\varepsilon_{\mathrm{eff}} - 1)\varepsilon_0 E\ , \end{aligned} \tag{33}$$

where $\varepsilon_{\mathrm{eff}}$ is the effective permittivity. Therefore, we obtain the effective permittivity when E is parallel to graphene surface

$$\begin{aligned} \varepsilon_{\mathrm{eff}} &= \varepsilon_{\mathrm{d}} + i\frac{\sigma}{\omega\varepsilon_0 d} \\ &= \varepsilon_{\mathrm{d}} + i\tfrac{\sigma Z_0}{2\pi}\left(\tfrac{\lambda}{d}\right), \end{aligned} \tag{34}$$

which is the same as Eq. (3) of Chapter 5. It is also clear that, because the out-of-plane response of graphene is neglegible, when the electric field E is perpendicular to the graphene surface, the effective permittivity derived in the quasi-static approximation is simply ε_{d}.

APPENDIX E

Measure the dielectric thickness of the graphene-dielectric multilayer structure by ellipsometer

The Al_2O_3 dielectric layers are deposited by the atomic layer deposition (ALD). Before fabricating our metamaterial sample, we have calibrated the recipe of ALD in order to deposit the desired 10-nm layers. However, we still need to characterize the Al_2O_3 thickness of the sample we actually fabricated, as the deposition rate of ALD can depend on the surface conditions. To obtain the dielectric thickness, we measure the sample with M-2000 ellipsometer after each step in the fabrication and acquire the ellipsometric angles Ψ and Δ. More specifically, we have measured 10 different structures in the intermediate steps, including G/S, dG/S, GdG/S, dGdG/S, GdGdG/S, dGdGdG/S, GdGdGdG/S, dGdGdGdG/S, GdGdGdGdG/S and dGdGdGdGdG/S, where we denote the CaF_2 substrate, chemically-doped graphene, and Al_2O_3 dielectric layer with S, G, and d, respectively. After acquiring the entire set of data, we fit all data together with the same set of unknown free parameters: the conductivity of graphene, the refractive index and thickness of the dielectric. We assume all the graphene layers have the same conductivity, and all the dielectric layers have the same refractive index and thickness. The graphene conductivity is parameterized by cubic splines, and the refractive index of Al_2O_3 is parameterized by Cauchy's equation.

The fitting is performed within a wavelength range between 500 nm and 850 nm. This wavelength range is selected such that the graphene conductivity in this range is practically independent of the doping level. This is because the doping level of graphene

can vary during the fabrication steps, especially by the elevated temperature and low pressure in the ALD chamber. If the photon energies is significantly larger than $2E_F$ such that the Pauli blocking is not present (E_F denotes the Fermi energy), the graphene conductivity is independent of doping in theory. This is also verified experimentally with our ellipsometry characterization of graphene with different doping levels, except that we have found the imaginary conductivity varies slightly at very short wavelengths, which is probably due to the sub-monolayer thickness of the "magic blue" dopant. The wavelength rage between 500 nm and 850 nm is a practical choice of using a constant conductivity for all graphene layers of the structures in the intermediate steps.

Figure A. 4 shows the measured Ψ and Δ for all 10 different structures in the intermediate steps. The measurement is performed with 3 different incident angles: 47°, 57°, and 67°. By fitting the data with the model described above, we extract an Al_2O_3 thickness of 10.4 nm.

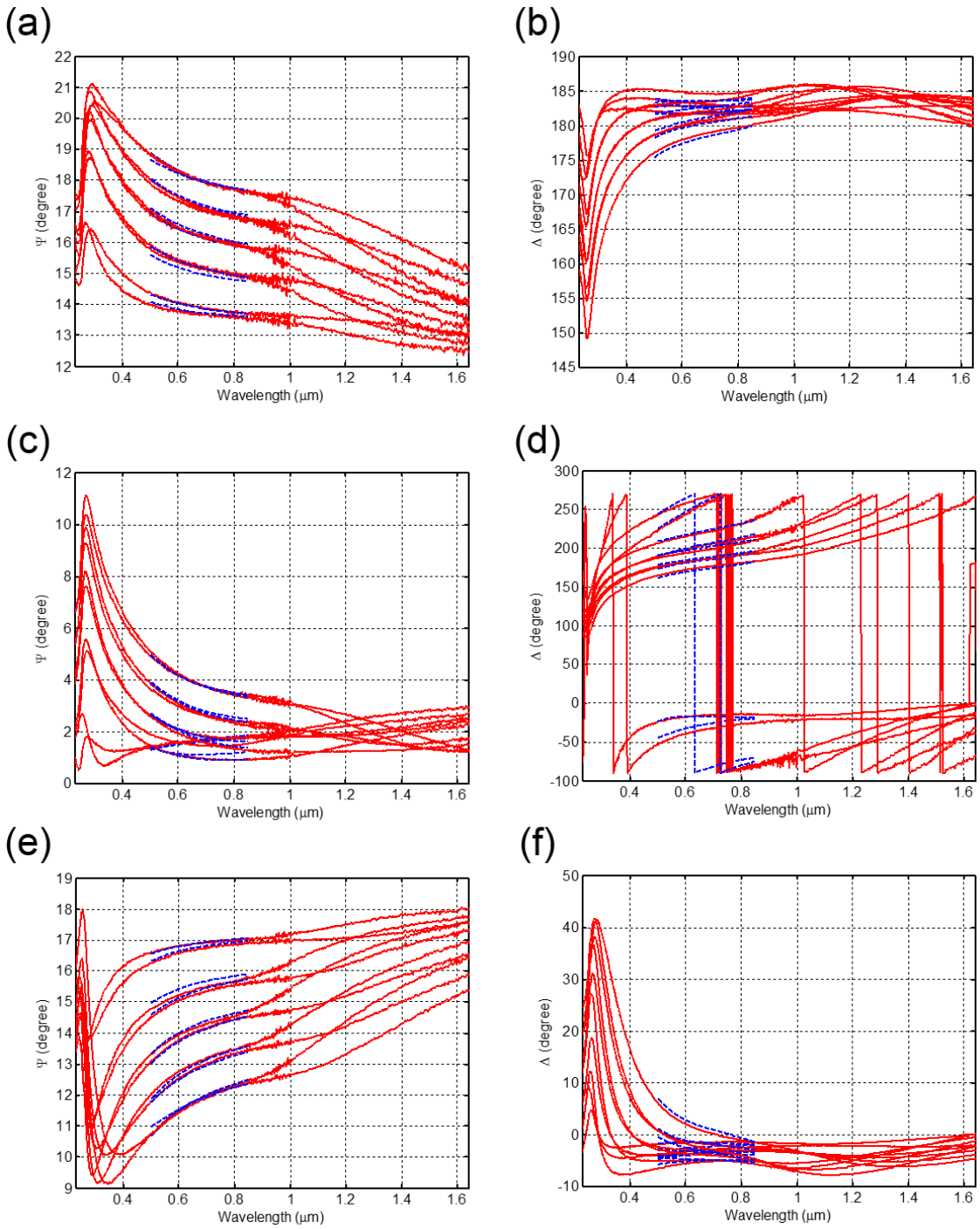

Figure A. 4 **(a) Ψ at 47° (b) Δ at 47° (c) Ψ at 57° (d) Δ at 57° (e) Ψ at 67° (f) Δ at 67° for all 10 different structures in the intermediate steps.** The red solid lines are the data, and the blue dash lines are the fit.

APPENDIX F

Waveguide modes of a hyperbolic slab in a symmetric cladding environment

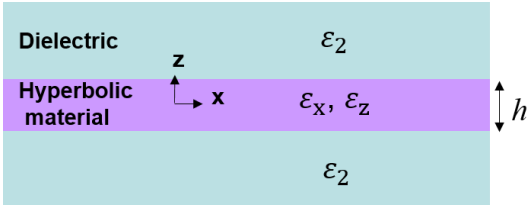

Figure A. 5 **The schematic of a hyperbolic slab sandwiched in a symmetric cladding environment.**

Consider a slab of a hyperbolic material sandwiched by another dielectric material, as shown in Figure A. 5. Here we are interested in the TM polarization because the hyperbolic dispersion only exists in this polarization. The magnetic field of an even mode can be written as

$$H_y = \begin{cases} cos(kh/2)e^{-\alpha_2(z-h/2)}e^{i\beta x}, & z > \frac{h}{2} \\ cos(kz)\, e^{i\beta x}, & \frac{-h}{2} \le z \le \frac{h}{2} \\ cos(kh/2)e^{\alpha_2(z+h/2)}e^{i\beta x}, & z < \frac{-h}{2} \end{cases}, \tag{35}$$

where $\beta^2 - \alpha_2^2 = \varepsilon_2 \left(\frac{\omega}{c}\right)^2$ and $\frac{k^2}{\varepsilon_x} + \frac{\beta^2}{\varepsilon_z} = \left(\frac{\omega}{c}\right)^2$.Using the curl equation of the Maxwell's equations, we can obtain the electric field in the x-direction:

$$E_x = \begin{cases} \frac{i\alpha_2}{\omega\varepsilon_0\varepsilon_2} cos(kh/2) e^{-\alpha_2(z-h/2)} e^{i\beta x}, & z > \frac{h}{2} \\ \frac{ik}{\omega\varepsilon_0\varepsilon_x} sin(kz)\, e^{i\beta x}, & \frac{-h}{2} \le z \le \frac{h}{2} \\ \frac{-i\alpha_2}{\omega\varepsilon_0\varepsilon_2} cos(kh/2) e^{\alpha_2(z+h/2)} e^{i\beta x}, & z < \frac{-h}{2} \end{cases}, \quad (36)$$

The boundary condition requires the continuity of E_x across the boundary at $z = h/2$, from which we can obtain the expression for the dispersion relation [184].

$$\frac{\alpha_2/k}{\varepsilon_2/\varepsilon_x} = \tan(kh/2). \quad (37)$$

With similar procedure, we can obtain the dispersion relation for odd modes, which is give by

$$\frac{\alpha_2/k}{\varepsilon_2/\varepsilon_x} = -\cot(kh/2). \quad (38)$$

BIBLIOGRAPHY

BIBLIOGRAPHY

1. Novoselov, K. S., Geim, A. K., Morozov, S. V., Jiang, D., Zhang, Y., Dubonos, S. V., Grigorieva, I. V. & Firsov, A. A. Electric field effect in atomically thin carbon films. *Science* **306,** 666-669 (2004).
2. Novoselov, K. S. A., Geim, A. K., Morozov, S., Jiang, D., Katsnelson, M., Grigorieva, I. V., Dubonos, S. V. & Firsov, A. Two-dimensional gas of massless Dirac fermions in graphene. *Nature* **438,** 197-200 (2005).
3. Gorbachev, R. V., Riaz, I., Nair, R. R., Jalil, R., Britnell, L., Belle, B. D., Hill, E. W., Novoselov, K. S., Watanabe, K., Taniguchi, T., Geim, A. K. & Blake, P. Hunting for Monolayer Boron Nitride: Optical and Raman Signatures. *Small* **7**, 465 (2011).
4. Mak, K. F., Lee, C., Hone, J., Shan, J. & Heinz, T. F. Atomically Thin MoS_2: A New Direct-Gap Semiconductor. *Phys. Rev. Lett.* **105**, 136805 (2010).
5. Geim, A. K. & Grigorieva, I. V. Van der Waals heterostructures. *Nature* **499,** 419 (2013).
6. Ling, X., Wang, H., Huang, S., Xia, F. & Dresselhaus, M. S. The renaissance of black phosphorus. *Proceedings of the National Academy of Sciences* **112,** 4523-4530 (2015).
7. Hao, Y. *et. al*. The role of surface oxygen in the growth of large single-crystal graphene on copper. *Science* **342,** 720-723 (2013).
8. Banszerus, L., Schmitz, M., Engels, S., Dauber, J., Oellers, M., Haupt, F., Watanabe, K., Taniguchi, T., Beschoten B. & Stampfer, C. Ultrahigh-mobility graphene devices from chemical vapor deposition on reusable copper. *Science Advances* **1,** e1500222 (2015).
9. Kang, K., Xie, S., Huang, L., Han, Y., Huang, P.Y., Mak, K.F., Kim, C.J., Muller, D. & Park, J. High-mobility three-atom-thick semiconducting films with wafer-scale homogeneity. *Nature* **520,** 656-660 (2015).
10. Blees, M.K., Barnard, A.W., Rose, P.A., Roberts, S.P., McGill, K.L., Huang, P.Y., Ruyack, A.R., Kevek, J.W., Kobrin, B., Muller, D.A. & McEuen, P.L. Graphene kirigami. *Nature* **524,** 204-207 (2015).
11. Yu, N. & Capasso, F. Flat optics with designer metasurfaces. *Nature Materials* **13,** 139-150 (2014).
12. Holloway, C. L., Kuester, E. F., Gordon, J. A., Hara, J. O., Booth, J. & Smith, D. R. An overview of the theory and applications of metasurfaces: The two-dimensional equivalents of metamaterials. *Antennas and Propagation Magazine, IEEE* **54,** 10-35 (2012).
13. Geim, A. K. Graphene: status and prospects. *Science* **324,** 1530-1534 (2009).
14. Castro Neto, A.H., Guinea, F., Peres, N. M. R., Novoselov, K. S. & Geim, A. K. The electronic properties of graphene. *Reviews of Modern Physics* **81,** 109 (2009).
15. Wallace, P. R. The band theory of graphite. *Physical Review* **71,** 622 (1947).

16. Semenoff, G. W. Condensed-matter simulation of a three-dimensional anomaly. *Physical Review Letters* **53,** 2449 (1984).
17. Kim, P. Graphene and relativistic quantum physics. *Semin. Poincare* 18, 1-21 (2014).
18. Sarma, S. D., Adam, S., Hwang, E. H. & Rossi, E. Electronic transport in two-dimensional graphene. *Reviews of Modern Physics* **83,** 407 (2011).
19. Abergel, D. S. L., Apalkov, V., Berashevich, J., Ziegler, K. & Chakraborty, T. Properties of graphene: a theoretical perspective. *Advances in Physics* **59,** 261-482 (2010).
20. Wu, X., Li, X., Song, Z., Berger, C. & de Heer, W. A. Weak antilocalization in epitaxial graphene: evidence for chiral electrons. *Physical Review Letters* **98,** 136801 (2007).
21. Falkovsky, L. A. & Varlamov, A. A. Space-time dispersion of graphene conductivity. *Eur. Phys. J. B* **56**, 281 (2007).
22. Falkovsky, L. A. & Pershoguba, S. S. Optical far-infrared properties of a graphene monolayer and multilayer. *Phys. Rev. B* **76**, 153410 (2007).
23. Stauber, T., Peres, N. R. M. & Geim, A. K. Optical conductivity of graphene in the visible region of the spectrum. *Phys. Rev. B* **78,** 085432 (2008).
24. Nair, R. R., Blake, P., Grigorenko, A. N., Novoselov, K. S., Booth, T. J., Stauber, T., Peres, N. M. R. & Geim, A. K. Fine Structure Constant Defines Visual Transparency of Graphene. *Science* **320,** 1308 (2008).
25. Mikhailov, S. A. & Ziegler, K. Nonlinear electromagnetic response of graphene: frequency multiplication and the self-consistent-field effects. *Journal of Physics: Condensed Matter* **20,** 384204 (2008).
26. Mak, K. F., Shan, J. & Heinz, T. F. Seeing Many-Body Effects in Single- and Few-Layer Graphene: Observation of Two-Dimensional Saddle-Point Excitons. *Phys. Rev. Lett.* **106,** 046401 (2011).
27. Yang, L., Deslippe, J., Park, C. H., Cohen, M. L. & Louie, S. G. Excitonic Effects on the Optical Response of Graphene and Bilayer Graphene. *Phys. Rev. Lett.* **103,** 186802 (2009).
28. Yan, H., Li, X., Chandra, B., Tulevski, G., Wu, Y., Freitag, M., Zhu, W., Avouris, P. & Xia, F. Tunable infrared plasmonic devices using graphene/insulator stacks. *Nature Nanotechnology* **7,** 330-334 (2012).
29. Chang, Y. C., Liu, C. H., Liu, C. H., Zhang, S., Marder, S. R., Narimanov, E. E., Zhong, Z & Norris, T. B. Realization of mid-infrared graphene hyperbolic metamaterials. *Nature Communications* **7,** 10568 (2016).
30. Yao, Y., Shankar, R., Kats, M. A., Song, Y., Kong, J., Loncar, M. & Capasso, F. Electrically tunable metasurface perfect absorbers for ultrathin mid-infrared optical modulators. *Nano letters* **14,** 6526-6532 (2014).
31. Liu, M., Yin, X., Ulin-Avila, E., Geng, B., Zentgraf, T., Ju, L., Wang, F. and Zhang, X. A graphene-based broadband optical modulator. *Nature* **474,** 64-67 (2011).

32. Phare, C. T., Lee, Y. H. D., Cardenas, J. & Lipson, M. Graphene electro-optic modulator with 30 GHz bandwidth. *Nature Photonics* **9,** 511-514 (2015).
33. Jang, M.S., Brar, V.W., Sherrott, M.C., Lopez, J.J., Kim, L., Kim, S., Choi, M & Atwater, H.A., Tunable large resonant absorption in a midinfrared graphene Salisbury screen. *Physical Review B* **90,** 165409 (2014).
34. Ju, L., Geng, B., Horng, J., Girit, C., Martin, M., Hao, Z., Bechtel, H.A., Liang, X., Zettl, A., Shen, Y.R. & Wang, F. Graphene plasmonics for tunable terahertz metamaterials. *Nature Nanotechnology*, **6,** 630-634 (2011).
35. Wang, F., Zhang, Y., Tian, C., Girit, C., Zettl, A., Crommie, M. & Shen, Y. R. Gate-variable optical transitions in graphene. *Science* **320,** 206-209 (2008).
36. Gierz, I. *et al.* Snapshots of non-equilibrium Dirac carrier distributions in graphene. *Nature materials* **12**, 1119 (2013).
37. Mihnev, M.T., Divin, C.J., Kadi, F., Winzer, T., Lee, S., Liu, C.H., Zhong, Z., Wang, X., Ruoff, R.S., Berger, C. de Heer, W.A., Malic, E., Knorr, A. & Norris, T. B. Microscopic origins of the terahertz carrier relaxation and cooling dynamics in graphene. *In CLEO: QELS_Fundamental Science*, FTu4B-5 (2015).
38. Mihnev, M. T. *et al.* Microscopic origins of the terahertz carrier relaxation and cooling dynamics in graphene. *Nat. Commun.* **7,** 11617 (2016).
39. Koppens, F. H. L., Mueller, T., Avouris, P., Ferrari, A. C., Vitiello, M. S. & Polini, M. Photodetectors based on graphene, other two-dimensional materials and hybrid systems. *Nature Nanotechnology* **9,** 780-793 (2014).
40. Bonaccorso, F., Sun, Z., Hasan, T. & Ferrari, A. C. Graphene photonics and optoelectronics. *Nature Photonics* **4,** 611-622 (2010).
41. Chang, Y. C., Liu, C. H., Liu, C. H., Zhong, Z. & Norris, T. B. Extracting the complex optical conductivity of mono- and bilayer graphene by Ellipsometry. *Appl. Phys. Lett.* **104,** 261909 (2014).
42. Mak, K. F., Ju, L., Wang, F. & Heinz, T. F. Optical spectroscopy of graphene: from the far infrared to the ultraviolet. *Solid State Communications* **152**, 1341 (2012).
43. Xia, F. N., Mueller, T., Lin, Y. M., Valdes-Garcia, A. & Avouris, P. Ultrafast graphene photodetector. *Nature Nanotechnology* **4,** 839 (2009).
44. Gabor, N.M., Song, J.C., Ma, Q., Nair, N.L., Taychatanapat, T., Watanabe, K., Taniguchi, T., Levitov, L.S. & Jarillo-Herrero, P. Hot carrier–assisted intrinsic photoresponse in graphene. *Science* **334,** 648-652 (2011).
45. Yan, J., Kim, M.H., Elle, J.A., Sushkov, A.B., Jenkins, G.S., Milchberg, H.W.M., Fuhrer, M.S. & Drew, H.D. Dual-gated bilayer graphene hot-electron bolometer. *Nature Nanotechnology* **7,** 472-478 (2012).
46. Konstantatos, G., Badioli, M., Gaudreau, L., Osmond, J., Bernechea, M., de Arquer, F. P. G., Gatti, F. & Koppens, F. H. Hybrid graphene-quantum dot phototransistors with ultrahigh gain. *Nature Nanotechnology* **7,** 363 (2012).

47. Roy, K., Padmanabhan, M., Goswami, S., Sai, T. P., Ramalingam, G., Raghavan, S. & Ghosh, A. Graphene-MoS_2 hybrid structures for multifunctional photoresponsive memory devices. *Nature Nanotechnology* **8,** 826 (2013).
48. Liu, C. H., Chang, Y. C., Norris, T. B. & Zhong, Z. Graphene photodetectors with ultra-broadband and high responsivity at room temperature. *Nature nanotechnology* **9,** 273 (2014).
49. Liu, C. H., Chang, Y. C., Lee, S., Zhang, Y., Zhang, Y., Norris, T. B. & Zhong, Z. Ultrafast lateral photo-Dember effect in graphene induced by nonequilibrium hot carrier dynamics. *Nano Letters* **15,** 4234-4239 (2015).
50. Sun, Z., Hasan, T., Torrisi, F., Popa, D., Privitera, G., Wang, F., Bonaccorso, F., Basko, D.M. & Ferrari, A.C. Graphene mode-locked ultrafast laser. *ACS Nano* **4,** 803-810 (2010).
51. Hendry, E., Hale, P. J., Moger, J., Savchenko, A. K. & Mikhailov, S. A. Coherent nonlinear optical response of graphene. *Physical Review Letters* **105,** 097401 (2010).
52. Cheng, J. L., Vermeulen, N. & Sipe, J. E. Third-order nonlinearity of graphene: Effects of phenomenological relaxation and finite temperature. *Physical Review B* **91,** 235320 (2015).
53. Kumar, N., Kumar, J., Gerstenkorn, C., Wang, R., Chiu, H. Y., Smirl, A. L. & Zhao, H. Third harmonic generation in graphene and few-layer graphite films. *Physical Review B* **87,** 121406 (2013).
54. Grigorenko, A. N., Polini, M. & Novoselov, K. S. Graphene plasmonics. *Nature Photonics* **6,** 749-758 (2012).
55. Koppens, F. H., Chang, D. E. & Garcia de Abajo, F. J. Graphene plasmonics: a platform for strong light–matter interactions. *Nano letters* **11,** 3370-3377 (2011).
56. Yan, H., Li, X., Chandra, B., Tulevski, G., Wu, Y., Freitag, M., Zhu, W., Avouris, P. & Xia, F. Tunable infrared plasmonic devices using graphene/insulator stacks. *Nature Nanotechnology* **7,** 330-334 (2012).
57. Yan, H., Low, T., Zhu, W., Wu, Y., Freitag, M., Li, X., Guinea, F., Avouris, P. & Xia, F. Damping pathways of mid-infrared plasmons in graphene nanostructures. *Nature Photonics* **7,** 394-399 (2013).
58. Mikhailov, S. A. & Ziegler, K. New electromagnetic mode in graphene. *Physical Review Letters* **99,** 016803 (2007).
59. Jablan, M., Buljan, H. & Soljacic, M. Plasmonics in graphene at infrared frequencies *Phys. Rev. B* **80,** 245435 (2009).
60. Hwang, E. H. & Sarma, S. D. Dielectric function, screening, and plasmons in two-dimensional graphene. *Physical Review B* **75,** 205418 (2007).
61. Lin, Y. M., Dimitrakopoulos, D., Jenkins, K. A., Farmer, D. B., Chiu, H. Y., Grill, A. & Avouris, P. 100-GHz transistors from wafer-scale epitaxial graphene. *Science* **327,** 662 (2010).

62. Xia, F., Mueller, T., Lin, Y. M., Valdes-Garcia, A. & Avouris, P. Ultrafast graphene photodetector. *Nature Nanotechnology* **4,** 840-843 (2009).
63. Vicarelli, L., Vitiello, M. S., Coquillat, D., Lombardo, A., Ferrari, A. C., Knap, W., Polini, M., Pellegrini, V. & Tredicucci, A. Graphene field-effect transistors as room-temperature terahertz detectors. *Nature Materials* **11,** 865-871 (2012).
64. Zheng, J., Wang. L., Quhe, R., Liu, Q., Li, H., Yu, D., Mei, W. N., Shi, J., Gao, Z. & Lu, J. Sub-10 nm Gate Length Graphene Transistors: Operating at Terahertz Frequencies with Current Saturation. *Scientific. Reports* **3,** 1314 (2013).
65. Hwang, H. Y., Brandt, N. C., Farhat, H., Hsu, A. L., Kong, J. & Nelson, K. A. Nonlinear THz conductivity dynamics in CVD-grown graphene. *arXiv:*1101.4985 [cond-mat.mtrl-sci] (2011).
66. Li, Z. Q., Henriksen, E. A., Jiang, Z., Hao, Z., Martin, M. C., Kim, P., Stormer, H. L. & Basov, D. N. Dirac charge dynamics in graphene by infrared spectroscopy. *Nature Phys.* **4,** 532-535 (2008).
67. Horng, J., Chen, C. F., Geng, B., Girit, C., Zhang, Y., Hao, Z., Bechtel, H. A., Martin, M., Zettl, A., Crommie, M. F., Shen, Y. R. & Wang, F. Drude conductivity of Dirac fermion in graphene. *Phys. Rev. B* **83,** 165113 (2011).
68. Bao, W. S., Liu, S. Y., Lei, X. L. & Wang, C. M. Nonlinear dc transport in graphene *J. Phys.: Condens. Matter* **21,** 305302 (2009).
69. Dora, B. & Moessner, R. Nonlinear electric transport in graphene: Quantum quench dynamics and the Schwinger mechanism. *Phys. Rev. B* **81,** 165431 (2010).
70. Mishchenko, E. G. Dynamic conductivity in graphene beyond linear response. *Phys. Rev. Lett.* **103,** 246802 (2009).
71. Shishir, R. S., Ferry, D. K. & Goodnick, S. M. Room temperature velocity saturation in intrinsic graphene. *J. Phys.: Conference Series* **193,** 012118 (2009).
72. Shareef, S., Ang, Y. S. & Zhang C. Room-temperature strong terahertz photon mixing in graphene. *J. Opt. Soc. Am. B* **29,** 274-279 (2012).
73. Mikhailov, S. A. Non-linear electromagnetic response of graphene. *Europhysics Letters* **79**2, 27002 (2007).
74. Wright, A. R., Xu, X. G., Cao, J. C. & Zhang, C. Strong nonlinear optical response of graphene in the terahertz regime. *App. Phys. Lett.* **95,** 072101 (2009).
75. Ishikawa, K. L. Nonlinear optical response of graphene in time domain. *Phys. Rev. B* **82,** 201402 (2010).
76. Al-Naib, I., Sipe, J. E. & Dignam, M. M. High harmonic generation in undoped graphene: Interplay of inter-and intraband dynamics. *Physical Review B* **90,** 245423 (2014).
77. Al-Naib, I., Sipe, J. E. & Dignam, M. M. Nonperturbative model of harmonic generation in undoped graphene in the terahertz regime. *New Journal of Physics* **17,** 113018 (2015).

78. Paul, M. J., Chang, Y. C., Thompson, Z. J., Stickel, A., Wardini, J., Choi, H., Minot, E. D., Norris, T. B. & Lee, Y. S. High-field terahertz response of graphene. *New Journal of Physics* **15,** 085019 (2013).
79. Tani, S., Blanchard, F. & Tanaka, K. Ultrafast carrier dynamics in graphene under a high electric field. *Phys. Rev. Lett.* **109,** 166603 (2012).
80. Sun, D., Divin, C., Mihnev, M., Winzer, T., Malic, E., Knorr, A., Sipe, J. E., Berger, C., de Heer, W. A., First, P. N. & Norris, T. B. Current relaxation due to hot carrier scattering in graphene. *New J. Phys.* **14,** 105012 (2012).
81. Winzer, T., Knorr, A., Mittendorff, M., Winnerl, S., Lien, M. B., Sun, D., Norris, T. B., Helm, M. & Malic, E. Absorption saturation in optically excited graphene. *Appl. Phys. Lett.* **101,** 221115 (2012).
82. Li, X., Barry, E. A., Zavada, J. M., Nardelli, M. B. & Kim, K. W. Influence of electron-electron scattering on transport characteristics in monolayer graphene. *Appl. Phys. Lett.* **97,** 082101 (2010).
83. Bonvalet, A. & Joffre, M. *Terahertz femtosecond pulses*, Springer, 1998.
84. Kim, K. Y., Taylor, A. J., Glownia, J. H. & Rodriguez, G. Coherent control of terahertz supercontinuum generation in ultrafast laser-gas interactions. *Nature Photonics* **2,** 605-609 (2008).
85. Bartel, T., Gaal, P., Reimann, K., Woerner, M. & Elsaesser, T. Generation of single-cycle THz transients with high electric-field amplitudes. *Optics Letters* **30,** 2805-2807 (2005).
86. Kim, K. Y., Glownia, J. H., Taylor, A. J. & Rodriguez, G. Terahertz emission from ultrafast ionizing air in symmetry-broken laser fields. *Opt. Express* **15,** 4577-4584 (2007).
87. Karpowicz, N., Lu, X. & Zhang, X. C. Terahertz gas photonics. *J. Modern Optics* **56,** 1137-1150 (2009).
88. Hou, B., Easter, J., Mordovanakis, A., Krushelnick, K. & Nees, J. A. Vacuum-free x-ray source based on ultrafast laser irradiation of solids. *Opt. Express* **16,** 17695-17705 (2008).
89. Chen, S. L., Chang, Y. C., Zhang, C., Ok, J. G., Ling, T., Mihnev, M. T., Norris, T. B. & Guo, L. J. Efficient real-time detection of terahertz pulse radiation based on photoacoustic conversion by carbon nanotube nanocomposite. *Nature Photonics* **8,** 537 (2014).
90. Dragoman, M., Neculoiu, D., Deligeorgis, G., Konstantinidis, G., Dragoman, D., Cismaru, A., Muller, A. A. & Plana, R. Millimeter-wave generation via frequency multiplication in graphene. *Appl. Phys. Lett.* **97,** 093101 (2010).
91. Sun, D., Wu, Z. K., Divin, C., Li, X., Berger, C., de Heer, W. A., First, P. N. & Norris, T. B. Ultrafast relaxation of excited Dirac fermions in epitaxial graphene using optical differential transmission spectroscopy. *Phys. Rev. Lett.* **101,** 157402 (2008).

92. Sun, D., Divin, C., Berger, C., de Heer, W. A., First, P. N. & Norris, T. B. Spectroscopic measurement of interlayer screening in multilayer epitaxial graphene. *Phys. Rev. Lett.* **104,** 136802 (2010).
93. Bowlan, P., Martinez-Moreno, E., Reimann, K., Elsaesser, T. & Woerner, M. Ultrafast terahertz response of multilayer graphene in the nonperturbative regime. *Physical Review B* **89,** 041408 (2014).
94. Park, J., Ahn, Y. H. & Ruiz-Vargas, C. Imaging of photocurrent generation and collection in single-layer graphene. *Nano Lett.* **9**, 1742 (2009).
95. Xia, F. N. et al. Photocurrent imaging and efficient photon detection in a graphene transistor. *Nano Lett.* **9,** 1039 (2009).
96. Mueller, T., Xia, F. N. A. & Avouris, P. Graphene photodetectors for highspeed optical communications. *Nature Photonics* **4,** 297 (2010).
97. Gan, X. et al. Chip-integrated ultrafast graphene photodetector with high responsivity. *Nature Photonics* **7,** 888 (2013).
98. Pospischil, A. et al. CMOS-compatible graphene photodetector covering all optical communication bands. *Nature Photonics* **7,** 892 (2013).
99. Echtermeyer, T. J. *et al.* Strong plasmonic enhancement of photovoltage in graphene. *Nature Commun.* **2,** 458 (2011).
100. Yao, Y., Shankar, R., Rauter, P., Song, Y., Kong, J., Loncar, M. & Capasso, F. High-responsivity mid-infrared graphene detectors with antenna-enhanced photocarrier generation and collection. *Nano Letters* **14,** 3749 (2014).
101. Furchi, M. et al. Microcavity-integrated graphene photodetector. *Nano Lett.* **12,** 2773-2777 (2012).
102. Liu, C. H., Dissanayake, N. M., Lee, S., Lee, K. & Zhong, Z. Evidence for extraction of photoexcited hot carriers from graphene. *ACS Nano* **6,** 7172 (2012).
103. Zhang, Y., Liu, T., Meng, B., Li, X., Liang, G., Hu, X. & Wang, Q. J. Broadband high photoresponse from pure monolayer graphene photodetector. *Nature Communications* **4,** 1811 (2013).
104. Vincent, J. D., Hodges S., Vampola J., Stegall M. & Pierce G. *Fundamentals of Infrared and Visible Detector Operation and Testing,* (Wiley,1990).
105. Cerna, M & Harvey A. F. *The Fundamentals of FFT-Based Signal Analysis and Measurement,* (National Instruments Application Note 041, 2000).
106. Iorsh, I. V., Mukhin, I. S., Shadrivov, I. V., Belov, P. A. & Kivshar, K. S. Hyperbolic metamaterials based on multilayer graphene structures. *Phys. Rev. B* **87,** 075416 (2013).
107. DaSilva, A. M., Chang, Y. C., Norris T. B. & MacDonald, A. H. Enhancement of photonic density of states in finite graphene multilayers. *Phys. Rev. B* **88,** 195411 (2013).
108. Mak, K. F., Sfeir, M. Y., Wu, Y., Lui, C. H., Misewich, J. A. & Heinz, T. F. Measurement of the Optical Conductivity of Graphene. *Phys. Rev. Lett.* **101,** 196405 (2008).

109. Choi, H., Borondics, F., Siegel, D. A., Zhou, S. Y., Martin, M. C., Lanzara, A. & Kaindl, R. A. Broadband electromagnetic response and ultrafast dynamics of few-layer epitaxial graphene. *Appl. Phys. Lett.* **94,** 172102 (2009).
110. Kravets, V. G., Grigorenko, A. N., Nair, R. P., Blake, P., Anissimova, S., Novoselov, K. S. & Geim, A. K. Spectroscopic ellipsometry of graphene and an exciton-shifted van Hove peak in absorption. *Phys. Rev. B* **81,** 155413 (2010).
111. Nelson, F. J., Kamineni, V. K., Zhang, T., Comfort, E. S., Lee J. U. & Diebold, A. C. Optical properties of large-area polycrystalline chemical vapor deposited graphene by spectroscopic ellipsometry. *Appl. Phys. Lett.* **97,** 253110 (2010).
112. Weber, J. W., Calado, V. E. & van de Sanden, M. C. M., Optical constants of graphene measured by spectroscopic ellipsometry. *Appl. Phys. Lett.* **97,** 091904 (2010).
113. Weber, J. W., Hinrichs, K., Gensch, M., van de Sanden, M. C. M. & Oates, T. W. H. Microfocus infrared ellipsometry characterization of air-exposed graphene flakes. *Appl. Phys. Lett.* **99,** 061909 (2011).
114. Wurstbauer, U., Röling, C., Wurstbauer, U., Wegscheider, W., Vaupel, M., Thiesen, P. H. & Weiss, D. Imaging ellipsometry of graphene. *Appl. Phys. Lett.* **97,** 231901 (2010).
115. Gaskell, P. E., Skulason, H. S., Strupinski, W. & Szkopek, T. High spatial resolution ellipsometer for characterization of epitaxial graphene. *Opt. Lett.* **35,** 3336 (2010).
116. Mousavi, S. H., Kholmanov, I., Alici, K. B., Purtseladze, D., Arju, N., Tatar, K., Fozdar, D. Y., Suk, J. W., Hao, Y., Khanikaev, A. B., Ruoff, R. S. & Shvets, G. Inductive Tuning of Fano-Resonant Metasurfaces Using Plasmonic Response of Graphene in the Mid-Infrared. *Nano Lett.* **13,** 1111 (2013).
117. Prokopeva, L. J., Chang, Y. C., Emani, N. K., Norris, T. B. & Kildishev, A. V. In-the-cloud optimization tool for retrieving experimentally fitted conductivity. *Proc. SPIE*. **9546,** Active Photonic Materials VII, 95461W (2015).
118. Prokopeva, L., Chang, Y. C., Kildishev, A. V. PhotonicVASEfit: VASE fitting tool. https://nanohub.org/resources/photonicvasefit. (DOI: 10.4231/D3JH3D373) (2015).
119. Azzam, R.M. & Bashara, N.M. *Ellipsometry and polarized light*, Elsevier Science Publishing Co., 1987.
120. Lee, S., Lee, K. & Zhong, Z. Wafer Scale Homogeneous Bilayer Graphene Films by Chemical Vapor Deposition. *Nano Letters* **10,** 4702 (2010).
121. Li, Z. Q., Henriksen, E. A., Jiang, Z., Hao, Z., Martin, M. C., Kim, P., Stormer, H. L. & Basov, D. N. Band Structure Asymmetry of Bilayer Graphene Revealed by Infrared Spectroscopy. *Phys. Rev. Lett.* **102,** 037403 (2009).
122. Mak, K. F., Lui, C. H., Shan, J. & Heinz, T. F. Observation of an Electric-Field-Induced Band Gap in Bilayer Graphene by Infrared Spectroscopy. *Phys. Rev. Lett.* **102,** 256405 (2009).

123. Mak, K. F., da Jornada, F. H., He, K., Deslippe, J., Petrone, N., Hone, J., Shan, J., Louie, S. G. & Heinz, T. F. Tuning Many-Body Interactions in Graphene: The Effects of Doping on Excitons and Carrier Lifetimes. *Phys. Rev. Lett.* **112,** 207401 (2014).
124. Smith, D. R. & Schurig, D. Electromagnetic wave propagation in media with indefinite permittivity and permeability tensors. *Phys. Rev. Lett.* **90,** 077405 (2003).
125. Poddubny, A., Iorsh, I., Belov, P. & Kivshar, Y. Hyperbolic metamaterials. *Nature Photonics* **7,** 948-957 (2013).
126. Jacob, Z., Kim, J. Y., Naik, G. V., Boltasseva, A., Narimanov, E. E. & Shalaev, V. M. Engineering photonic density of states using metamaterials. *Applied physics B* **100,** 215-218 (2010).
127. Krishnamoorthy, H. N., Jacob, Z., Narimanov, E., Kretzschmar, I. & Menon, V. M. Topological transitions in metamaterials. *Science* **336,** 205-209 (2012).
128. Guclu, C., Campione, S. & Capolino, F. Hyperbolic metamaterial as super absorber for scattered fields generated at its surface. *Phys. Rev. B* **86,** 205130 (2012).
129. Biehs, S. A., Tschikin, M., Messina, R. & Ben-Abdallah, P. Super-Planckian near-field thermal emission with phonon-polaritonic hyperbolic metamaterials. *Appl. Phys. Lett.*, ***102,*** 131106 (2013).
130. Liu, Z., Lee, H., Xiong, Y., Sun, C. & Zhang, X. Far-field optical hyperlens magnifying sub-diffraction-limited objects. *Science* **315,** 1686-1686 (2007).
131. Yang, X., Yao, J., Rho, J., Yin, X. & Zhang, X. Experimental realization of three-dimensional indefinite cavities at the nanoscale with anomalous scaling laws. *Nature Photonics* **6,** 450-454 (2012).
132. Narimanov, E. E. & Kildishev, A. V. Naturally hyperbolic. *Nature Photonics* **9**, 214-216 (2015).
133. Dai, S. *et. al.* Tunable phonon polaritons in atomically thin van der Waals crystals of boron nitride. *Science* **343,** 1125-1129 (2014).
134. Caldwell, J. D *et al.* Sub-diffractional volume-confined polaritons in the natural hyperbolic material hexagonal boron nitride. *Nature Communications* **5,** 5221 (2014).
135. Soukoulis, C. M. & Wegener, M. Past achievements and future challenges in the development of three-dimensional photonic metamaterials. *Nature Photonics* **5,** 523-530 (2011).
136. Zheludev, N. I. The road ahead for metamaterials. *Science* **328,** 582-583 (2010).
137. Valentine, J., Zhang, S., Zentgraf, T., Ulin-Avila, E., Genov, D. A., Bartal, G. & Zhang, X. Three-dimensional optical metamaterial with a negative refractive index. *Nature* **455,** 376-379 (2008).
138. Wurtz, G. A., Pollard, R., Hendren, W., Wiederrecht, G. P., Gosztola, D. J., Podolskiy, V. A. & Zayats, A. V. Designed ultrafast optical nonlinearity in a plasmonic nanorod metamaterial enhanced by nonlocality. *Nature Nanotechnology* **6,** 107-111 (2011).
139. Engheta, N. Pursuing near-zero response. *Science* **340,** 286-287 (2013).

140. Noginov, M. A., Barnakov, Y. A., Zhu, G., Tumkur, T., Li, H. & Narimanov, E. E. Bulk photonic metamaterial with hyperbolic dispersion. *Appl. Phys. Lett.* **94,** 151105 (2009).
141. Hoffman, A. J., Alekseyev, L., Howard, S. S., Franz, K. J., Wasserman, D., Podolskiy, V. A., Narimanov, E. E., Sivco, D. L. & Gmachl, C. Negative refraction in semiconductor metamaterials. *Nature Materials* **6,** 946-950 (2007).
142. Othman, M. A. K., Guclu, C. & Capolino, F. Graphene–dielectric composite metamaterials: evolution from elliptic to hyperbolic wavevector dispersion and the transverse epsilon-near-zero condition. *J. Nanophotonics* **7,** 073089-073089 (2013).
143. Othman, M. A. K., Guclu, C. & Capolino, F. Graphene-based tunable hyperbolic metamaterials and enhanced near-field absorption. *Optics Express* **21,** 7614-7632 (2013).
144. Wang, B., Zhang, X., García-Vidal, F. J., Yuan, X. & Teng, J. Strong coupling of surface plasmon polaritons in monolayer graphene sheet arrays. *Phys. Rev. Lett.* **109,** 073901 (2012).
145. Nefedov, I. S., Valaginnopoulos, C. A. & Melnikov, L. A. Perfect absorption in graphene multilayers. *J. Opt.* **15,** 114003 (2013).
146. Sreekanth, K. V., De Luca, A. & Strangi, G. Negative refraction in graphene-based hyperbolic metamaterials. *Appl. Phys. Lett.* **103,** 023107. (2013).
147. Andryieuski, A., Lavrinenko, A. V. & Chigrin, D. N. Graphene hyperlens for terahertz radiation. *Physical Review B* **86,** 121108 (2012).
148. Kidwai, O., Zhukovsky, S. V. & Sipe, J. E. Effective-medium approach to planar multilayer hyperbolic metamaterials: Strengths and limitations. *Phys. Rev. A* **85,** 053842 (2012).
149. Lee, S. H., Choi, J., Kim, H. D., Choi, H. & Min, B. Ultrafast refractive index control of a terahertz graphene metamaterial. *Scientific Reports* **3,** 2135 (2013).
150. Smith, D. R., Vier, D. C., Koschny, T. & Soukoulis, C. M. Electromagnetic parameter retrieval from inhomogeneous metamaterials. *Physical Review E* **71,** 036617 (2005).
151. Smith, D. R. & Pendry, J. B. Homogenization of metamaterials by field averaging. *JOSA B* **23,** 391-403 (2006).
152. Pfeiffer, C. & Grbic, A. Bianisotropic metasurfaces for optimal polarization control: analysis and synthesis. *Physical Review Applied* **2,** 044011 (2014).
153. Cortes, C. L., Newman, W., Molesky, S. & Jacob, Z. Quantum nanophotonics using hyperbolic metamaterials. *Journal of Optics* **14,** 063001 (2012).
154. Zhou, J., Koschny, T., Kafesaki, M. & Soukoulis, C. M. Negative refractive index response of weakly and strongly coupled optical metamaterials. *Phys. Rev. B* **80,** 035109 (2009).
155. Li, X. *et. al.* Large-area synthesis of high-quality and uniform graphene films on copper foils. *Science* **324,** 1312-1314 (2009).

156. Hwang, E. H., Adam, S. & Sarma, S. D. Carrier transport in two-dimensional graphene layers. *Phys. Rev. Lett.* **98,** 186806 (2007).
157. Liang, X. et. al. Toward clean and crackless transfer of graphene. *ACS nano* 5, 9144-9153 (2011).
158. Tarasov, A., Zhang, S., Tsai, M. Y., Campbell, P. M., Graham, S., Barlow, S., Marder, S. R. & Vogel, E. M. Controlled Doping of Large-Area Trilayer MoS_2 with Molecular Reductants and Oxidants. *Adv. Mater.* **27,** 1175-1181 (2015).
159. Paniagua, S. A., Baltazar, J., Sojoudi, H., Mohapatra, S. K., Zhang, S., Henderson, C. L., Graham, S., Barlow, S. & Marder, S. R. Production of heavily n-and p-doped CVD graphene with solution-processed redox-active metal–organic species. *Materials Horizons* **1,** 111-115 (2014).
160. Schedin, F., Geim, A. K., Morozov, S. V., Hill, E. W., Blake, P., Katsnelson, M. I. & Novoselov, K. S. Detection of individual gas molecules adsorbed on graphene. *Nature Materials* **6,** 652-655 (2007).
161. Bae. S. *et al.* Roll-to-roll production of 30-inch graphene films for transparent electrodes. *Nature Nanotechnology* **5,** 574-578 (2010).
162. Cui, Y., He, Y., Jin, Y., Ding, F., Yang, L., Ye, Y., Zhong, S., Lin, Y. & He, S. Plasmonic and metamaterial structures as electromagnetic absorbers. *Laser & Photonics Reviews* **8,** 495-520 (2014).
163. Ra'di, Y., Simovski, C. R. & Tretyakov, S. A. Thin perfect absorbers for electromagnetic waves: theory, design, and realizations. *Phys. Rev. Applied* **3,** 037001 (2015).
164. Watts, C. M., Liu, X. & Padilla, W. J. Metamaterial electromagnetic wave absorbers. *Advanced Materials* **24,** OP98–OP120 (2012).
165. Kats, M. A., Blanchard, R., Genevet, P. & Capasso, F. Nanometre optical coatings based on strong interference effects in highly absorbing media. *Nature Materials* **12,** 20-24 (2013).
166. Aydin, K., Ferry, V. E., Briggs, R. M. & Atwater, H. A. Broadband polarization-independent resonant light absorption using ultrathin plasmonic super absorbers. *Nature Communications* **2,** 517 (2011).
167. Ji, D., Song, H., Zeng, X., Hu, H., Liu, K., Zhang, N. & Gan, Q. Broadband absorption engineering of hyperbolic metafilm patterns. *Scientific Reports* **4,** 4498 (2014).
168. Narimanov, E. E. Photonic hypercrystals. *Physical Review X* **4,** 041014 (2014).
169. Narimanov, E. E. Dirac dispersion in photonic hypercrystals. *Faraday discussions* **178,** 45-59 (2015).
170. Huang, Z., & Narimanov, E. E. Veselago lens by photonic hyper-crystals. *Applied Physics Letters* **105,** 031101 (2014).
171. Galfsky, T., Narimanov, E. & Menon, V. Enhanced spontaneous emission in photonic hypercrystals. *In Frontiers in Optics,* FW6A-3, Optical Society of America, October 2015.

172. Salisbury, W.W. Absorbent body of electromagnetic waves, *U.S. Patent* No. 2,599,944, 10 June 1952.
173. Fan, S. & Joannopoulos, J. D. Analysis of guided resonances in photonic crystal slabs. *Physical Review B* **65,** 235112 (2002).
174. Piper, J. R. & Fan, S. Total absorption in a graphene monolayer in the optical regime by critical coupling with a photonic crystal guided resonance. *ACS Photonics* **1,** 347-353 (2014).
175. Ding, Y. & Magnusson, R. Resonant leaky-mode spectral-band engineering and device applications. *Optics Express*, **12,** 5661-5674 (2004).
176. Inoue, T., De Zoysa, M., Asano, T. & Noda, S. Realization of dynamic thermal emission control. *Nature Materials* **13,** 928-931 (2014).
177. Ganesh, N., Zhang, W., Mathias, P.C., Chow, E., Soares, J.A.N.T., Malyarchuk, V., Smith, A.D. & Cunningham, B.T Enhanced fluorescence emission from quantum dots on a photonic crystal surface. *Nature Nanotechnology* **2,** 515-520 (2007).
178. de Ceglia, D., Vincenti, M. A., Grande, M., Bianco, G. V., Bruno, G., D'Orazio, A. & Scalora, M. Tuning infrared guided-mode resonances with graphene. *JOSA B* **33,** 426-433 (2016).
179. Park, J., Kang, J. H., Liu, X. & Brongersma, M. L. Electrically Tunable Epsilon-Near-Zero (ENZ) Metafilm Absorbers. *Scientific Reports* **5,** 15754 (2015).
180. Palik, E. D. *Handbook of optical constants of solids*. Academic press, 1998.
181. Li, P., Lewin, M., Kretinin, A.V., Caldwell, J.D., Novoselov, K.S., Taniguchi, T., Watanabe, K., Gaussmann, F. & Taubner, T. Hyperbolic phonon-polaritons in boron nitride for near-field optical imaging and focusing. *Nature Communications* **6,** 7507 (2015).
182. Dai, S. *et al.* Graphene on hexagonal boron nitride as a tunable hyperbolic metamaterial. *Nature Nanotechnology* **10,** 682-686 (2015).
183. Liu, V. & Fan, S. S4: a free electromagnetic solver for layered periodic structures. *Computer Physics Communications* **183,** 2233-2244 (2012).
184. Hu, H., Ji, D., Zeng, X., Liu, K. & Gan, Q. Rainbow trapping in hyperbolic metamaterial waveguide. *Scientific Reports* **3,** 1249 (2013).
185. Pfeiffer, C. & Grbic, A. Bianisotropic metasurfaces for optimal polarization control: Analysis and synthesis. *Physical Review Applied* **2,** 044011 (2014).
186. Joannopoulos, J. D., Johnson, S. G., Winn, J. N. & Meade, R. D. *Photonic crystals: molding the flow of light*. Princeton university press, 2011.
187. Wang, F. & Shen, Y. R. General properties of local plasmons in metal nanostructures. *Physical Review Letters* **97,** 206806 (2006).
188. Molesky, S., Dewalt, C. J. & Jacob, Z. High temperature epsilon-near-zero and epsilon-near-pole metamaterial emitters for thermophotovoltaics. *Optics Express* **21,** A96-A110 (2013).

189. Meric, I., Dean, C. R., Petrone, N., Wang, L., Hone, J., Kim, P. & Shepard, K. L. Graphene field-effect transistors based on boron–nitride dielectrics. *Proceedings of the IEEE* **101,** 1609-1619 (2013).
190. Dean, C.R., Young, A.F., Meric, I., Lee, C., Wang, L., Sorgenfrei, S., Watanabe, K., Taniguchi, T., Kim, P., Shepard, K.L. & Hone, J. Boron nitride substrates for high-quality graphene electronics. *Nature Nanotechnology* **5,** 722-726 (2010).
191. Kumar, A., Low, T., Fung, K. H., Avouris, P. & Fang, N. X. Tunable light–matter interaction and the role of hyperbolicity in graphene–hBN system. *Nano Letters* **15,** 3172-3180 (2015).
192. Jablan, M. *Electrodynamic properties of graphene and their technological applications.* Doctoral thesis of University of Zagreb, 2012.
193. Trushin, M., & Schliemann, J. Anisotropic photoconductivity in graphene. *Europhysics Letters* **96,** 37006 (2011).
194. Yeh, Pochi. *Optical waves in layered media.* New York, Wiley, 1988.